Advanced control of ultrashort and high-power pulses in enhancement cavities

Nikolai Lilienfein

SIGILL · UNIVERSITAT · LUDOVIC · MAXIM ·

München 2018

Advanced control of ultrashort and high-power pulses in enhancement cavities

Nikolai Lilienfein

Dissertation
an der Fakultät für Physik
der Ludwig–Maximilians–Universität
München

vorgelegt von
Nikolai Lilienfein
aus Duisburg

München, den 28.08.2018

Erstgutachter: Prof. Dr. Ferenc Krausz
Zweitgutachter: Prof. Dr. Jens Limpert
Tag der mündlichen Prüfung: 02.10.2018

Zusammenfassung

Überhöhungsresonatoren haben sich im Verlauf des letzten Jahrzehnts zu einer vielversprechenden Technologie zur Erzeugung extrem-ultravioletten (XUV) Lichtes für Frequenzkammspektroskopie und Attosekundenphysik entwickelt. Diese Anwendungen verlangen kohärente Lichtquellen, welche durch die Erzeugung hoher Harmonischer von ultrakurzen Laserpulsen bei hohen Intensitäten realisiert werden können. Die meisten üblichen Lasersysteme können solche Pulse nur bei Wiederholraten im Kilohertzbereich produzieren. Die Überhöhung von Femtosekunden-Laserpulsen zu Durchschnittsleistungen von einigen Kilowatt in passiven Resonatoren bietet eine Möglichkeit, die benötigten Intensitäten bei Pulswiederholraten von vielen Megahertz zu erreichen. Die Erzeugung von XUV Pulsen mit ausreichendem Fluss bei solchen Wiederholraten würde diese unzugängliche Region des optischen Spektrums für die Frequenzkammmetrologie öffnen und hat zudem das Potential die Messdauer von Experimenten der Attosekundenphysik um viele Größenordnungen zu verkürzen.

Die resonatorgestützte Erzeugung hoher Harmonischer ist allerdings mit einer Reihe eigener Einschränkungen verbunden. Diese betreffen insbesondere die erreichbare Durchschnitts- und Spitzenleistung, sowie die minimale Pulsdauer im Resonator. Diese Dissertation stellt neue Ansätze zur Erweiterung des Potentials von Überhöhungsresonatoren für Femtosekundenpulse vor.

In einem ersten Experiment wurde die Kompensation thermisch induzierter Linseneffekte in Überhöhungsresonatoren durch den Einbau geeigneter Brewster-Platten, welche auch als XUV-Auskoppelelemente Verwendung finden können, demonstriert. Mit diesem Ansatz konnte die Strahlgröße im Resonator für Durchschnittsleistungen von bis zu 160 kW konstant gehalten werden.

Anschließend wurde die Wechselwirkung zwischen nichtlinearer Plasmaerzeugung, die eine Vorraussetzung zur Erzeugung hoher Harmonischer darstellt, und der Resonatorüberhöhung untersucht. Aus einem experimentell validierten numerischen Modell konnte ein Skalierungsgesetz abgeleitet werden, welches die optimierte Auslegung von Überhöhungsresonatoren zur Erzeugung hoher Harmonischer erlaubt. Das Modell wurde außerdem vewendet, um ein neuartiges Konzept für die effiziente Kompression ultrakurzer Pulse in Überhöhungsresonatoren mit auf die Nichtlinearität zugeschnittener spektraler Finesse zu entwickeln.

Weitere Arbeiten behandeln die Optimierung der Resonatordispersion. Durch Kombination von Spiegelbeschichtungen mit passenden spektralen Phasenverläufen konnten Resonatoren zur Überhöhung von wellenstabilen Pulsen und von ultrakurzen Pulsen mit einer Dauer von unter sechs Zyklen der Trägerwelle realisiert werden. Diese Resultate stellen wesentliche Vorraussetzungen für die Erzeugung isolierter Attosekundenpulse in Resonatoren dar.

In der Folge wurden die zuvor entwickelten Methoden zur Kontrolle der Resonatordispersion zusammen mit einer flexiblen Technik zur Resonatorlängenreferenzierung für die erste Demonstration von Solitonen in Freistrahl-Überhöhungsresonatoren angewendet. Durch eine maßgeschneiderte spektrale Finesse konnte dabei eine Pulskompression von 350 fs auf 37 fs, bei einem Überhöhungsfaktor der Spitzenleistung von über 3000 erreicht werden. Dieses

überraschende Resultat belegt das Potential dieses Konzeptes für Auslegung und Betrieb nichtlinearer Überhöhungsresonatoren, und legt eine zukünftige Anwendung für resonatorgestützte Erzeugung hoher Harmonischer nahe.

Zusätzlich wurde ein Konzept für die optomechanische Auskopplung von Laserpulsen vorgeschlagen, welches eine Rolle bei der Verwendung von Überhöhungsresonatoren in einer neuen Klasse von Lasersystemen zur Erzeugung hochenergetischer Pulse spielen könnte.

Preface

In the decade preceding this thesis, femtosecond enhancement cavities had emerged as a highly promising technology in the context of extreme ultraviolet light (XUV) sources for frequency comb metrology and attosecond physics. These applications require light of laser-like coherence, which can be provided by high-order harmonic generation (HHG), a highly nonlinear frequency conversion process driven by intense ultrashort laser pulses. The laser systems commonly used to drive HHG are limited to pulse repetition rates in the kilohertz range. In contrast, the enhancement of femtosecond pulses in passive optical cavities to average powers of many kilowatts delivers the necessary intensities even at repetition rates of tens to hundreds of megahertz. Achieving sufficient XUV flux with megahertz repetition rates would enable the extension of frequency comb metrology to the XUV, and dramatically reduce data acquisition times for experiments in attosecond physics. However, cavity-enhanced HHG comes with unique challenges, imposing cavity-related limitations to the power, peak intensity, and minimum duration of the driving pulses. In this thesis, several novel approaches to extending the capabilities of femtosecond enhancement cavities are presented.

In a first experiment, we demonstrated the compensation of thermal lensing effects in enhancement cavities. Using intracavity Brewster plates, which also offer a robust solution for XUV output coupling in cavity-enhanced HHG setups, we gained control over the thermally-induced mode change at average powers of up to 160 kW.

Subsequently, we investigated the effects of nonlinear phase modulations caused by ionization in an intracavity gas target, which is a prerequisite for HHG. We experimentally validated a numerical model of the plasma-cavity interaction, leading to a scaling law allowing for the layout of optimized cavity HHG systems, and a proposal for tailoring the spectral finesse of cavities to exploit the nonlinear phase modulation for intracavity pulse compression.

In parallel, we worked on the design and characterization of highly reflective multilayer mirrors to optimize the cavity dispersion. Combining different mirrors with compatible spectral phase characteristics, we demonstrated enhancement cavities supporting waveform-stable pulses, and cavities supporting pulse durations approaching the few-cycle regime. These results represent vital technological developments towards the goal of isolated attosecond pulse generation with enhancement cavities.

Finally, we applied the developed methods of dispersion control to design an enhancement cavity for intracavity pulse compression using self-phase modulation in a Brewster plate. Implementing a flexible locking scheme, we demonstrated for the first time the generation of temporal cavity solitons in free-space enhancement cavities. The temporal compression from 350 fs to 37 fs together with the spectrally tailored finesse resulted in a peak power enhancement factor of over 3000, significantly surpassing the enhancement in linear cavities supporting similar pulse durations. This intriguing result opens the door to a novel regime of nonlinear cavity operation, with potentially significant benefits to cavity-enhanced HHG.

In addition, we proposed a concept for optomechanical cavity dumping, with the potential to aid efforts employing enhancement cavities for a new generation of high-pulse-energy lasers.

Structure of the thesis

The results included in this cumulative thesis are presented in two parts. Part I aims to motivate the research objective, to introduce the theory of operation of femtosecond enhancement cavities, to summarize the results, and to provide the broader context in which the presented research was conducted. Part II includes the results of this work in the form of the published (or submitted) manuscripts. These manuscripts are self-contained, i.e., each should be accessible without knowledge of the prior chapters. All of these results involve contributions from multiple people. My contribution to each is summarized in statements preceding the respective articles. Five of the manuscripts presented in this thesis were published as peer-reviewed journal articles, and one manuscript is currently in review:

1. *N. Lilienfein*, H. Carstens, S. Holzberger, C. Jocher, T. Eidam, J. Limpert, A. Tünnermann, A. Apolonski, F. Krausz, and I. Pupeza, **Balancing of thermal lenses in enhancement cavities with transmissive elements**, Optics Letters 40, 843–846 (2015), DOI: 10.1364/OL.40.000843.

2. S. Holzberger, *N. Lilienfein*, M. Trubetskov, H. Carstens, F. Lücking, V. Pervak, F. Krausz, and I. Pupeza, **Enhancement cavities for zero-offset-frequency pulse trains**, Optics Letters 40, 2165–2168 (2015), DOI: 10.1364/OL.40.002165.

3. S. Holzberger, *N. Lilienfein*, H. Carstens, T. Saule, M. Hogner, F. Lücking, M. Trubetskov, V. Pervak, T. Eidam, J. Limpert, A. Tünnermann, E. Fill, F. Krausz, and I. Pupeza, **Femtosecond enhancement cavities in the nonlinear regime**, Physical Review Letters 115, 023902 (2015), DOI: 10.1103/PhysRevLett.115.0239025.

4. *N. Lilienfein*, C. Hofer, S. Holzberger, C. Matzer, P. Zimmermann, M. Trubetskov, V. Pervak, and I. Pupeza, **Enhancement cavities for few-cycle pulses**, Optics Letters 42, 271–274 (2017), DOI: 10.1364/OL.42.000271.

5. *N. Lilienfein*, S. Holzberger, and I. Pupeza, **Ultrafast optomechanical pulse picking**, Applied Physics B 123, 1916 (2017), DOI: 10.1007/s00340-016-6608-4.

6. *N. Lilienfein*, C. Hofer, T. Saule, M. Högner, M. Trubetskov, V. Pervak, E. Fill, C. Riek, A. Leitenstorfer, J. Limpert, F. Krausz, and I. Pupeza, **Temporal solitons in free-space femtosecond enhancement cavities**, Manuscript in review aa a Letter to Nature Photonics, submitted on June 14th, 2018, Tracking number NPHOT-2018-06-00751.

In the course of my Ph.D. work, I have contributed to a further eight peer-reviewed publications, to two manuscripts currently in review, and have filed one patent application. A list of these research items is included at the back of this thesis.

Contents

Part I

Framework

Chapter 1
Introduction

1.1 Enhancement cavities

Enhancement cavities are optical resonators – systems of reflective surfaces for the spatial confinement of light – used to locally increase the intensity of a laser. The history of optical resonators goes back to the interferometer pioneered by Charles Fabry and Alfred Pérot in 1897, the basic concept of which had already been considered theoretically over sixty years before by George Airy [1]. In contrast to earlier interferometers, for instance those used by Michelson and Sagnac, in which light was split between two distinct arms and subsequently brought to interference, the Fabry-Pérot interferometer involves an indefinite number of back-and-forth reflections between two parallel mirrors, all interfering simultaneously.

The longitudinal transmission of light through the Fabry-Pérot interferometer is described by the Airy-distribution, which depends on the reflectivity of the surfaces, the optical length of the path between the surfaces, and the wavelength of the light. In contrast to the interference fringes observed in two-armed interferometers, which follow a sinusoidal function , the bright fringes of the Airy distribution can exhibit a very narrow width with respect to the separation of adjacent fringes. Their "fine-ness" or *finesse* is proportional to the reflectivity of the mirrors (disregarding other loss-mechanisms), and thus related to the effective number of roundtrips experienced by the light "caught" between the mirrors. Appearing upon constructive interference of all reflections, the fringes can be understood as resonances of the electromagnetic field constrained by the reflective surfaces of the Fabry-Pérot interferometer, which thus constitutes an *optical resonator*.

The resonances, also referred to as *longitudinal modes* of the resonator, appear periodically in the transmission spectrum, with their spectral separation depending on the length of the resonator. When these modes are resonantly excited, the intensity inside the resonator is enhanced by a factor proportional to the finesse with respect to the impinging intensity. Fabry and Pérot immediately realized the advantages afforded by the finesse of the fringes for the precision of interferometric measurements. In the following years, they developed remarkably well-engineered interferometers, and exploited this effect for a number of breakthrough experiments in astronomy and early work on optical metrology [1].

While its plane mirrors constrain the propagation of electromagnetic waves in longitudinal direction, the classical Fabry-Pérot resonator is wide open in the transverse directions. It is highly sensitive to misalignments and surface deformations, which result in field spillage over the edges of the mirrors, and effectively degrade the finesse. Even in the absence of such defects, its finesse is limited by diffraction losses at the edges of its finite-sized mirrors. With increasing mirror separations, these effects become increasingly severe.

After the invention of the laser in 1960 [2], the crucial role of optical resonators as a component of laser oscillators led to the rapid development and understanding of more stable resonator types based on spherical mirrors, and of Gaussian optics in general [3]. While not directly appearing in the acronym LASER (light amplification by stimulated emission of radiation), the use of Fabry-Pérot resonators as amplifying cavities of laser oscillators is fundamental to the laser concept and was already a key part of the early maser and laser proposals [4, 5]. It provides a feedback structure which encloses the gain material, effectively confining the radiation to the resonator modes and facilitating the generation of coherent and directed light.

In this context, the field propagation within optical resonators became a highly relevant question for optimizing laser operation. The numerical work of Fox and Li [6] uncovered the existence of discrete transverse modes in optical resonators, closely followed by the development of Gaussian mode theory [7]. Within a few years, most of the nowadays familiar concepts of resonator optics emerged [3]. Importantly, it was realized that open-sided resonators containing suitable spherical mirrors can form stable optical cavities [8]. "Stable" means that they exhibit *transverse resonator modes*, typically given by Gauss-Hermite functions, representing beams which are reproduced with every roundtrip and thus spatially confined in the cavity.

Not only do these concepts apply to the active oscillators at the heart of laser systems, but also to passive optical resonators, which have found diverse applications in laser science and technology. Thanks to the transverse mode confinement in stable cavities and the development of high-reflectivity dielectric multilayer mirrors, resonators with extremely low roundtrip losses and a correspondingly high finesse have become available. In concert with the ability to coherently excite such resonators with laser light, there are in particular two properties of passive resonators that make them extremely useful. These are (I) the *power enhancement* of light inside the cavity, and (II) its enhanced sensitivity with respect to intracavity absorption and phase changes. For these reasons they are often referred to as *enhancement cavities*.

Enhancement cavities can be implemented in a multitude of forms, from microcavities, used for instance in investigations of cavity quantum electrodynamics of free atoms [9] and nonlinear dynamics [10, 11], to kilometer-scale cavities incorporated in the interferometers built for the recently successful quest for gravitational wave detection [12, 13]. In laser technology, the power enhancement inside such cavities has been utilized to boost the efficiency of nonlinear conversion processes such as second harmonic generation [14, 15].

1.2 Ultrafast lasers

In the decades since Theodeore Maiman [2] constructed the first laser using a flash-lamp pumped ruby crystal, a vast number of gain materials and laser architectures producing light over a broad range of the electromagnetic spectrum with wildly different properties have been developed [16]. Today, lasers are ubiquitous in everyday technology and vital to the physical sciences, with laser technology being as diverse as its fields of application. Since the laser's inception, the major themes of development have been its scalability towards higher average power, shorter laser pulses and higher peak intensity, longer coherence length, and broader spectral coverage, with these directions being variously intertwined. In terms of spectral coverage, significant effort is going into pushing the photon energies of laser sources into the extreme ultraviolet (XUV) range.

A particularly fascinating group of laser architectures are mode-locked lasers, and in particular passively mode locked lasers, capable of producing laser pulses with femtosecond durations [17]. To this end, several longitudinal modes of the laser oscillator are coupled by carefully engineered nonlinear mechanisms, causing them to resonate simultaneously with a fixed phase relationship. The emitted frequency spectrum consists of a vast number of equally spaced lines. Its structure is characterized by two radio frequencies, one of which is the line spacing and the other the offset of its first line. If both frequencies are stabilized, this spectrum is referred to as a *frequency comb*, and presents a powerful tool for optical metrology [18, 19], linking optical frequencies to radio frequencies.

In the time domain, this spectral structure corresponds to an infinite train of short pulses, stemming from one or more pulses traveling in the laser oscillator. In a time-domain picture of mode locking, the mode-locking mechanism effectively produces an additional *temporal* confinement of the already spatially confined light in the oscillator cavity. The repetition rate of the resulting pulse train is typically in the range of 100 MHz, corresponding to a length of the laser oscillator of a few meters. The spectral bandwidth, and correspondingly the minimum duration of pulses produced from laser oscillators are limited primarily by the spectral gain profile of the laser medium, but also depend on the mode-locking mechanism and the dispersion of the oscillator [17]. The short pulse duration with respect to the pulse repetition period afforded by mode-locked lasers results in high peak intensities being achievable at moderate average powers. In laser systems optimized for maximum peak intensity and/or pulse energy, the repetition rate is further reduced to kilohertz or even hertz levels before subsequent amplification. This has allowed for a variety of nonlinear optical effects to be studied and efficiently exploited. In particular, nonlinear optical effects can be used to extend and shift the bandwidth of the driving laser, giving access to wavelength ranges that lack suitable gain materials. Also, optical pulses can be temporally compressed by nonlinear means. Today, minimum pulse durations in the range of a few femtoseconds to a few tens of femtoseconds can be achieved in a variety of wavelength ranges. Notably, the duration of pulses can approach the period of the electromagnetic wave oscillation itself. Such pulses are referred to as few-cycle or single-cycle pulses [20, 21].

One of the most important nonlinear conversion mechanisms is the generation of coherent XUV light by high-order harmonic generation (HHG). The HHG process involves intense driving pulses ionizing atoms in a medium, for instance a noble gas. After being accelerated in the oscillating laser field, some of the freed electrons recollide with the atoms and emit high-energy ultraviolet (UV) photons, the “harmonics”. Notably, this UV emission preserves the coherence properties of the driving laser, thus providing coherent radiation in this otherwise inaccessible spectral region [22, 23]. Driven by single-cycle laser pulses, HHG can produce isolated XUV pulses [24] as short as 80 as [25], representing the shortest events produced by mankind. Used in pump-probe photoelectron spectroscopy (PES) experiments, such pulses have allowed to investigate physical processes on unprecedented time scales, marking the birth of attosecond metrology [24, 26].

The peak intensity necessary for HHG is in the range of 10^{13}–$10^{14}\,\mathrm{W\,cm^{-2}}$. The repetition rate of the complex laser systems capable of providing pulses of such intensity is typically restricted to the kilohertz range, due to constraints relating to the average power. One of the main directions of current scientific laser development is the adaptation of high-average-power ytterbium-based laser architectures, for ultrafast and high-energy lasers [27–33]. With respect to HHG, this approach holds promise for further development both in terms of photon energy and XUV power, and for increasing repetition rates [34–40].

There are in particular two fields of application to which coherent XUV generation at much higher repetition rates would be highly beneficial. The first concerns time-resolved and angle-resolved photo-electron spectroscopy experiments [41], which are a crucial technique of attosecond science. Here space-charge effects severely limit the permitted number of generated electrons per pulse [42], leading to long, and in some cases prohibitive measurement times at kilohertz repetition rates [43]. If the driving laser repetition rates could be increased to those produced by the laser oscillators at the heart of laser systems, acquisition times could potentially be reduced by 3 to 5 orders of magnitude. The second major goal pursued via cavity-enhanced HHG is the extension of frequency comb spectroscopy to the XUV range. There is a number of targets for spectroscopy experiments in this spectral range which would be highly interesting both for fundamental science and metrology. These include fundamental transitions of hydrogen-like atomic systems such as $\mathrm{He^+}$ and $\mathrm{Li^{2+}}$, which could provide precise tests of quantum electro dynamics [44–46], and low-lying nuclear transitions, most notably the recently detected [47] nuclear clock transition in thorium-229, with the potential to significantly surpass current frequency standards in accuracy [48]. With frequency comb spectroscopy requiring a certain power per comb line, and the line spacing of the comb being identical to the repetition rate of the laser, megahertz repetition rates are a necessity for such experiments [49, 50].

1.3 Enhancement cavities for HHG

An elegant approach to multi-megahertz HHG is offered by *femtosecond enhancement cavities*, which enabled the development of XUV sources with a unique combination of high repetition rate and high photon energy. In the wake of the full stabilization of frequency combs, it was demonstrated that matching the comb lines to the resonance structure of enhancement cavities allows for the enhancement of femtosecond pulses [51]. The potential to generate pulses of extremely high peak power inside such femtosecond enhancement cavities without actual amplification makes them a highly appealing tool for nonlinear optics. While a first proposal sought to periodically extract these pulses for further use [51], a scheme later termed "stack and dump" (SnD) [52], the main application pursued since then has been intracavity XUV generation via HHG [49, 50]. A major challenge for both these applications is the extraction of the generated radiation from the closed optical cavity. While the lack of success of the SnD scheme is mainly due to this problem, a number of solutions for XUV output coupling have been found. These include intracavity Brewster plates [49, 50] and other transmission optics [53, 54], nanogratings etched onto cavity mirrors [55, 56] and different geometric schemes [57–61].

It was realized early on that the dispersion of cavity mirrors and other intracavity media limit the optical bandwidth and thus the minimum pulse duration in femtosecond enhancement cavities [51, 62]. The sensitivity to the spatial phase curvature caused by this dispersion is proportional to the cavity finesse. The same applies to the temporal phase shifts produced by nonlinear effects in the cavity, which have a detrimental effect on the enhancement level [49, 63]. Such effects can occur both in transmissive optics, if present, and in the process of laser-driven ionization, and lead to an intensity-clamping behavior in nonlinear enhancement cavities. The conversion efficiency of the HHG process, as well as the harmonic cut-off marking the highest generated photon energies critically depend on the driving pulses' peak intensity. With ionization being an inherent part of the HHG process, the associated intensity clamping represents the main limiting factor to the power scalability of intracavity XUV generation [64, 65].

The first demonstrations of cavity-enhanced HHG were performed in high-finesse cavities seeded directly by relatively low-power mode-locked Titanium:Sapphire oscillators [49, 50, 58]. In the following years, large performance gains in terms of generated XUV power and photon energy were achieved by adopting more and more powerful seeding sources such as amplified Titanium:Sapphire lasers [66] and high-power ytterbium-doped fiber chirped-pulse amplifiers [67–69], allowing a reduction of the cavity finesse [56, 60, 70, 71].

Apart from downscaling the finesse, promising paths towards higher XUV power is to increase the interaction volume over which HHG takes place, and/or to increase the pulse repetition rate, while keeping the intensity constant. Both paths require an upscaling of the intracavity power. The power scalability of femtosecond enhancement cavities was investigated by Pupeza *et al.* [72], achieving 18 and 72 kW of average power with pulse durations of 200 fs and 2 ps, respectively, limited by peak-intensity induced mirror damage. The identification of suitable cavity geometries to increase the beam size on the mirrors [73] and mitigation of thermal lensing effects, to which this geometry is particularly sensitive, allowed for average powers of 400 kW and 670 kW for similar pulse durations, respectively [74]. The limitation to the power scalability of femtosecond enhancement cavities was identified as a combination of intensity-induced mirror damage, and thermal lensing effects [74]. Importantly, these result were achieved in empty enhancement cavities which did not include output coupling devices or gas targets.

Another promising approach to mitigate the effects of nonlinear intensity clamping was suggested by results showing that its severity is reduced for shorter driving pulse durations [60]. The restrictions of the cavity bandwidth relating to the mirror dispersion, however, necessitate the development of novel low-dispersion mirrors to achieve progress in this direction. Femtosecond enhancement cavities supporting significantly shorter pulse durations would have the additional benefit of potentially allowing the intracavity generation of isolated attosecond pulses. While the pulse durations in the range of a few femtoseconds necessary for direct isolated attosecond pulse generation seem unattainable in enhancement cavities, a number of promising temporal gating schemes [75–79], some of which could be applicable in enhancement cavities for pulse durations of about 20 fs at 1 µm wavelength [80, 81], have been investigated.

In addition to significant progress in terms of supported bandwidth, the generation of isolated attosecond pulses would also require control over the waveform evolution of the enhanced pulses [24, 82]. While high-power lasers [83, 84] providing waveform-stable pulses have become available, the constraints of femtosecond pulse enhancement related to the cavity dispersion make this challenging.

1.4 Research objective

The research objective of the work presented here was the development of novel approaches to overcome the cavity-related technological challenges associated with cavity-enhanced high-order harmonic generation and isolated attosecond pulse generation. In summary, these challenges were identified as the power scalability, the bandwidth (and thus pulse duration) scalability, the control of the field evolution, and the nonlinearity-induced intensity clamping in femtosecond enhancement cavities.

Chapter 2

Background

In this chapter the theoretical concepts and experimental considerations relevant to the power enhancement of short, intense pulses in optical resonators are summarized.

2.1 Power relations in optical resonators

The power enhancement in a passive optical resonator depends on the interferometric coupling of an impinging light field at its partially transmissive input coupling mirror, and the roundtrip losses of the resonator. In this section, some basic relations governing the power enhancement in optical resonators are introduced for the case of a single optical frequency ω_0, and plane waves (i.e. neglecting diffraction).[1]

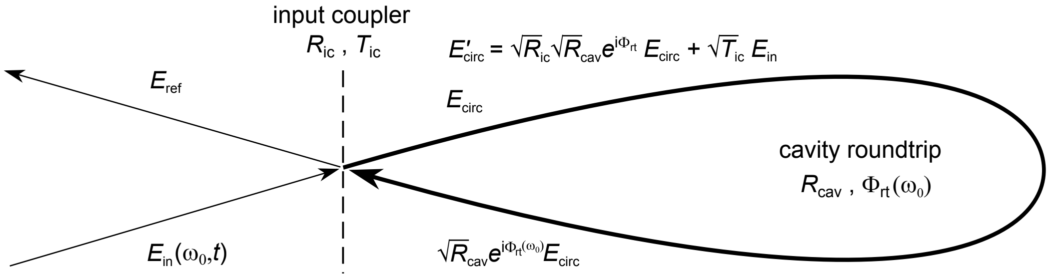

Figure 2.1: Schematic of a passive optical resonator. A monochromatic light wave $E_{in}(\omega_0, t)$ with angular frequency ω_0 impinges on the input coupling surface with the power transmission T_{ic} and power reflectivity R_{ic}. An initial intraresonator field E_{circ} is circulated back to the input coupler experiencing a power attenuation R_{cav} and a phase $\Phi_{rt}(\omega_0)$. It interferes with the input field to form the new circulating field E'_{circ} in the resonator, and the reflected field E_{ref}.

Figure 2.1 illustrates the interference of light waves at the input coupling mirror of an enhancement resonator. The resonator can be parametrized by the power transmission T_{ic}

---

[1] An excellent textbook covering basic properties of enhancement cavities is [85].

and reflectivity $R_{\mathrm{ic}} = 1 - T_{\mathrm{ic}}$ of its input coupling mirror, the power attenuation factor R_{cav} acquired upon a resonator roundtrip (*excluding* the input coupler reflectivity), and the phase Φ_{rt} acquired upon one roundtrip (*including* the input coupler phase upon reflection). The roundtrip phase of an electromagnetic wave of angular frequency ω_0 is simply $\Phi_{\mathrm{rt}}(\omega_0) = \omega_0 t_{\mathrm{rt}}$, with the roundtrip time $t_{\mathrm{rt}} = L/v_{\mathrm{p}}$ in a resonator of length L and with a phase velocity v_{p}. It is important to note that t_{rt} can be frequency dependent, which becomes relevant for the enhancement of femtosecond laser pulses (Sec. 2.3). Initially, the fraction T_{ic} of an impinging electromagnetic wave E_{in} is transmitted into the resonator, now forming the circulating field E_{circ}. After one roundtrip, the circulating field interferes with the transmitted field at the input coupler, now forming the new intra-resonator field $E'_{\mathrm{circ}} = \sqrt{R_{\mathrm{ic}} R_{\mathrm{cav}}} e^{i\Phi_{\mathrm{rt}}} E_{\mathrm{circ}} + \sqrt{T_{\mathrm{ic}}} E_{\mathrm{in}}$. The field is resonant when $\Phi_{\mathrm{rt}} = n2\pi$, where n is an integer number. In the resonant case, the interference is constructive and optical power is transferred from the impinging field to the circulating field. After a number of roundtrips a steady state defined by $E'_{\mathrm{circ}} = E_{\mathrm{circ}}$ develops. Solving this equation yields the *resonant* steady-state power enhancement $\mathbb{E}_{\mathrm{R}}$:

$$\mathbb{E}_{\mathrm{R}} = \left. \frac{|E_{\mathrm{circ}}|^2}{|E_{\mathrm{in}}|^2} \right|_{\Phi_{\mathrm{rt}} = n2\pi} = \frac{T_{\mathrm{ic}}}{\left(1 - \sqrt{R_{\mathrm{ic}} R_{\mathrm{cav}}}\right)^2}. \tag{2.1}$$

For a variable detuning $\delta = \Phi_{\mathrm{rt}} - n2\pi$ from the resonance, the power enhancement can be written as:

$$\mathbb{E}(\delta) = \frac{1}{1 + \left[\frac{2\mathcal{F}}{\pi} \sin\left(\frac{\delta}{2}\right)\right]^2} \mathbb{E}_{\mathrm{R}}, \tag{2.2}$$

defining the *finesse* $\mathcal{F}$:

$$\mathcal{F} := \pi \frac{\sqrt[4]{R_{\mathrm{ic}} A_{\mathrm{cav}}}}{1 - \sqrt{R_{\mathrm{ic}} A_{\mathrm{cav}}}}. \tag{2.3}$$

The spectral enhancement of a resonator is shown in Figure 2.2. It exhibits periodically spaced resonances where the enhancement reaches $\mathbb{E}_{\mathrm{R}}$, which are also referred to as the *longitudinal modes* of the cavity. The *free spectral range* denotes the distance between two adjacent resonances. The *finesse* of a resonator can be defined as the ratio of its free spectral range and its resonance width, thus being a measure for its relative narrowness. The absolute spectral width, or *linewidth*, of the resonance is usually specified as its full width at 1/4-intensity, corresponding to its full width at half maximum (FWHM) in terms of field amplitude. For practical reasons it is most useful to specify the linewidth as a frequency $\Delta\nu$, with:

$$\Delta\nu = \frac{\mathrm{FSR}}{\mathcal{F}}, \tag{2.4}$$

in terms of the finesse and the *free spectral range* (FSR) in the frequency domain $\mathrm{FSR} = 1/t_{\mathrm{rt}}$. The finesse of a resonator depends exclusively on its total attenuation factor given by $R_{\mathrm{ic}} A_{\mathrm{cav}}$. In contrast, the enhancement additionally depends on the input-coupling transmission, resulting in different enhancement levels for different distributions of the total resonator losses between input coupler transmission and cavity losses. For optical resonators used as enhancement cavities, there are two particularly interesting cases to consider.

In the *impedance-matched* configuration ($R_{\mathrm{ic}} \approx A_{\mathrm{cav}}$), the resonant enhancement is:

$$\mathbb{E}_{\mathrm{R}} = \frac{\mathcal{F}}{\pi} = \frac{1}{T_{\mathrm{ic}}} = \frac{1}{1 - A_{\mathrm{cav}}} \qquad \text{(impedance matched)}. \tag{2.5}$$

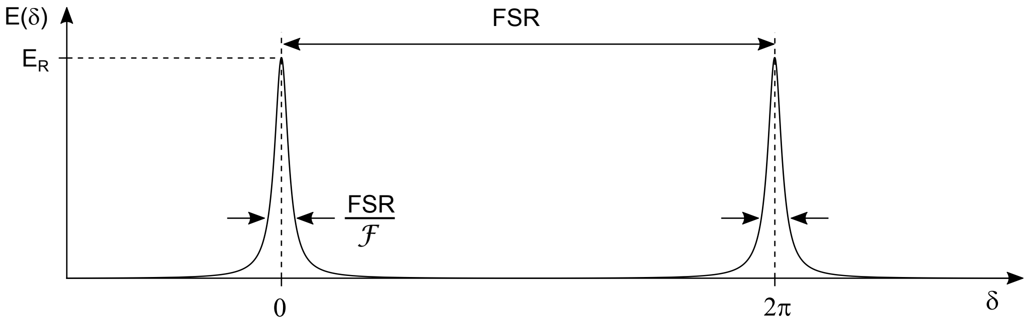

Figure 2.2: Resonance spectrum. The spectral enhancement $\mathbb{E}(\delta)$ for $T_{\mathrm{ic}} = 1 - A_{\mathrm{ic}} = 0.1$ is plotted over a detuning range of 4π. The range in between the resonances is called the free spectral range (FSR). The finesse $\mathcal{F}$ is a measure of the relative narrowness of the resonances.

For a given A_{cav}, the impedance matched configuration yields the highest possible $\mathbb{E}_{\mathrm{R}}$. Thus, it allows for the highest possible efficiency when driving purely lossy intracavity processes.

In an *input-coupler-limited* configuration ($R_{\mathrm{ic}} >> A_{\mathrm{cav}}$), the resonant enhancement is:

$$\mathbb{E}_{\mathrm{R}} \approx \frac{2\mathcal{F}}{\pi} = \frac{4}{T_{\mathrm{ic}}} \qquad \text{(IC limited).} \tag{2.6}$$

The input-coupler-limited configuration yields the highest $\mathbb{E}_{\mathrm{R}}$ for a given $\mathcal{F}$. As will become apparent in Sections 2.3 and 2.4, this holds advantages for the enhancement of ultrashort pulses, and for driving nonlinear processes associated with intracavity phase shifts. In practice, enhancement cavities are typically operated in the *over-coupled* regime between these cases [71].

2.2 The transverse cavity mode

In the previous section, the field distribution was assumed to depend solely on the longitudinal dimension z and time t. In the following, a brief introduction to the transverse field distribution in free-space cavities is given.[2] Throughout this section, the paraxial approximation is used, i.e. the wavefront normals are assumed to be nearly parallel to the propagation axis z. Furthermore, the discussion is restricted to the fundamental transverse cavity mode (TEM_{00}), or *Gaussian mode.*

Gaussian beams

Under the paraxial approximation, a beam $u(r, z)$ can be modeled as a plane wave which is spatially modulated by the function $\psi(r, z)$ (assuming circular symmetry):

$$u(r, z) = \psi(r, z)e^{-ikz}. \tag{2.7}$$

The most simple solution of the paraxial wave equation is the *Gaussian* beam. For this solution, it is instructive to express $\psi(r, z)$ in terms of the *complex beam parameter* $q(z)$ and the phase

---

[2] More thorough introductions to this topic can be found in [85], and [16].

term $P[q(z)]$ (which is itself al function of $q(z)$):

$$\psi(r,z) = \exp\left[-i\left(P[q(z)] + \frac{k}{2q(z)}r^2\right)\right], \tag{2.8}$$

with $k = \omega/v_\mathrm{p}$ being the angular wavenumber of the electric field. The complex beam parameter can be defined using the *wavefront radius* of the beam $R(z)$, and its $1/e^2$*-intensity radius* w:

$$\frac{1}{q(z)} = \frac{1}{R(z)} - i\frac{\lambda}{\pi w^2(z)}. \tag{2.9}$$

The phase term is most intuitively written in terms of the *Rayleigh length* z_R of the beam (equal to half its *confocal parameter*):

$$iP(z) = \ln\sqrt{1 + \frac{z}{z_\mathrm{R}}^2} - i\tan^{-1}\left(\frac{z}{z_\mathrm{R}}\right). \tag{2.10}$$

The Rayleigh length of a beam can be obtained from the complex beam parameter at an arbitrary point of propagation, with $z_\mathrm{R} = \mathrm{Im}\,[q]$. The first term of Equation 2.10 is simply a normalization factor which ensures energy conservation. The second term represents the *Gouy phase* of the beam. After propagation through a focus, the Gouy phase shift acquired by a Gaussian beam approaches π.

The complex beam parameter $q(z)$ fully characterizes the beam. Remarkably, it can be propagated using the ABCD matrices used in paraxial ray optics to calculate the propagation of rays. Here, A, B, C and D refer to the elements of the 2×2-matrix describing an optical system. In the ABCD formalism, the free-space propagation over a distance d is described by a matrix $\mathbf{S}(d)$, and the reflection of a spherical mirror with radius of curvature R by a matrix $\mathbf{M}(R)$, being:

$$\mathbf{S}(d) = \begin{bmatrix} 1 & d \\ 0 & 1 \end{bmatrix} \qquad \text{and} \qquad \mathbf{M}(R) = \begin{bmatrix} 1 & 0 \\ -2/R & 1 \end{bmatrix}. \tag{2.11}$$

The ABCD matrix $\mathbf{P}_\mathrm{rt}$ for a single roundtrip through an optical cavity is calculated by multiplying the individual matrices of the cavity elements in the reverse order of propagation, starting from an arbitrary reference point. The relation of the complex beam parameters of a Gaussian beam q before, and q' after one roundtrip parameterized by $\mathbf{P}_\mathrm{rt}$ through the cavity, is then given by:

$$q' = \frac{Aq + B}{Cq + D}, \qquad \text{with} \qquad \begin{bmatrix} A & B \\ C & D \end{bmatrix} = \mathbf{P}_\mathrm{rt}. \tag{2.12}$$

Cavity stability

An optical cavity is called *stable*, if a beam which is perfectly reproduced after a complete roundtrip through the cavity exists. This self-consistent *eigenmode* of a cavity can be found by requiring $q' = q$. Solved for $1/q$, this yields :

$$\frac{1}{q} = \frac{D - A}{2B} \pm \frac{1}{B}\sqrt{\left(\frac{A + D}{2}\right)^2 - 1}. \tag{2.13}$$

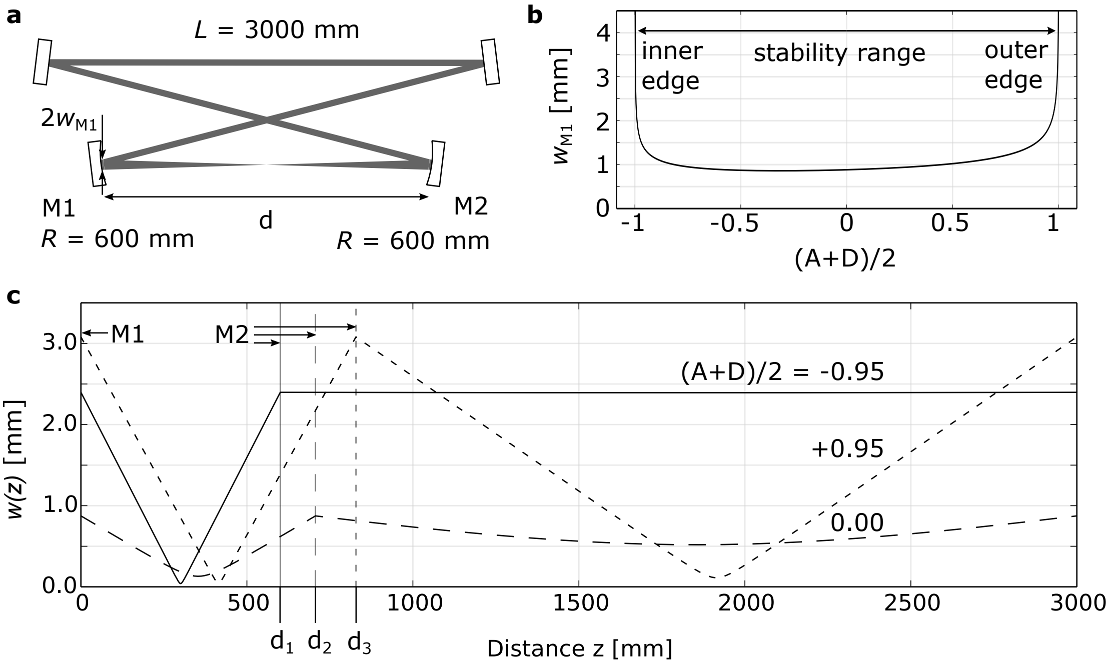

Figure 2.3: Stability dependence of the cavity caustic. **a** Symmetric bow-tie cavity with a total length of L, and two spherical mirrors M1 and M2 with radius of curvature R and distance d. **b** Beam radius w_{M1} on M1 with respect to the stability parameter $(A+D)/2$. **c** Beam caustic $w(z)$ along the optical axis z of the cavity for three values of the stability parameter and d. For $L = 3000\,\mathrm{mm}$ and $R = 600\,\mathrm{mm}$, the stability parameter values -0.95, 0, 0.95 correspond to $d_1 = 600.5\,\mathrm{mm}$, $d_2 = 706\,\mathrm{mm}$ and $d_3 = 828.5\,\mathrm{mm}$, respectively.

Since all elements of the ABCD matrix are real, the term under the square root must be negative for q to represent the complex beam parameter of a physical beam. The resulting inequality is called the *stability criterion*:

$$|A + D| \leq 2. \tag{2.14}$$

Only cavity configurations conforming with this criterion, i.e. being within the *stability range*, possess a well-defined eigenmode. Taking into account that the ABCD matrix elements are real, the values of R and w at the reference point can be deduced:

$$R = \frac{2B}{D - A} \quad \text{and} \quad w = \sqrt{\frac{2\lambda|B|}{\pi\sqrt{4 - (A + D)^2}}}. \tag{2.15}$$

The mode profile at other points can be obtained by propagating q further through the cavity. Th Gouy phase acquired over one cavity roundtrip is given by:

$$\Phi_{\mathrm{Gouy}} = \mathrm{sign}(B) \cos^{-1}\left(\frac{A + D}{2}\right). \tag{2.16}$$

Importantly, the eigenmode is stable with respect to perturbations [16]. The caustic as well as the stability of the cavity mode strongly depend on the position of the cavity configuration in the stability range. Figure 2.3 shows the caustic of a symmetric bow-tie cavity containing two spherical mirrors, and its mode size at different points for a range of values of their separation. At the edges of the stability range, the beam size on the spherical mirrors diverges. Close to the *inner edge of stability*, the cavity caustic between the spherical mirrors is tightly focussed, while the beam in the remaining cavity arms is nearly collimated. The roundtrip Gouy phase converges to π. The inner edge corresponds to a confocal imaging configuration. At the *outer edge of stability*, the caustic exhibits two foci, and the roundtrip Gouy phase converges to 2π.

So far, the cavity has been assumed to be radially symmetric. In the case of non-zero angles of incidence α, however, spherical mirrors exhibit *astigmatism*, breaking this symmetry. The effective radii of curvature in the *sagittal* and *tangential* planes defined by the angle of incidence, are given by:

$$R_\mathrm{x} = R\cos\alpha \quad \text{and} \quad R_\mathrm{y} = \frac{R}{\cos\alpha}, \tag{2.17}$$

with x and y denoting the corresponding transverse axes.

For elliptical Gaussian modes, the transverse field envelopes in the x-z and y-z planes can be separated, with

$$\psi(x, y, z) = \psi[q_\mathrm{x}(z), x]\psi[q_\mathrm{y}(z), y]. \tag{2.18}$$

In a planar cavity, the complex beam parameters can thus be calculated independently in the sagittal and tangential planes to account for the mirror astigmatism. As a result of the modified values for R, the stability ranges in the sagittal and tangential planes are then shifted up and down, respectively, in terms of d. In the central region of the stability range, the effect of a small angle of incidence of a few degree will be negligible. Moving towards the edges of the stability range, however, the inner and outer edges of stability are reached first in the sagittal and tangential planes, respectively. In effect, the mode profile becomes increasingly elliptic with increasing absolute values of the stability parameter. An interesting scheme to compensate for astigmatism by using a non-planar bow-tie cavity is presented in [86].

The spatial overlap

An important practical parameter for the enhancement in a cavity is the *spatial overlap* between the input and intracavity beams. The spatial overlap of two Gaussian beams with complex beam parameters $q_\mathrm{x,in}$ and $q_\mathrm{x,cav}$ in the x-z plane is given by the normalized and squared inner product of their transverse mode envelopes $\psi(q_\mathrm{x}, x)$ [87],

$$U_\mathrm{x} = \left| \int \psi(q_\mathrm{x,in}, x)\psi^*(q_\mathrm{x,cav}, x + \Delta x) \cdot e^{ik(\Delta\alpha_\mathrm{x} x)} \mathrm{d}x \right|^2, \tag{2.19}$$

with Δx being the positional, and $\Delta\alpha_\mathrm{x}$ the angular mismatch between the optical axes of the beams. The total spatial overlap $U_\mathrm{x,y}$ is simply $U_\mathrm{x,y} = U_\mathrm{x}U_\mathrm{y}$.

The spatial overlap acts as factor reducing the effective enhancement. It takes a value of one if both optical axes coincide, and both complex beam parameters are equal. Experimentally, the first condition corresponds to the correct *cavity alignment*, while the second is referred to as the *mode matching* between cavity and input beam. Importantly, the sensitivity of the cavity alignment errors with respect to a *mirror adjustment* error depends strongly on the cavity geometry and its stability parameter [88].

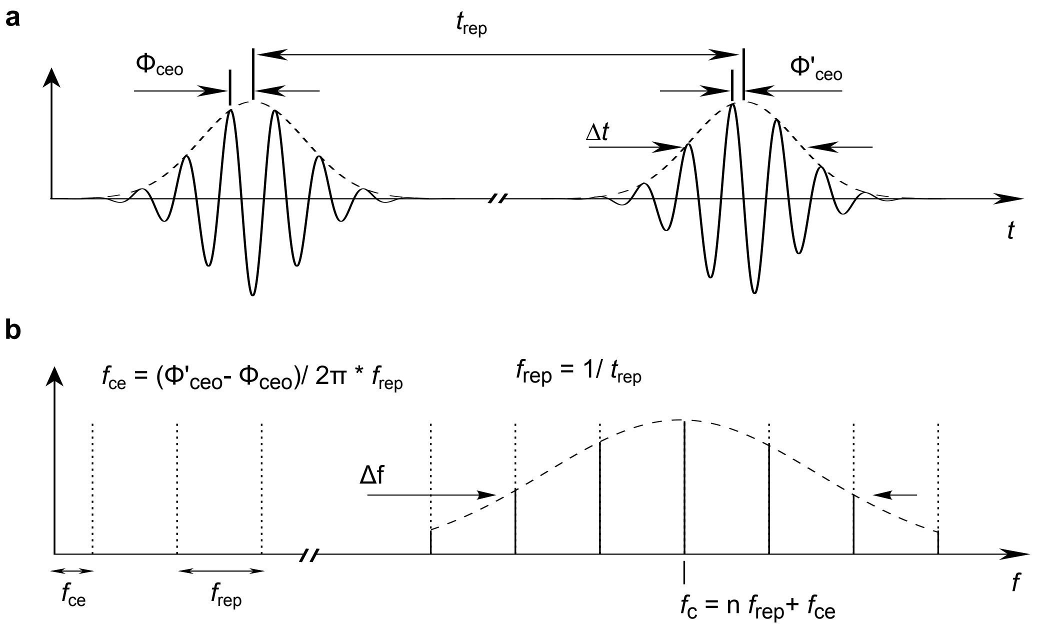

Figure 2.4: Frequency combs. **a** Two successive pulses of a continuous pulse train with repetition period t_{rep} and a pulse duration Δt. The relative phases between the electric field oscillation (straight line) and the envelopes (dashed lines) are given by ϕ_{ceo} and ϕ'_{ceo}. **b** The Fourier transformation of the pulse train yields a frequency comb defined by a carrier-envelope frequency f_{ce}, and a repetition frequency f_{rep}. The spectral envelope with the width Δf is centered at f_{c}, being the carrier frequency of the electric field oscillation in **a**.

2.3 Enhancement of femtosecond pulses

In the previous sections, excitation of the enhancement cavity with a single-frequency (i.e. a continuous-wave laser) was assumed. For the enhancement of short laser pulses, which are associated with broad spectra, the simultaneous enhancement of multiple frequencies is necessary. In particular, the frequency dependencies of the cavity roundtrip phase, the attenuation factor, and the input coupler reflectivity have to be taken into account.

Frequency combs

A light pulse can be described as a wave packet with a carrier frequency ω_{c} and a complex amplitude envelope defining its temporal shape (Fig. 2.4).[3] The relative phase of the electric field oscillation with respect to the temporal envelope is defined as the *carrier-envelope-offset* phase ϕ_{ceo}. In the frequency domain, a continuous train of pulses corresponds to a frequency comb, i.e. a number of discrete lines with a constant frequency spacing distributed under a spectral envelope covering a corresponding bandwidth. For a given shape of the spectral envelope, its width is inversely proportional to the Fourier limit of the temporal duration of the individual pulses. For a well-behaved spectral envelope, a central frequency, being the *carrier frequency* of the pulse train can be defined.

Being periodically spaced, the positions of all frequency comb lines can be parametrized

---

[3] A good textbook covering the optics of femtosecond pulses is [89]

by the line spacing f_{rep} and the absolute position of a virtual first line of the comb f_{ce}. In the time domain, the *repetition frequency* f_{rep} corresponds to the inverse repetition period of the temporal pulse envelopes. The *carrier-envelope frequency* f_{ce} is given by

$$f_{\text{ce}} = \frac{\phi'_{\text{ceo}} - \phi_{\text{ceo}}}{2\pi} f_{\text{rep}}, \tag{2.20}$$

with ϕ_{ceo} and ϕ'_{ceo} being the carrier-envelope-offset phases of two successive pulses. The carrier-envelope frequency thus represents the frequency with which the electric field oscillation slips with respect to the pulse envelope. For $f_{\text{ce}} = 0$ the electric fields of all pulses of a pulse train are identical. The *absolute* electric fields are also identical for $f_{\text{ce}} = f_{\text{rep}}/2$.

The spectral overlap

To enhance pulses in a resonator, the individual frequency comb lines have to overlap with the cavity resonances. This is equivalent to requiring the per-shot spectral phase shift of the pulse train $\Phi_{\text{fc}}(\omega)$, to be equal to the spectral phase that a pulse acquires during one roundtrip in the cavity $\Phi_{\text{cav}}(\omega)$ (Fig. 2.7). The frequency comb phase shift is defined by a function linear in ω:

$$\Phi_{\text{fc}}(\omega) = 2\pi \frac{f_{\text{ce}}}{f_{\text{rep}}} + \frac{1}{f_{\text{rep}}}\omega. \tag{2.21}$$

In the presence of intracavity dispersion, however, the roundtrip cavity phase $\Phi_{\text{cav}}(\omega)$ is not linear. A curvature of $\Phi_{\text{cav}}(\omega)$ corresponds to a nonuniform resonance spacing and thus limits the bandwidth over which a frequency comb can be enhanced (Fig. 2.7).

The quantity that one usually seeks to optimize in enhancement cavities is the effective power enhancement $\mathbb{E}_{\text{eff}}$, defined by the ratio of intracavity power to input power. For a frequency comb with spectral intensity I_{in}, this is given by:

$$\mathbb{E}_{\text{eff}} = \frac{\int I_{\text{cav}}(\omega)d\omega}{\int I_{\text{in}}(\omega)d\omega} = U_{\text{x,y}} \cdot \frac{\int U(\omega)\mathbb{E}_{\text{R}}(\omega)I_{\text{in}}(\omega)d\omega}{\int I_{\text{in}}(\omega)d\omega}, \tag{2.22}$$

introducing the spectrally resolved resonant enhancement $\mathbb{E}_{\text{R}}(\omega)$, which accounts for nonuniform spectral input coupling transmission and cavity attenuation, and the *spectral overlap* $U(\omega)$ between frequency comb lines and cavity resonances. $U_{\text{x,y}}$ represents the spatial overlap, which was discussed in Section 2.2. Note, that we assume $U_{\text{x,y}}$ to be frequency independent, which is typically a good assumption for the fiber amplifiers and fiber-based pulse compression setups used in this thesis. The spectral overlap can be defined as:

$$U(\omega) = \left(1 + \left[\frac{2}{\pi}\mathcal{F}(\omega)\sin\left(\frac{1}{2}\Delta\Phi(\omega)\right)\right]^2\right)^{-1}. \tag{2.23}$$

The spectral overlap depends on the spectrally-resolved finesse $\mathcal{F}(\omega)$ and the roundtrip phase mismatch $\Delta\Phi_{\text{rt}}(\omega) = \Phi_{\text{cav}}(\omega) - \Phi_{\text{fc}}(\omega)$, which corresponds to the detuning of each frequency comb line from the closest resonance. The spectral overlap is one for $\Delta\Phi_{\text{rt}}(\omega) = 0$, and decreases with increasing $|\Delta\Phi_{\text{rt}}(\omega)|$. The sensitivity of $U(\omega)$ with respect to $\Delta\Phi(\omega)$ depends on the $\mathcal{F}(\omega)$. For the overlap to exceed a value of 0.5, the following condition applies:

$$|\Delta\Phi_{\text{rt}}(\omega)|_{0.5} \leq \frac{\pi}{\mathcal{F}(\omega)} \tag{2.24}$$

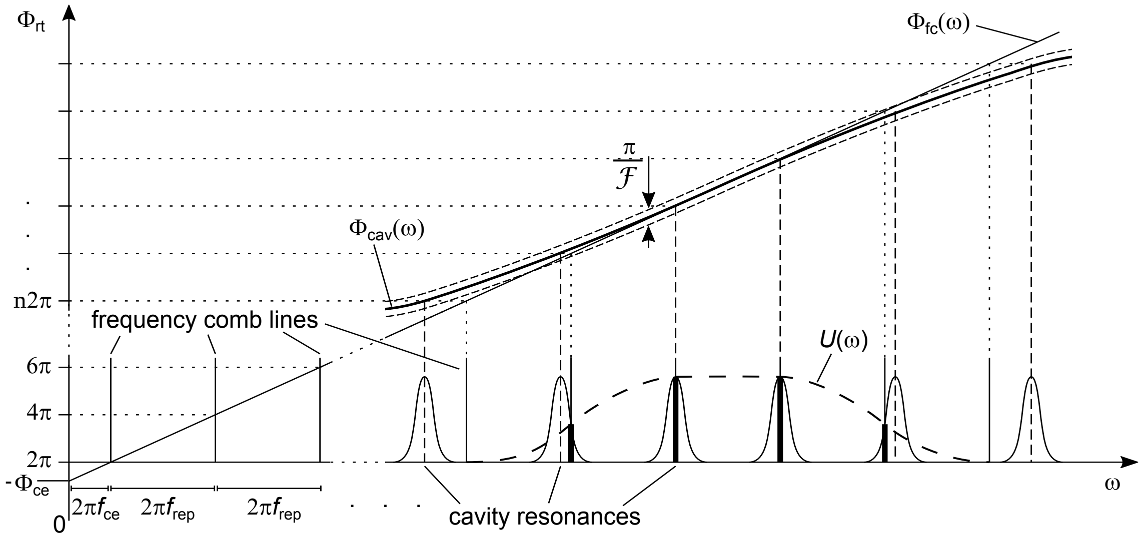

Figure 2.5: Spectral roundtrip phase and resonance spacing. The cavity is resonant for frequencies for which the cavity roundtrip phase $\Phi_{\mathrm{cav}}(\omega)$ is equal to an integer multiple of 2π. The width of the cavity resonances is given by the finesse $\mathcal{F}$ of the cavity. A curvature in the roundtrip phase results in an uneven frequency spacing of the resonances. For specific values of the carrier-envelope frequency f_{ce} and the repetition frequency f_{rep} defining its pulse-to pulse phase $\Phi_{\mathrm{fc}}(\omega)$, there is an optimum overlap $U(\omega)$ between input frequency comb and cavity resonances. In the time domain, the simultaneous enhancement of frequency comb lines corresponds to the enhancement of laser pulses. The maximum bandwidth and minimum pulse duration is limited by the spectral width of $U(\omega)$.

If $\Phi_{\mathrm{cav}}(\omega)$ is sufficiently well behaved, there is a set of frequency comb parameters $(f_{\mathrm{ce}}^{\mathrm{opt}}, f_{\mathrm{rep}}^{\mathrm{opt}})$ associated with a clear maximum of $\mathbb{E}_{\mathrm{eff}}$. The corresponding optimal roundtrip phase mismatch $\Delta\Phi_{\mathrm{rt}}^{\mathrm{opt}}(\omega)$ is then:

$$\Delta\Phi_{\mathrm{rt}}^{\mathrm{opt}}(\omega) = \Phi_{\mathrm{cav}}(\omega) - \frac{1}{f_{\mathrm{rep}}^{\mathrm{opt}}}\left(2\pi f_{\mathrm{ce}}^{\mathrm{opt}} + \omega\right). \tag{2.25}$$

In general, the optimal comb parameters for cavity enhancement can depend on the shape of $\Phi_{\mathrm{cav}}(\omega)$, the laser spectrum, and the spectral modulations of the resonant enhancement and finesse of the cavity. If $\Delta\Phi_{\mathrm{rt}}^{\mathrm{opt}}(\omega)$ is sufficiently small to allow for an optimal spectral overlap near unity within the laser bandwidth, however, the optimal comb parameters are determined mainly by $\Phi_{\mathrm{cav}}(\omega)$.

The roundtrip dispersion in practice[4]

In the following, the practical importance of the properties of $\Phi_{\mathrm{cav}}(\omega)$ are discussed for an approximately linear spectral cavity phase over the relevant spectral bandwidth. In this case, it is instructive to associate the terms appearing in Eq. 2.25 with the terms of the Taylor series of $\Phi_{\mathrm{cav}}(\omega)$ at the frequency ω_{c} of the central cavity resonance:

$$\Phi_{\mathrm{cav}}(\omega) = n2\pi + \Phi_1(\omega_{\mathrm{c}})(\omega - \omega_{\mathrm{c}}) + \frac{1}{2!}\Phi_2(\omega_{\mathrm{c}})(\omega - \omega_{\mathrm{c}})^2 + \ldots \quad , \tag{2.26}$$

---

[4] An excellent review covering this and other aspects of femtosecond enhancement cavities for high-order harmonic generation was presented by Mills *et al.* [71]

where $\Phi_0(\omega_c) = n2\pi$ by choice of ω_c.

The carrier-envelope-offset phase shift per roundtrip $\Phi_{ce} = -\Phi_1\omega_c$ determines the *optimum offset frequency* (OOF) f_{ce}^{opt}, of the cavity. To allow for the enhancement of waveform-stable pulses, it is required that $\Phi_{ce} = 0$ (or $\Phi_{ce} = \pi$, for applications which are insensitive to the sign of the field oscillation, such as isolated attosecond pulse generation). The OOF is determined by the Gouy phase of the cavity caustic, the dispersion of the cavity mirrors, and the dispersion of intracavity media if present. The cavity OOF is usually stable except for slow drifts that may be caused by thermal effects in intracavity media. Depending on the phase noise properties of the laser, the laser f_{ce} needs to be actively stabilized to achieve efficient low-noise enhancement [90].

The *1st-order* term Φ_1 corresponds to the roundtrip *group delay* (GD), i.e. the cavity's optical path length, and determines f_{rep}^{opt}. In the macroscopic enhancement cavities used in this thesis, the cavity length is subject to significant mechanical noise. To achieve stable enhancement, the detuning of the frequency comb lines close to its central wavelength need to be actively stabilized to zero. In the experiments presented in this thesis, this was achieved by generating a Pound-Drever-Hall error signal [91, 92], to feed a servo which acts on a piezoelectric and/or electro-optic actuator in the laser oscillator.

The *higher-order* terms Φ_2, Φ_3, ... correspond to the roundtrip *group-delay dispersion* (GDD), the *third order dispersion* (TOD), and so forth. These terms represent the curvature of the cavity roundtrip phase. The presence of this curvature limits the spectral width over which the phase mismatch $\Delta\Phi_{rt}^{opt}$ is negligible, and thus the bandwidth of the optimal spectral overlap $U(\omega)$ (Fig. 2.5). The higher-order contributions to the cavity phase comprise the dispersion of the cavity mirrors upon reflection, and, if present, the dispersion of intracavity media. The shape of the spectral phase of dielectric *quarter-wave-stack* coatings typically used as mirrors in enhancement cavities, is characterized by an inflection point at their central wavelength. With increasing positive and negative spectral distance to this point, the absolute value of the mirror phase curvature increases (in negative and positive directions, respectively) (Fig. 2.5). In the absence of intracavity media, i.e. in a cavity containing no transmissive optics and operated in vacuum, it is the spectral mirror phase that poses the main limitation to the maximum width of the enhanced intracavity spectrum $I_{cav}(\omega)$ [51].

For a given mirror dispersion and number of mirrors, there is a trade-off between cavity finesse and bandwidth (Eq. 2.24). Thus, it is advantageous to work with a cavity close to the input-coupler-limited configuration to maximize the cavity enhancement (Eq. 2.6). The finesse of enhancement cavities for HHG is typically in the range of 100 to 1000. Thus, $\Delta\Phi_{rt}(\omega)$ must be within about $0 \pm (3 - 30)$mrad within the desired spectral bandwidth to achieve efficient enhancement.

Multilayer mirrors

The spectral reflectivity and phase of dielectric multilayer coatings are determined by the interference of all reflections within the many layers comprising the coating, and thus depends on the individual thicknesses of the layers. These can be numerically optimized to approach a desired (but not arbitrary) target reflectivity and phase. An important property of the resulting coating design is its sensitivity with respect to the optical thickness errors of the layers, which invariably occur during production. Empirically, the sensitivity of coating designs for highly-reflective mirrors with a linear spectral phase increases with the bandwidth over which the phase is specified.

As a general rule, the bandwidth supported by the phase of dielectric cavity mirrors for a given finesse scales with the contrast of the refractive indices of the two materials making up the mirror coatings [93]. A higher refractive index, however, indicates a smaller bandgap, resulting in a lower damage threshold [94, 95]. Thus, there is a trade-off between mirror damage threshold on the one hand and intracavity bandwidth (and pulse duration) on the other. Typical material choices are SiO_2/Ta_2O_5 for a high damage threshold and low absorption, or SiO_2/Nb_2O_5 for larger bandwidth.

Enhancement of high-power pulses[5]

The maximum peak intensity supported by cavity mirrors is limited by dielectric breakdown of the highly-reflective coatings leading to irreversible mirror damage, with typical damage thresholds being in the range of $10^{11}\,\mathrm{W\,cm^{-2}}$ [72] for pulse durations in the few-hundred-femtosecond range. In effect, the attainable peak power in an enhancement cavity is limited by the cavity mirror on which the beam diameter is smallest. Thus, an ideal cavity geometry optimized for high peak intensities in the focus must exhibit large mode profiles on all mirrors, and a tightly focused waist. Independent of the cavity geometry, these requirements can be met best by setting up the cavity close to one of its stability edges, where the mode size on the focusing mirrors diverges. However, there is a major drawback to the operation of cavities close to the stability edges: Together with the mode size divergence, the sensitivity of the cavity alignment with respect to mirror alignment errors, and the sensitivity of the cavity mode with respect to changes to the focusing power of mirrors, e.g. caused by thermal lensing, tend to diverge.

The alignment sensitivity of different cavity geometries suitable for obtaining large modes on all mirrors was recently investigated by Carstens *et al.* [73]. In this work, symmetrical bow-tie cavities set up close to the inner edge of the stability range (Fig. 2.3) were identified as the most robust design for high-power enhancement cavities. In general, the alignment sensitivity of cavities tends to be much more severe at edges of stability where the Gouy phase approaches a value of 2π, than at edges where it approaches π.

For the operation of cavities at high average powers, absorption of intracavity light leads to thermal gradients in the cavity mirror substrates, and in transmissive cavity optics, if present. The resulting mirror surface deformation and the temperature dependence of the refractive index in transmissive optics distort the transverse phase and shape of the cavity mode. Depending on their profile, these distortions act as thermal lenses and/or aberrations.

In a mirror-only bow-tie cavity close to the inner edge of stability, the defocussing thermal lenses of the mirrors push the cavity configuration closer to the stability edge, leading to an increase in mode size. A simple approximation for the focusing power R^{-1}_{mirror} of thermal lens on a mirror is [97]:

$$R^{-1}_{\mathrm{mirror}} \propto -A_{\mathrm{coat.}} \frac{\alpha_{\mathrm{subst.}}}{\kappa_{\mathrm{subst.}}} \frac{P}{w^2}, \tag{2.27}$$

with the incident power P, the absorption fraction of the coating $A_{\mathrm{coat.}}$, and the thermal conductivity $\kappa_{\mathrm{subst.}}$ and thermal expansion coefficient $\alpha_{\mathrm{subst.}}$ of the mirror substrate.

---

[5] The power scalability of enhancement cavities was thoroughly investigated in a recent dissertation [96].

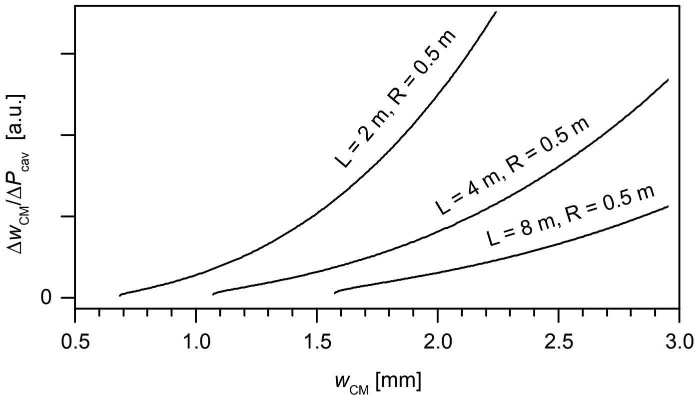

Figure 2.6: Thermal sensitivity. Plots of the thermal sensitivities $\Delta w/\Delta P$ of symmetric bow-tie cavities of total lengths L, and mirror curvatures R close to the inner edge of stability, for a continuous range of initial mode sizes w_{CM} on the focusing mirrors.

Using this approximation and the ABCD-formalism introduced in Section 2.2, the thermally-induced cavity mode change upon an incremental increase in intracavity power $\frac{\Delta w}{\Delta P}$, being a good metric for the *thermal sensitivity* of a cavity, can be calculated [74, 96, 98]. Figure 2.6 plots the thermal sensitivity versus the initial mode radius for three symmetric bow tie cavities of different lengths close to the inner edge of stability. The sensitivity of the cavity mode with respect to thermal lenses diverges at the edges of the stability zone, i.e. for large initial mode sizes. For a given initial mode size, the thermal sensitivity decreases strongly with the cavity length.

2.4 Nonlinear phase modulation

In the last section the limitation to the peak and average pulse power in enhancement cavities was identified as a combination of thermally-induced lensing effects and nonlinearly-induced optical damage. For many practical applications of enhancement cavities, however, another group of nonlinear effects limit the enhancement at a much lower peak power. These are *self-action* effects, i.e. effects in which a beam of light modifies its own propagation by means of the nonlinear response of a material medium [99]. In the context of femtosecond enhancement cavities, the most important self-action effects are temporal phase modulations caused by the nonlinear refractive index of intracavity media.

Neglecting the transverse field distribution, the propagation of a light pulse with the temporal field envelope A through a nonlinear medium over an arbitrarily small distance L can be approximated in the comoving frame:

$$A(z_0 + L, \tau) = A(z_0, \tau) e^{i\Phi_{\mathrm{NL}}(z_0,\tau,L)}, \tag{2.28}$$

with $\Phi_{\mathrm{NL}}(z_0, \tau, L)$ being the nonlinear phase shift, provided that the changes to the pulse envelope are small, i.e. the nonlinear response does not change over the distance L, and nonlinear loss terms can be neglected.

For intracavity HHG, the two main sources for nonlinear phase shifts arise from plasma

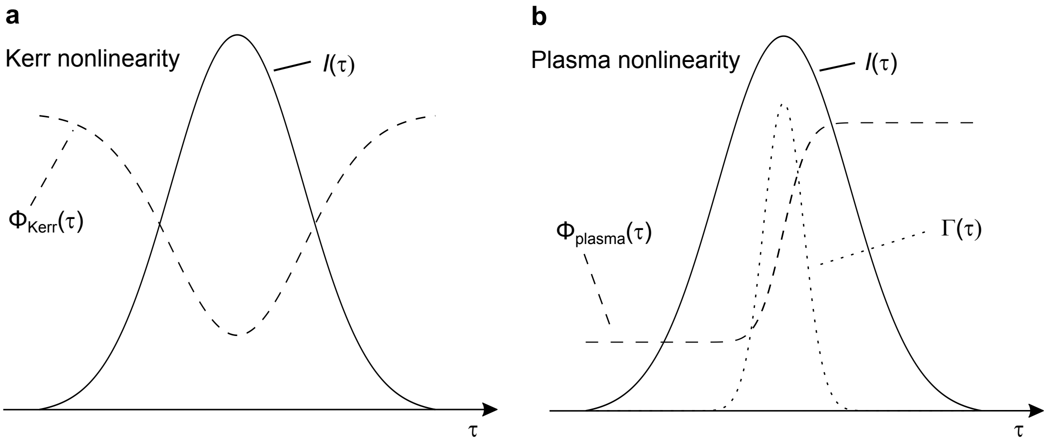

Figure 2.7: Nonlinear phase shifts. Temporal phase shifts produced by a sech^2-shaped pulse upon propagation through a medium exhibiting a Kerr nonlinearity(**a**), and an ionizable medium (**b**) for the case of a small ionization fraction.

generation in the gas target[6] and from the Kerr effect. The latter occurs both in the gas target, and in the transmissive cavity optics, which are used for XUV output coupling in many cavity HHG setups. The Kerr effect is particularly relevant to stack-and-dump cavities, which so far rely on transmissive optics for optical switching [63, 101]. The Kerr phase shift $\Phi_{\mathrm{Kerr}}(t)$ reads [99]:

$$\Phi_{\mathrm{Kerr}}(\tau) = -\frac{\omega_0}{c} I(\tau) n_2 L, \tag{2.29}$$

with n_2 being the second-order nonlinear index of refraction.

The plasma phase shift $\Phi_{\mathrm{ion}}(t)$ in a gas target with the number density n_{gas}, and an initial density of ionized atoms $n_{\mathrm{e}}^{\mathrm{init}}$ can be approximated as [100]:

$$\Phi_{\mathrm{plasma}}(\tau) = r_{\mathrm{e}} \lambda_{\mathrm{c}} (n_{\mathrm{gas}} - n_{\mathrm{e}}^{\mathrm{init}}) \exp\left[- \int_{-\infty}^{\tau} \Gamma\left[I(\tau')\right] \mathrm{d}\tau' \right] L, \tag{2.30}$$

using the the ionization rate $\Gamma\left[I(\tau')\right]$, the central wavelength λ_{c} and the classical electron radius r_{e}. In the low-intensity regime, the ionization rate scales as I^n, with $n = I_{\mathrm{p}}/\hbar\omega_{\mathrm{c}}$ being the number of photons required to reach the ionization potential I_{p} [102]. An analytical model for $\Gamma\left[I(\tau')\right]$ valid over a broader parameter range was introduced by Perelomov, Popov and Terent'ev (PPT) [103]. For ionization events occurring at a multi-megahertz rate, the initial ionized fraction $n_{\mathrm{e}}^{\mathrm{init}}$ can be nonzero, forming the steady-state ionization fraction. Its value depends on the fraction of atoms ionized per pulse, the recombination rate between pulses, the repetition rate, and the gas exchange in the focal volume [64]. Figure 2.7 shows the nonlinear phase shifts associated with the Kerr effect and plasma generation for a Gaussian temporal intensity envelope. In general, a nonlinear phase shift in the temporal domain alters both the spectral phase and *spectral shape* of the pulses in the frequency domain, i.e. it generates new frequency components [99]. There are three major repercussions for the operation of nonlinear enhancement cavities.

---

[6] The effects of plasma generation in femtosecond enhancement cavities were introduced in greater detail in a recent dissertation [100]

First, the nonlinear phase shift adds to the cavity roundtrip phase and results in an intensity-dependent detuning of the cavity resonances. The Kerr effect will generally shift the cavity resonances to lower frequencies, while the presence of plasma results in higher cavity resonance frequencies. The resulting coupling between power build-up in the cavity and its roundtrip phase leads to interesting nonlinear cavity dynamics such as optical bistability [99]. These dynamics complicate the frequency locking between driving laser and cavity, typically increasing the intensity noise in the cavity, and making an in-lock adaptation of the servo parameters necessary [64, 71].

Second, a temporal phase shift also results in the creation of new spectral components. The Kerr effect typically produces symmetric spectral broadening, while the temporal phase shift associated with ionization results in a blue shift of the spectrum. As a result, the spectral overlap with the driving laser pulses, and thus the enhancement, decreases. This effect currently presents a main limitation for the power scalability of intracavity HHG and stack-and-dump schemes [63–65].

Third, for a nonuniform spatial distribution of the driving field, e.g. a Gaussian beam, the transverse distribution of the nonlinear phase shift results in Kerr and plasma lensing effects, and aberrations [64, 71].

Temporal optical solitons

A particularly interesting regime for nonlinear pulse propagation exists in media exhibiting both a Kerr nonlinearity and second-order dispersion. The pulse propagation in such a medium can be expressed in the comoving frame by the *nonlinear Schrödinger equation* [99]:

$$\partial_z A(\tau, z) + i\beta_2 \partial_\tau^2 A(\tau, z) = i2n_0\epsilon_0 n_2\omega_0 |A(\tau, z)|^2 A(\tau, z), \tag{2.31}$$

with β_2 being the group velocity dispersion of the medium. This equation has solutions for which the group velocity dispersion term on the left hand side completely compensates for the Kerr term on the right hand side. Such solutions represent *solitons*, i.e. pulses which travel through a nonlinear dispersive medium without any change of their temporal and spectral shapes. The fundamental, or first-order soliton is given by a hyperbolic-secant-shaped temporal envelope:

$$A(z, \tau) = A_0 \mathrm{sech}\left(\frac{\tau}{\tau_0}\right) e^{i\kappa z}, \tag{2.32}$$

where the temporal width τ_0 and the phase shift upon propagation κ are functions of the peak intensity $|A_0|^2$, reading:

$$\tau_0^2 = -\frac{\beta_2}{n_2}\frac{1}{n_0\epsilon_0\omega_0}\frac{1}{|A_0|^2} \quad \text{and} \quad \kappa = -\frac{\beta_2}{\tau_0^2}. \tag{2.33}$$

For a material of a given dispersion and nonlinear refractive index, Equation 2.32 thus represents a continuous range of fundamental soliton solutions which exhibit a decreasing pulse duration with increasing peak intensity. To represent physical pulses with positive values of the intensity and squared pulse width, n_2 and β_2 must be of opposite sign. Because of this condition, “bright” soliton pulses only exist in the anomalous (negative) dispersion regime, while a positive dispersion can support more exotic “dark” solitons. Importantly, solitons are stable against perturbations, and arbitrary pulses of sufficient pulse energy will converge to a soliton pulse upon propagation along a suitable medium [104].

Temporal solitons are an important concept in the context of fiber optics, where mode guiding facilitates low-loss propagation over long distances in a homogeneous medium [104]. As *dissipative solitons*, generalized solutions which also account for loss and gain mechanisms, they also play a major role for the mode locking of lasers [17, 105], and have more recently been demonstrated in passive microresonators [10, 11, 106] and fiberresonators [107].

Chapter 3

Outline of results

In this chapter the individual studies comprised in this thesis are summarized and motivated in the context of the research objective. The full results are presented in the form of five published articles and one recently submitted manuscript, compiled in Part II of this thesis. The five experimental studies relevant to cavity-enhanced HHG are arranged in the order in which the related work was performed. A further article outlining a proposal for a power-scalable cavity dumping device is appended.

3.1 Power scalability in the presence of thermal lensing

Prior to this work, the limitations to the power scalability of (empty) enhancement cavities were investigated, and identified as a combination of intensity-induced mirror damage, and the sensitivity of the cavity mode with respect to thermally induced deformations of the mirror surfaces and thus distortions of the spatial roundtrip phase [72, 74, 98]. The latter effect results in thermal lensing, causing changes of the cavity mode size, and aberrations, causing mode deformation and losses to the fundamental Gaussian beam (Section 2.3). By optimizing the mirror properties for minimal surface deformation, record values for the average power in mirror-only enhancement cavities were achieved [74]. Still, the cavity was subject to significant thermally induced mode distortions. Also, many cavity HHG experiments [23, 108–111] rely on a transmissive optic, usually a thin Brewster plate, for XUV output coupling, raising the question how such elements affect the power scalability of enhancement cavities.

Balancing of thermal lenses in enhancement cavities[1]

In the first study presented in this thesis, we extended our previous power scaling experiments [74] to cavities including Brewster plates. In particular, we developed a scheme for power-independent thermal lens compensation, exploiting that the shapes of the spatial phase distortions caused by laser-induced mirror deformations on the one hand, and refractive index changes in transmissive elements on the other, are similar but of opposite sign. As a result,

---

[1] The full study was published on February 27th, 2015 in *Optics Letters*[112], and is included together with a statement of author contributions in Chapter 5.

the thermal lenses caused by the cavity mirrors and a Brewster plate can compensate for each other. To this end, the strength of lensing effects in all components must be carefully balanced.

We investigated the balancing of thermal lenses in enhancement cavities theoretically, modeling the laser-induced spatial phase distortions with finite element simulations, and performed cavity experiments using a high-power ytterbium-fiber amplifier system [69]. To achieve a compensation of thermal lenses with the available Brewster plates we installed mirrors with higher thermal deformation coefficients than those used in [74]. The model and experimental results show excellent agreement. We showed that thermal lenses can be used to compensate the astigmatism of the cavity mirrors at a given power. We demonstrated that the thermal lensing behavior of a thin Brewster plate can be fine-tuned by convective cooling with a directed gas flow. With this technique, we achieved a power-independent cavity mode size for intracavity average powers up to 160 kW. Furthermore, the mode deformation, being an indicator for aberrations, is significantly reduced with respect to the same cavity without the Brewster plate.

This work demonstrated that the choice of Brewster plate material, thickness, orientation and cooling, presents degrees of freedom to control the mode shape evolution with increasing power. The average power reported here surpasses previously reported average powers in enhancement cavities with transmissive elements by more than an order of magnitude [110], but is significantly lower than that achieved in an optimized mirror-only enhancement cavity [74]. The presented scheme will be of particular interest for cavity experiments requiring transmissive elements for XUV output coupling or other purposes, such as intracavity pulse compression (Chapter 9) or other frequency conversion mechanisms.

3.2 Power scalability in the presence of ionization

In the presence of laser-induced plasma generation in a gas target, a prerequisite for HHG, the peak intensity in the enhancement cavity is limited by the associated temporal phase shifts, most importantly those occurring on the time scale of the pulses. The resulting intensity clamping sets in at a specific value of this phase shift, which depends on the finesse [64]. While models which can qualitatively describe the processes at the bottom of this limitation have been introduced in previous studies [64, 65], a quantitative, experimentally validated model of intracavity plasma generation remained highly desirable to allow for a global optimization of cavity HHG.

Femtosecond enhancement cavities in the nonlinear regime[2]

Within the framework of this thesis, experimental work for the validation of an ab-initio model developed primarily by Simon Holzberger was conducted. In particular, the intracavity spectrum, peak intensity and the relative spectral phase between intracavity pulses and driving pulses were measured in presence of a xenon gas target, for three different pulse durations. To this end, we used driving pulse durations of down to 30 fs from a nonlinearly-compressed fiber amplifier system [67], resulting in an intracavity pulse duration of down to 35 fs, limited by

---

[2] The full study was published on July 8th, 2015 in *Physical Review Letters*[115], and is included together with a statement of author contributions in Chapter 6.

the cavity mirror dispersion. For precise measurements of the nonlinearly-induced spectral phase we employed spatial-spectral interferometry, which has previously been shown to allow measurements of the linear intracavity dispersion with a sensitivity of less than 1 fs^2 [114].

The numerical model exhibited quantitative agreement with the experimental results. Subsequently, the model was used to derive an empirical scaling law for the *clamping intensity*, i.e. the peak intensity in the gas target, for which a further increase in input laser power results in negligible increases of the intracavity power. The scaling law shows that the clamping intensity increases with decreasing finesse, pulse duration, and the product of gas density and target length (Chapter 6, Eq. 4 and Table 1). As a result, it is generally desirable to decrease the experimental values of these parameters as far as possible to optimize HHG efficiency, in particular for high photon energies. In practice, the gas density is usually an exception to this rule, since an optimum gas density is determined by the phase matching condition.

Furthermore, the numerical model was used to theoretically investigate a novel scheme for exploiting the nonlinear plasma phase shift for the efficient temporal compression of intracavity pulses. The concept relies on the use of input coupling mirrors with a tailored spectral reflectivity. It was shown that for an optimized spectral reflectivity curve, in theory a stable steady state exists in which the temporal plasma phase facilitates efficient intracavity pulse compression by a factor of five, and a significantly increased XUV conversion efficiency compared to a "standard approach" cavity, employing input couplers of approximately uniform reflectivity.

3.3 Towards waveform-stable few-cycle pulse enhancement

In the previous section, decreasing the intracavity pulse duration was identified as a promising approach to increase conversion efficiencies in standard-approach cavity HHG. A significantly shorter intracavity pulse duration than those supported by standard quarter-wave-stack mirrors could furthermore enable the generation of isolated attosecond pulses via cavity HHG with temporal gating techniques [78, 80, 81]. Apart from progress on decreasing the intracavity pulse duration, isolated attosecond pulse generation requires cavities suitable for enhancing *waveform-stable* pulses, i.e. having an optimum offset frequency of zero or equaling half the repetition rate.

Both the optimum offset frequency and the bandwidth, and thus minimum pulse duration of cavities depend on the spectral phase of the cavity mirrors. To optimize the spectral cavity phase we implemented novel mirror designs, and used different designs in a single cavity to compensate for production errors.

Enhancement cavities for zero-offset-frequency pulse trains[3]

To control the optimum offset frequency of a broadband enhancement cavity, we implemented two mirror designs with slightly differing carrier-envelope phase shift upon reflection. The mirror designs were based on quarter-wave stacks using $\mathrm{SiO_2/Nb_2O_5}$ layers, with small variations of the uppermost layers changing the phase upon reflection, and achieving a slight

---

[3] The full study was published on April 14th, 2015 in *Optics Letters*[113], and is included together with a statement of author contributions in Chapter 7.

increase in bandwidth. Implementing these mirrors in a femtosecond enhancement cavity, we determined the optimum offset frequency for different mirror combinations. We found excellent agreement of the measured carrier-envelope phase shift upon reflection with the mirror design. For a suitable mirror combination, we demonstrate a cavity set up close to its inner edge of stability with an optimum offset frequency of zero, and supporting a pulse duration of 30 fs. Furthermore, we showed that the mirror design variations introduced for offset frequency control do not compromise the damage threshold of the coatings.

Enhancement cavities for few-cycle pulses[4]

To further reduce the supported pulse duration, we investigated mirrors based on more complex multilayer designs. To characterize the spectral phase of the mirrors we implemented a sensitive multi-pass spatial spectral interferometry setup. We found significant deviations of the measured spectral phase of the produced coatings from the designs. Multiple coating runs yielded mirrors with approximately opposite spectral phase curvatures, allowing the setup of a broadband enhancement cavity with an optimum offset frequency equaling half the repetition rate. The enhanced intracavity spectrum, and its relative spectral phase show excellent agreement with simulations based on the mirror phase measurements, confirming their utility. A thorough characterisation of the intracavity pulse yielded a duration of 19 fs. The cavity bandwidth could be further extended by introducing additional dispersion in the form of 24 mbar of air, resulting in a -10-dB bandwidth of 195 nm.

3.4 Intracavity pulse compression

While the efforts towards shorter pulse durations described in the previous section yielded a significant improvement over the state of the art, the results were clearly close to the current technological limits in terms of coating deposition accuracy and multilayer design, and thus marked the lower limit of pulse durations achievable in linear femtosecond enhancement cavities, and the standard approach of cavity HHG. In a next step, we followed up on the encouraging simulations on the intracavity pulse compression in nonlinear enhancement cavities with spectrally tailored input coupling. While the simulations were performed for intracavity plasma phase shifts, we decided to experimentally investigate this scheme for a cavity exhibiting a Kerr nonlinearity [63, 117]. For this case, the generation of spatial and temporal *cavity solitons* in microresonators and fiber resonators [10, 11, 106, 107, 118, 119] has recently attracted significant interest [120].

The resonator architectures in which cavity solitons have been demonstrated to date are based on total internal reflection inside of a Kerr medium, with transverse mode diameters on the micrometer scale, and thus differ fundamentally from the macroscopic free-space enhancement cavities subject to this thesis. Moreover, all previous soliton cavities exhibited an approximately uniform spectral input-coupling transmission. In this case, the coupling efficiency of an external laser driving the soliton cavity is limited by the temporal and spectral overlap with the intracavity pulse [121, 122]. The effective average power enhancement in

---

[4] The full study was published on January 11th, 2017 in *Optics Letters*[116], and is included together with a statement of author contributions in Chapter 8.

a cavity soliton state with respect to the linear resonant enhancement is thus decreased at least by a factor proportional to the spectral broadening or temporal compression factor of the soliton with respect to the driving laser. In other words, peak-power enhancement in a cavity soliton state cannot surpass the resonant power enhancement that would be achieved in the same cavity in the absence of nonlinearity.

Temporal solitons in free-space enhancement cavities[5]

We investigated a more efficient concept for temporal cavity soliton generation based on a spectrally tailored input coupler reflectivity conceptually similar to the proposal in Chapter 6, in a free-space femtosecond enhancement cavity. The Kerr nonlinearity was generated in a Brewster plate similar to those used for XUV output coupling and in our demonstration of thermal-lens balancing. The input coupling mirror exhibited a high reflectivity over its spectral range with exception of narrow notch in the center of its spectral range, where its transmission is about 1%. Its spectral width and position approximately match the spectrum of the 350-fs pulses delivered directly by the ytterbium-fiber amplifier of the driving laser. The roundtrip dispersion of the cavity was optimized using the mirror characterization scheme introduced in Chapter 8. Furthermore, we introduced a locking scheme using an auxiliary laser that is insensitive to the nonlinear cavity phase shifts.

Controlled detuning of the driving laser lock allowed for the generation of intracavity solitons with a duration of 37 fs. The average power enhancement in this soliton state was 366, and the peak power enhancement was 3200. The linear power enhancement in the same cavity was 444, applying both to the peak and average power, for the same laser spectrum at a much lower power. The exceptional peak power enhancement in the soliton cavity state, achieved at a temporal compression factor above nine significantly surpasses the enhancement of linear cavities capable of supporting similar pulse durations. We found that the intracavity soliton reproduces the driving frequency comb structure, and found an interesting low-frequency intensity-noise suppression mechanism. Notably, the nonlinear phase shift at which the soliton operates far exceeds the phase shift for intensity clamping in standard-approach nonlinear cavities at similar peak power enhancements.

3.5 Proposal for cavity dumping

The last manuscript included in this thesis proposes a novel concept for periodic dumping of pulses from optical cavities. While not directly connected to cavity-enhanced HHG, the use of passive resonators to store energy from a pulse train in a pulse circulating in the cavity, which is then periodically released from the cavity, has been subject of early work on enhancement cavities [51, 124–126], and has recently found renewed interest in the context of next-generation high-pulse energy lasers based on ytterbium-fiber amplifiers [52, 101]. To extract, or “dump”, the powerful circulating pulse from the cavity, a fast optical switch is used. In all experiments performed so far, acousto-optic modulators were employed for this purpose. When inserted in

---

[5] The full study is included together with a statement of author contributions in Chapter 9. A revised version of this manuscript has been published in *Nature Photonics* [123] after submission of this thesis on January 21st, 2019.

the cavity under Brewster's angle, they produce very low losses, and are capable of sufficiently fast switching times.

Many design considerations relevant to the power scalability of this concept, termed "stack-and-dump", are similar to those for cavity-enhanced HHG. In particular, these relate to optically induced damage, thermal lensing, dispersion, and nonlinear effects in intracavity media. The main limitation to the power scalability of stack-and-dump setups is posed by the nonlinear phase produced by the Kerr effect in the optical switch [101, 126]. While the application of the intracavity soliton compression scheme described in the preceding section could be an interesting prospect, the power scalability of the linear stack-and-dump scheme would benefit tremendously from an output coupling scheme avoiding transmissive elements [52].

Ultrafast optomechanical pulse picking[6]

Here we propose a scheme for moving part of the intracavity beam path by using one or more rotating mirrors. To achieve a stable beam path in the remaining cavity, one or more static mirrors are used to image the rotating mirror onto itself, or onto a second, synchronized mirror. In this fashion, the beam path on the imaging optics can be brought to move over a circle with a large circumference, while using a small rotating mirror, allowing high revolution rates. As a result, the beam path can move by a distance larger than the beam width during one pulse repetition period in the a cavity. An individual pulse from the pulse train can then be dumped by placing an output coupling element, for instance a mirror edge, at some point along the circle described by the beam path over one mirror revolution. Requiring no transmissive elements, a cavity dumper based on this concept would offer large improvements in terms of power scalability.

We proposed several possible implementations of this concept, and discuss practical parameters for its application in stack-and-dump enhancement cavities and high-pulse-energy regenerative amplifier cavities, and found that the major challenge for an experimental implementation of this concept will be posed by irregularities of the rotor motion causing cavity misalignment and synchronization issues. First measurements on a rotating mirror based on a self-bearing permanent-magnet motor [128] at rotation frequencies of up to 5 kHz, indicating that sufficient motion stability for some of the proposed implementations may be within reach of further technological development [129].

---

[6] The full study was published on January 16th, 2017 in *Applied Physics B* [127], and is included together with a statement of author contributions in Chapter 10.

Chapter 4

Conclusion

Summary

In the years preceding this thesis, the limitations of enhancement cavity technology for ultrashort high-energy pulse enhancement in general, and high-order harmonic generation in particular, have become increasingly well understood. In this thesis, several novel approaches to tackle these limitations are presented. To this end, different levers to control the roundtrip phase of enhancement cavities, in particular in the presence of thermal and nonlinear effects, have been investigated.

We have demonstrated the compensation of the *spatial* roundtrip phase distortions caused by thermal lensing through a proper choice of transmissive cavity optics, allowing control over the cavity mode evolution with increasing intracavity power. Using this scheme we have demonstrated the elimination of thermally-induced mode change in a large-mode enhancement cavity for average powers up to 160 kW.

We have optimized the *spectral* roundtrip phase by combining different appropriately designed and accurately characterized mirror coatings, allowing for the enhancement of field-stable pulses and of pulses with significantly shorter durations than achieved in previous femtosecond enhancement cavities.

We have investigated a novel approach to the operation of nonlinear femtosecond enhancement cavities, showing that by tailoring the input coupler reflectivity and spectral cavity phase, the nonlinearity-induced *temporal* phase shifts can be utilized for efficient intracavity pulse compression. This approach was investigated theoretically for the case of plasma phase shifts, and demonstrated experimentally with the generation of temporal cavity solitons for the case of an intracavity Kerr nonlinearity. In the soliton state, the self-phase modulation in a transmissive element in the enhancement cavity is compensated by the spectral phase of mirrors, and a tailored input coupler allows for a peak-power enhancement surpassing the resonant enhancement of the linear cavity by nearly an order of magnitude.

Additionally, we have proposed a scheme for the cavity dumping of energetic infrared pulses.

Outlook

Over the last decade, cavity-enhanced high-order harmonic generation has matured, recently allowing the application of coherent, multi-megahertz pulsed XUV radiation for time and frequency resolved experiments [23, 111, 130–132]. Further development of these sources depends on the optimization of phase matching between infrared and XUV fields under the constraints of passive resonant enhancement, where significant advances have been reported recently [70, 133], and the power scalability of enhancement cavities, in particular in the presence of plasma generation and XUV output couplers. The results of this thesis contribute to the understanding of limitations to this power scalability, and offer novel approaches for its extension.

Our experiments on thermal lens compensation show that the operation of high-power enhancement cavities at the edge of stability, providing large spot sizes and therefore low intensities on the optical elements, is possible even in the presence of intracavity Brewster plates, which, being robust, simple, and exhibiting extremely low losses to the cavity beam, present a well-established concept for XUV output coupling [23, 108–111]. As a result, the thermal balancing approach facilitates the power scalability of this output-coupling technique, which is typically limited by the Kerr effect in the Brewster plate [110], beyond the approximately 10 kW of average power typically used in present cavity HHG experiments [56, 60, 70, 110, 130], while allowing to maintain a power-independent mode size, and enabling compensation of astigmatism. Further development of this concept, for instance using Brewster plates with higher thermal conductivity or less absorption, and low-absorption mirror coatings [74], could offer a path to advancing the average power for picosecond enhancement cavities beyond one megawatt, which would be highly desirable for X-ray sources based on inverse Compton scattering [134–136].

Together with the carrier-envelope phase control of high-power lasers [84], the control of the optimal cavity offset frequency demonstrated here constitutes a vital step for isolated attosecond pulse generation in enhancement cavities. The advances in intracavity pulse duration, culminating in the enhancement of pulses comprising less than six optical cycles, mark the first time that temporal gating techniques [75–79] could realistically be employed in cavities [80, 81]. Together, these results provide the prerequisites for isolated attosecond pulse generation at multi-megahertz repetition rates. Moreover, the demonstrated intracavity pulse duration will benefit efforts to extend the reach of cavity enhanced HHG sources towards higher photon energies by facilitating higher clamping intensities, and may find application in cavity-enhanced frequency-comb or ultrafast spectroscopy [137, 138]. The simple approach for precise mirror phase characterization demonstrated in this context will simplify the setup of broadband enhancement cavities and may facilitate further advances in supported pulse durations.

The clamping law for intracavity plasma generation represents a valuable tool for the layout of future cavity HHG setups, which, together with phase matching considerations [133, 139], allows for an estimation of the ideal cavity finesse and enhancement for given laser pulse parameters. It has already been employed for the next generation of multi-megahertz HHG sources developed in our group [70, 140], facilitating space-charge-free photo-electron spectroscopy with an unprecedented photoelectron flux, and photon energies up to 60 eV [140]. Currently, this system is being employed for laser-dressed attosecond photoelectron spectroscopy in solids, using the RABBIT technique [141–144].

The locking scheme demonstrated here for cavity soliton generation will also benefit cavity HHG setups by avoiding the servo dynamics caused by nonlinear phase shifts which can affect the conventional locking concept [56, 64, 71]. This will reduce phase and amplitude noise of the generated XUV and may allow tuning further along the upper branch of the bistable nonlinear cavity resonance [71], resulting in improved conversion efficiencies.

Apart from presenting approaches to extend the power scalability of the standard approach of cavity-enhanced high harmonic generation, this thesis offers a first glimpse at an intriguing, novel regime of nonlinear enhancement cavity operation characterized by efficient intracavity pulse compression. While these demonstrations do not yet answer the question of whether this can be harnessed to benefit cavity enhanced high-harmonic generation, the peak power enhancement, tolerance of spectral phase deviations and nonlinear shifts, and the noise filtering properties associated with this regime mark it as a high-value target for further investigations. Its potential for cavity HHG could be unlocked either by (I) including a gas target in a high-power soliton cavity employing a separate Kerr nonlinearity for intracavity pulse compression generation, or by (II) optimizing a cavity for pulse compression through the plasma nonlinearity itself.

The viability of approach (I) depends on the interaction between soliton and plasma nonlinearity in the cavity, which, in a first step, can be studied numerically. An experimental realization would require a solution to the thermal problems limiting the power scalability in our proof-of-principle cavity soliton experiment, which will likely include the use of high-thermal-conductivity substrates, an optimization of the dispersive and tailored-reflectivity mirrors for low absorption, and the thermal-lens balancing approach demonstrated earlier. Assuming that the cavity soliton robustness to roundtrip phase distortions scales similarly to linear enhancement cavities, it should be advantageous to implement a soliton cavity with a far lower peak-power enhancement than demonstrated here for cavity HHG experiments. The Brewster plate producing the Kerr effect could be used simultaneously for XUV output coupling. Alternatively, soliton generation could rely on the Kerr nonlinearity in the gas target itself. This scheme for cavity-soliton driven high-harmonic generation would be conceptually similar to HHG in mode-locked laser oscillators [145], but would offer greater control of the soliton state, and potentially higher intracavity power and shorter pulse durations. It is important to note that the presented cavity soliton study constitutes a first proof-of-principle experiment, and leaves room for further optimization. Such efforts will benefit from the approaches for control of thermal lensing and the spectral roundtrip phase of cavities presented earlier in this thesis.

Important next steps on the path to realizing approach (II) would include numerically exploring stable steady states for realistic cavity mirror designs and driving pulses, and investigating whether they can be experimentally accessed using a locking scheme similar to the one employed for Kerr soliton generation.

Bibliography

[1] J. M. Vaughan, *The Fabry-Perot interferometer: History, theory, practice, and applications*, The Adam Hilger series on optics and optoelectronics (Adam Hilger, Bristol, PA, 1989).

[2] T. H. Maiman, "Stimulated optical radiation in ruby," Nature **187**, 493–494 (1960).

[3] A. E. Siegman, "Laser beams and resonators: the 1960s," IEEE Journal of selected topics in quantum electronics **6**, 1380–1388 (2000).

[4] A. L. Schawlow and C. H. Townes, "Infrared and optical masers," Physical Review **112**, 1940–1949 (1958).

[5] A. M. Prokhorov, "Molecular amplifier and generator for submillimeter wave," Sov. Phys. JETP **7**, 1140–1141 (1958).

[6] A. G. Fox and T. Li, "Resonant modes in a maser interferometer," Bell System Technical Journal **40**, 453–488 (1961).

[7] G. D. Boyd and J. P. Gordon, "Confocal multimode resonator for millimeter through optical wavelength masers," Bell System Technical Journal **40**, 489–508 (1961).

[8] G. D. Boyd and H. Kogelnik, "Generalized confocal resonator theory," Bell System Technical Journal **41**, 1347–1369 (1962).

[9] H. Walther, B. T. H. Varcoe, B.-G. Englert, and T. Becker, "Cavity quantum electrodynamics," Reports on Progress in Physics **69**, 1325–1382 (2006).

[10] Firth and Scroggie, "Optical bullet holes: Robust controllable localized states of a nonlinear cavity," Physical review letters **76**, 1623–1626 (1996).

[11] S. Barland, J. R. Tredicce, M. Brambilla, L. A. Lugiato, S. Balle, M. Giudici, T. Maggipinto, L. Spinelli, G. Tissoni, T. Knödl, M. Miller, and R. Jäger, "Cavity solitons as pixels in semiconductor microcavities," Nature **419**, 699–702 (2002).

[12] The LIGO Scientific Collaboration, "Advanced ligo," Classical and Quantum Gravity **32**, 074001 (2015).

[13] LIGO Scientific Collaboration and Virgo Collaboration, "Observation of gravitational waves from a binary black hole merger," Physical review letters **116**, 061102 (2016).

[14] A. Ashkin, G. Boyd, and J. Dziedzic, "Resonant optical second harmonic generation and mixing," IEEE Journal of Quantum Electronics **2**, 109–124 (1966).

[15] E. S. Polzik and H. J. Kimble, "Frequency doubling with knbo_3 in an external cavity," Optics letters **16**, 1400 (1991).

[16] A. E. Siegman, *Lasers* (University Science Books, Mill Valley, Calif., 1986).

[17] H. A. Haus, "Mode-locking of lasers," IEEE Journal of Selected Topics in Quantum Electronics **6**, 1173–1185 (2000).

[18] D. J. Jones, S. A. Diddams, J. K. Ranka, A. Stentz, R. S. Windeler, J. L. Hall, and S. T. Cundiff, "Carrier-envelope phase control of femtosecond mode-locked lasers and direct optical frequency synthesis," Science **288**, 635–639 (2000).

[19] T. Udem, R. Holzwarth, and T. W. Hänsch, "Optical frequency metrology," Nature **416**, 233–237 (2002).

[20] G. Steinmeyer, D. H. Sutter, L. Gallmann, and U. Keller, "Frontiers in ultrashort pulse generation: Pushing the limits in linear and nonlinear optics," Science **286**, 1507–1512 (1999).

[21] T. Brabec and F. Krausz, "Intense few-cycle laser fields: Frontiers of nonlinear optics," Reviews of Modern Physics **72**, 545–591 (2000).

[22] D. C. Yost, T. R. Schibli, J. Ye, J. L. Tate, J. Hostetter, M. B. Gaarde, and K. J. Schafer, "Vacuum-ultraviolet frequency combs from below-threshold harmonics," Nature Physics **5**, 815–820 (2009).

[23] C. Benko, T. K. Allison, A. Cingöz, L. Hua, F. Labaye, D. C. Yost, and J. Ye, "Extreme ultraviolet radiation with coherence time greater than 1 s," Nature Photonics **8**, 530–536 (2014).

[24] M. Hentschel, R. Kienberger, C. Spielmann, G. A. Reider, N. Milosevic, T. Brabec, P. Corkum, U. Heinzmann, M. Drescher, and F. Krausz, "Attosecond metrology," Nature **414**, 509–513 (2001).

[25] E. Goulielmakis, M. Schultze, M. Hofstetter, V. S. Yakovlev, J. Gagnon, M. Uiberacker, A. L. Aquila, E. M. Gullikson, D. T. Attwood, R. Kienberger, F. Krausz, and U. Kleineberg, "Single-cycle nonlinear optics," Science (New York, N.Y.) **320**, 1614–1617 (2008).

[26] F. Krausz and M. I. Stockman, "Attosecond metrology: from electron capture to future signal processing," Nature Photonics **8**, 205–213 (2014).

[27] A. Giesen and J. Speiser, "Fifteen years of work on thin-disk lasers: Results and scaling laws," IEEE Journal of Selected Topics in Quantum Electronics **13**, 598–609 (2007).

[28] T. Metzger, A. Schwarz, C. Y. Teisset, D. Sutter, A. Killi, R. Kienberger, and F. Krausz, "High-repetition-rate picosecond pump laser based on a yb:yag disk amplifier for optical parametric amplification," Optics letters **34**, 2123–2125 (2009).

[29] P. Russbueldt, T. Mans, J. Weitenberg, H. D. Hoffmann, and R. Poprawe, "Compact diode-pumped 1.1 kw yb:yag innoslab femtosecond amplifier," Optics letters **35**, 4169–4171 (2010).

[30] T. Eidam, S. Hanf, E. Seise, T. V. Andersen, T. Gabler, C. Wirth, T. Schreiber, J. Limpert, and A. Tünnermann, "Femtosecond fiber cpa system emitting 830 w average output power," Optics letters **35**, 94–96 (2010).

[31] C. Jauregui, J. Limpert, and A. Tünnermann, "High-power fibre lasers," Nature Photonics **7**, 861–867 (2013).

[32] G. Mourou, B. Brocklesby, T. Tajima, and J. Limpert, "The future is fibre accelerators," Nature Photonics **7**, 258–261 (2013).

[33] H. Fattahi, H. G. Barros, M. Gorjan, T. Nubbemeyer, B. Alsaif, C. Y. Teisset, M. Schultze, S. Prinz, M. Haefner, M. Ueffing, A. Alismail, L. Vámos, A. Schwarz, O. Pronin, J. Brons, X. T. Geng, G. Arisholm, M. Ciappina, V. S. Yakovlev, D.-E. Kim, A. M. Azzeer, N. Karpowicz, D. Sutter, Z. Major, T. Metzger, and F. Krausz, "Third-generation femtosecond technology," Optica **1**, 45 (2014).

[34] A. Vernaleken, J. Weitenberg, T. Sartorius, P. Russbueldt, W. Schneider, S. L. Stebbings, M. F. Kling, P. Hommelhoff, H.-D. Hoffmann, R. Poprawe, F. Krausz, T. W. Hänsch, and T. Udem, "Single-pass high-harmonic generation at 20.8 mhz repetition rate," Optics letters **36**, 3428–3430 (2011).

[35] C. M. Heyl, J. Güdde, A. L'Huillier, and U. Höfer, "High-order harmonic generation with mj laser pulses at high repetition rates," Journal of Physics B: Atomic, Molecular and Optical Physics **45**, 074020 (2012).

[36] M. Krebs, S. Hädrich, S. Demmler, J. Rothhardt, A. Zaïr, L. Chipperfield, J. Limpert, and A. Tünnermann, "Towards isolated attosecond pulses at megahertz repetition rates," Nature Photonics **7**, 555–559 (2013).

[37] S. Hädrich, A. Klenke, J. Rothhardt, M. Krebs, A. Hoffmann, O. Pronin, V. Pervak, J. Limpert, and A. Tünnermann, "High photon flux table-top coherent extreme-ultraviolet source," Nature Photonics **8**, 779–783 (2014).

[38] S. Hädrich, M. Krebs, A. Hoffmann, A. Klenke, J. Rothhardt, J. Limpert, and A. Tünnermann, "Exploring new avenues in high repetition rate table-top coherent extreme ultraviolet sources," Light: Science & Applications **4**, e320–e320 (2015).

[39] F. Emaury, A. Diebold, C. J. Saraceno, and U. Keller, "Compact extreme ultraviolet source at megahertz pulse repetition rate with a low-noise ultrafast thin-disk laser oscillator," Optica **2**, 980 (2015).

[40] C. M. Heyl, C. L. Arnold, A. Couairon, and A. L'Huillier, "Introduction to macroscopic power scaling principles for high-order harmonic generation," Journal of Physics B: Atomic, Molecular and Optical Physics **50**, 013001 (2017).

[41] A. L. Cavalieri, N. Müller, T. Uphues, V. S. Yakovlev, A. Baltuska, B. Horvath, B. Schmidt, L. Blümel, R. Holzwarth, S. Hendel, M. Drescher, U. Kleineberg, P. M. Echenique, R. Kienberger, F. Krausz, and U. Heinzmann, "Attosecond spectroscopy in condensed matter," Nature **449**, 1029–1032 (2007).

[42] S. H. Chew, F. Süßmann, C. Späth, A. Wirth, J. Schmidt, S. Zherebtsov, A. Guggenmos, A. Oelsner, N. Weber, J. Kapaldo, A. Gliserin, M. I. Stockman, M. F. Kling, and U. Kleineberg, "Time-of-flight-photoelectron emission microscopy on plasmonic structures using attosecond extreme ultraviolet pulses," Applied Physics Letters **100**, 051904 (2012).

[43] S. Mathias, M. Bauer, M. Aeschlimann, L. Miaja-Avila, H. C. Kapteyn, and M. M. Murnane, "Time-resolved photoelectron spectroscopy at surfaces using femtosecond xuv pulses," in "Dynamics at Solid State Surfaces and Interfaces," , vol. 13, U. Bovensiepen, H. Petek, and M. Wolf, eds. (Wiley-VCH Verlag GmbH & Co. KGaA, Weinheim, Germany, 2010), pp. 499–535.

[44] M. Herrmann, M. Haas, U. D. Jentschura, F. Kottmann, D. Leibfried, G. Saathoff, C. Gohle, A. Ozawa, V. Batteiger, S. Knünz, N. Kolachevsky, H. A. Schüssler, T. W. Hänsch, and T. Udem, "Feasibility of coherent xuv spectroscopy on the 1s–2s transition in singly ionized helium," Physical Review A **79**, 60 (2009).

[45] E. E. Eyler, D. E. Chieda, M. C. Stowe, M. J. Thorpe, T. R. Schibli, and J. Ye, "Prospects for precision measurements of atomic helium using direct frequency comb spectroscopy," The European Physical Journal D **48**, 43–55 (2008).

[46] D. Z. Kandula, C. Gohle, T. J. Pinkert, W. Ubachs, and K. S. E. Eikema, "Extreme ultraviolet frequency comb metrology," Physical review letters **105**, 063001 (2010).

[47] L. von der Wense, B. Seiferle, M. Laatiaoui, J. B. Neumayr, H.-J. Maier, H.-F. Wirth, C. Mokry, J. Runke, K. Eberhardt, C. E. Düllmann, N. G. Trautmann, and P. G. Thirolf, "Direct detection of the (229)th nuclear clock transition," Nature **533**, 47–51 (2016).

[48] L. von der Wense, B. Seiferle, and P. G. Thirolf, "Towards a 229th-based nuclear clock," Meas Tech **458**, 563 (2018).

[49] R. Jones, K. Moll, M. Thorpe, and J. Ye, "Phase-coherent frequency combs in the vacuum ultraviolet via high-harmonic generation inside a femtosecond enhancement cavity," Physical Review Letters **94** (2005).

[50] C. Gohle, T. Udem, M. Herrmann, J. Rauschenberger, R. Holzwarth, H. A. Schuessler, F. Krausz, and T. W. Hänsch, "A frequency comb in the extreme ultraviolet," Nature **436**, 234–237 (2005).

[51] R. J. Jones and J. Ye, "Femtosecond pulse amplification by coherent addition in a passive optical cavity," Optics Letters **27**, 1848 (2002).

[52] S. Breitkopf, T. Eidam, A. Klenke, L. von Grafenstein, H. Carstens, S. Holzberger, E. Fill, T. Schreiber, F. Krausz, A. Tünnermann, I. Pupeza, and J. Limpert, "A concept for multiterawatt fibre lasers based on coherent pulse stacking in passive cavities," Light: Science & Applications **3**, e211 (2014).

[53] O. Pronin, V. Pervak, E. Fill, J. Rauschenberger, F. Krausz, and A. Apolonski, "Ultrabroadband efficient intracavity xuv output coupler," Optics express **19**, 10232–10240 (2011).

[54] I. Pupeza, E. E. Fill, and F. Krausz, “Low-loss vis/ir-xuv beam splitter for high-power applications,” Optics express **19**, 12108–12118 (2011).

[55] D. C. Yost, T. R. Schibli, and J. Ye, “Efficient output coupling of intracavity high-harmonic generation,” Optics Letters **33**, 1099 (2008).

[56] D. C. Yost, A. Cingöz, T. K. Allison, A. Ruehl, M. E. Fermann, I. Hartl, and J. Ye, “Power optimization of xuv frequency combs for spectroscopy applications,” Optics Express **19**, 23483–23493 (2011).

[57] K. D. Moll, R. J. Jones, and J. Ye, “Output coupling methods for cavity-based high-harmonic generation,” Optics Express **14**, 8189 (2006).

[58] A. Ozawa, J. Rauschenberger, C. Gohle, M. Herrmann, D. R. Walker, V. Pervak, A. Fernandez, R. Graf, A. Apolonski, R. Holzwarth, F. Krausz, T. W. Hänsch, and T. Udem, “High harmonic frequency combs for high resolution spectroscopy,” Physical Review Letters **100**, 253901 (2008).

[59] J. Weitenberg, P. Russbüldt, T. Eidam, and I. Pupeza, “Transverse mode tailoring in a quasi-imaging high-finesse femtosecond enhancement cavity,” Optics express **19**, 9551–9561 (2011).

[60] I. Pupeza, S. Holzberger, T. Eidam, H. Carstens, D. Esser, J. Weitenberg, P. Rußbüldt, J. Rauschenberger, J. Limpert, T. Udem, A. Tünnermann, T. W. Hänsch, A. Apolonski, F. Krausz, and E. Fill, “Compact high-repetition-rate source of coherent 100 ev radiation,” Nature Photonics **7**, 608–612 (2013).

[61] I. Pupeza, M. Högner, J. Weitenberg, S. Holzberger, D. Esser, T. Eidam, J. Limpert, A. Tünnermann, E. Fill, and V. S. Yakovlev, “Cavity-enhanced high-harmonic generation with spatially tailored driving fields,” Physical review letters **112**, 103902 (2014).

[62] M. J. Thorpe, R. J. Jones, K. D. Moll, J. Ye, and R. Lalezari, “Precise measurements of optical cavity dispersion and mirror coating properties via femtosecond combs,” Optics express **13**, 882 (2005).

[63] K. D. Moll, R. J. Jones, and J. Ye, “Nonlinear dynamics inside femtosecond enhancement cavities,” Optics Express **13**, 1672 (2005).

[64] T. K. Allison, A. Cingöz, D. C. Yost, and J. Ye, “Extreme nonlinear optics in a femtosecond enhancement cavity,” Physical review letters **107**, 183903 (2011).

[65] D. R. Carlson, J. Lee, J. Mongelli, E. M. Wright, and R. J. Jones, “Intracavity ionization and pulse formation in femtosecond enhancement cavities,” Optics letters **36**, 2991–2993 (2011).

[66] J. Lee, D. R. Carlson, and R. J. Jones, “Optimizing intracavity high harmonic generation for xuv fs frequency combs,” Optics Express **19**, 23315–23326 (2011).

[67] T. Eidam, F. Röser, O. Schmidt, J. Limpert, and A. Tünnermann, “57 w, 27 fs pulses from a fiber laser system using nonlinear compression,” Applied Physics B **92**, 9–12 (2008).

[68] A. Ruehl, A. Marcinkevicius, M. E. Fermann, and I. Hartl, "80 w, 120 fs yb-fiber frequency comb," Optics letters **35**, 3015–3017 (2010).

[69] C. Jocher, T. Eidam, S. Hädrich, J. Limpert, and A. Tünnermann, "Sub 25 fs pulses from solid-core nonlinear compression stage at 250 w of average power," Optics letters **37**, 4407–4409 (2012).

[70] H. Carstens, M. Högner, T. Saule, S. Holzberger, N. Lilienfein, A. Guggenmos, C. Jocher, T. Eidam, D. Esser, V. Tosa, V. Pervak, J. Limpert, A. Tünnermann, U. Kleineberg, F. Krausz, and I. Pupeza, "High-harmonic generation at 250 mhz with photon energies exceeding 100 ev," Optica **3**, 366 (2016).

[71] A. K. Mills, T. J. Hammond, M. H. C. Lam, and D. J. Jones, "Xuv frequency combs via femtosecond enhancement cavities," Journal of Physics B: Atomic, Molecular and Optical Physics **45**, 142001 (2012).

[72] I. Pupeza, T. Eidam, J. Rauschenberger, B. Bernhardt, A. Ozawa, E. Fill, A. Apolonski, T. Udem, J. Limpert, Z. A. Alahmed, A. M. Azzeer, A. Tünnermann, T. W. Hänsch, and F. Krausz, "Power scaling of a high-repetition-rate enhancement cavity," Optics letters **35**, 2052–2054 (2010).

[73] H. Carstens, S. Holzberger, J. Kaster, J. Weitenberg, V. Pervak, A. Apolonski, E. Fill, F. Krausz, and I. Pupeza, "Large-mode enhancement cavities," Optics express **21**, 11606–11617 (2013).

[74] H. Carstens, N. Lilienfein, S. Holzberger, C. Jocher, T. Eidam, J. Limpert, A. Tünnermann, J. Weitenberg, D. C. Yost, A. Alghamdi, Z. Alahmed, A. Azzeer, A. Apolonski, E. Fill, F. Krausz, and I. Pupeza, "Megawatt-scale average-power ultrashort pulses in an enhancement cavity," Optics letters **39**, 2595–2598 (2014).

[75] P. Antoine, A. L'Huillier, M. Lewenstein, P. Salières, and B. Carré, "Theory of high-order harmonic generation by an elliptically polarized laser field," Physical Review A **53**, 1725–1745 (1996).

[76] O. Tcherbakoff, E. Mével, D. Descamps, J. Plumridge, and E. Constant, "Time-gated high-order harmonic generation," Physical Review A **68**, 447 (2003).

[77] G. Kolliopoulos, P. A. Carpeggiani, D. Rompotis, D. Charalambidis, and P. Tzallas, "A compact collinear polarization gating scheme for many cycle laser pulses," The Review of scientific instruments **83**, 063102 (2012).

[78] C. M. Heyl, S. N. Bengtsson, S. Carlström, J. Mauritsson, C. L. Arnold, and A. LHuillier, "Noncollinear optical gating," New Journal of Physics **16**, 052001 (2014).

[79] M. Louisy, C. L. Arnold, M. Miranda, E. W. Larsen, S. N. Bengtsson, D. Kroon, M. Kotur, D. Guénot, L. Rading, P. Rudawski, F. Brizuela, F. Campi, B. Kim, A. Jarnac, A. Houard, J. Mauritsson, P. Johnsson, A. L'Huillier, and C. M. Heyl, "Gating attosecond pulses in a noncollinear geometry," Optica **2**, 563 (2015).

[80] M. Högner, V. Tosa, and I. Pupeza, “Generation of isolated attosecond pulses with enhancement cavities—a theoretical study,” New Journal of Physics **19**, 033040 (2017).

[81] M. Högner, T. Saule, N. Lilienfein, V. Pervak, and I. Pupeza, “Tailoring the transverse mode of a high-finesse optical resonator with stepped mirrors,” Journal of Optics **20**, 024003 (2018).

[82] A. de Bohan, P. Antoine, D. B. Milošević, and B. Piraux, “Phase-dependent harmonic emission with ultrashort laser pulses,” Physical review letters **81**, 1837–1840 (1998).

[83] O. Pronin, M. Seidel, F. Lücking, J. Brons, E. Fedulova, M. Trubetskov, V. Pervak, A. Apolonski, T. Udem, and F. Krausz, “High-power multi-megahertz source of waveform-stabilized few-cycle light,” Nature communications **6**, 6988 (2015).

[84] T. Saule, S. Holzberger, O. de Vries, M. Plötner, J. Limpert, A. Tünnermann, and I. Pupeza, “Phase-stable, multi-µj femtosecond pulses from a repetition-rate tunable ti:sa-oscillator-seeded yb-fiber amplifier,” Applied Physics B **123**, 6877 (2017).

[85] W. G. Nagourney, *Quantum electronics for atomic physics*, Oxford graduate texts (Oxford University Press, Oxford and New York, 2010).

[86] G. Winkler, J. Fellinger, J. Seres, E. Seres, and T. Schumm, “Non-planar femtosecond enhancement cavity for vuv frequency comb applications,” Optics Express **24**, 5253–5262 (2016).

[87] W. B. Joyce and B. C. DeLoach, “Alignment of gaussian beams,” Applied optics **23**, 4187 (1984).

[88] R. Hauck, H. P. Kortz, and H. Weber, “Misalignment sensitivity of optical resonators,” Applied optics **19**, 598–601 (1980).

[89] A. M. Weiner, *Ultrafast optics*, Wiley series in pure and applied optics (Wiley, Hoboken, 2009).

[90] R. Jason Jones, I. Thomann, and J. Ye, “Precision stabilization of femtosecond lasers to high-finesse optical cavities,” Optics Letters **69**, 1286 (2004).

[91] R. W. P. Drever, J. L. Hall, F. V. Kowalski, J. Hough, G. M. Ford, A. J. Munley, and H. Ward, “Laser phase and frequency stabilization using an optical resonator,” Applied Physics B **31**, 97–105 (1983).

[92] E. D. Black, “An introduction to pound–drever–hall laser frequency stabilization,” American Journal of Physics **69**, 79–87 (2001).

[93] S. A. Furman and A. V. Tikhonravov, *Basics of optics of multilayer systems* (Frontieres, Gif-sur-Yvette, 1992).

[94] M. Mero, J. Liu, W. Rudolph, D. Ristau, and K. Starke, “Scaling laws of femtosecond laser pulse induced breakdown in oxide films,” Optics Communications **71**, S373 (2005).

[95] I. B. Angelov, M. von Pechmann, M. K. Trubetskov, F. Krausz, and V. Pervak, “Optical breakdown of multilayer thin-films induced by ultrashort pulses at mhz repetition rates,” Optics Express **21**, 31453–31461 (2013).

[96] H. Carstens, *Enhancement Cavities for the Generation of Extreme Ultraviolet and Hard X-Ray Radiation*, Springer Theses, Recognizing Outstanding Ph.D. Research (Springer International Publishing, Cham, 2018).

[97] W. Winkler, K. Danzmann, A. Rüdiger, and R. Schilling, “Heating by optical absorption and the performance of interferometric gravitational-wave detectors,” Physical Review A **44**, 7022–7036 (1991).

[98] N. Lilienfein, “Investigation of thermal lensing in high-power enhancement-cavities,” Master’s thesis, Ludwig-Maximilians-University, Munich (2013).

[99] R. W. Boyd, *Nonlinear optics* (Elsevier, Acad. Press, Amsterdam [u.a.], 2008), 3rd ed.

[100] S. Holzberger, “Enhancement cavities for attosecond physics,” Ph.d. thesis, Ludwig–Maximilians–University, Munich (2015).

[101] S. Breitkopf, S. Wunderlich, T. Eidam, E. Shestaev, S. Holzberger, T. Gottschall, H. Carstens, A. Tünnermann, I. Pupeza, and J. Limpert, “Extraction of enhanced, ultrashort laser pulses from a passive 10-mhz stack-and-dump cavity,” Applied Physics B **122**, 267 (2016).

[102] C. J. Joachain, N. J. Kylstra, and R. M. Potvliege, *Atoms in Intense Laser Fields* (Cambridge University Press, Cambridge, 2011).

[103] A. M. Perelomov and Popov, V. S. and Terent’ev, M. V., “Ionization of atoms in an alternating electric field,” Sov. Phys. JETP **23**, 924–934 (1966).

[104] G. P. Agrawal, *Nonlinear fiber optics, fifth edition* (Academic Press, Kidlington, Oxford, U.K. and Waltham, Mass., 2013), 5th ed.

[105] P. Grelu and N. Akhmediev, “Dissipative solitons for mode-locked lasers,” Nature Photonics **6**, 84–92 (2012).

[106] T. Herr, V. Brasch, J. D. Jost, C. Y. Wang, N. M. Kondratiev, M. L. Gorodetsky, and T. J. Kippenberg, “Temporal solitons in optical microresonators,” Nature Photonics **8**, 145–152 (2014).

[107] F. Leo, S. Coen, P. Kockaert, S.-P. Gorza, P. Emplit, and M. Haelterman, “Temporal cavity solitons in one-dimensional kerr media as bits in an all-optical buffer,” Nature Photonics **4**, 471–476 (2010).

[108] C. Benko, L. Hua, T. K. Allison, F. Labaye, and J. Ye, “Cavity-enhanced field-free molecular alignment at a high repetition rate,” Physical review letters **114**, 153001 (2015).

[109] A. Ozawa, Z. Zhao, M. Kuwata-Gonokami, and Y. Kobayashi, “High average power coherent vuv generation at 10 mhz repetition frequency by intracavity high harmonic generation,” Optics Express **23**, 15107–15118 (2015).

[110] C. Corder, P. Zhao, X. Li, M. D. Kershis, M. G. White, and T. K. Allison, "Development of a tunable high repetition rate xuv source for time-resolved photoemission studies of ultrafast dynamics at surfaces," Proc. SPIE 10519, Laser Applications in Microelectronic and Optoelectronic Manufacturing (LAMOM) XXIII p. 105190B (16 February 2018).

[111] C. Corder, P. Zhao, J. Bakalis, X. Li, M. D. Kershis, A. R. Muraca, M. G. White, and T. K. Allison, "Ultrafast extreme ultraviolet photoemission without space charge," Structural Dynamics **5**, 054301 (2018).

[112] N. Lilienfein, H. Carstens, S. Holzberger, C. Jocher, T. Eidam, J. Limpert, A. Tünnermann, A. Apolonski, F. Krausz, and I. Pupeza, "Balancing of thermal lenses in enhancement cavities with transmissive elements," Optics letters **40**, 843–846 (2015).

[113] S. Holzberger, N. Lilienfein, M. Trubetskov, H. Carstens, F. Lucking, V. Pervak, F. Krausz, and I. Pupeza, "Enhancement cavities for zero-offset-frequency pulse trains," Optics letters **40**, 2165–2168 (2015).

[114] I. Pupeza, X. Gu, E. Fill, T. Eidam, J. Limpert, A. Tünnermann, F. Krausz, and T. Udem, "Highly sensitive dispersion measurement of a high-power passive optical resonator using spatial-spectral interferometry," Optics Express **18**, 26184 (2010).

[115] S. Holzberger, N. Lilienfein, H. Carstens, T. Saule, M. Hogner, F. Lucking, M. Trubetskov, V. Pervak, T. Eidam, J. Limpert, A. Tunnermann, E. Fill, F. Krausz, and I. Pupeza, "Femtosecond enhancement cavities in the nonlinear regime," Physical review letters **115**, 023902 (2015).

[116] N. Lilienfein, C. Hofer, S. Holzberger, C. Matzer, P. Zimmermann, M. Trubetskov, V. Pervak, and I. Pupeza, "Enhancement cavities for few-cycle pulses," Optics letters **42**, 271–274 (2017).

[117] V. L. Kalashnikov, "Femtosecond pulse enhancement in an external resonator: impact of dispersive and nonlinear effects," Applied Physics B **92**, 19–23 (2008).

[118] A. Schreiber, B. Thüring, M. Kreuzer, and T. Tschudi, "Experimental investigation of solitary structures in a nonlinear optical feedback system," Optics Communications **136**, 415–418 (1997).

[119] K. Saha, Y. Okawachi, B. Shim, J. S. Levy, R. Salem, A. R. Johnson, M. A. Foster, M. R. E. Lamont, M. Lipson, and A. L. Gaeta, "Modelocking and femtosecond pulse generation in chip-based frequency combs," Optics express **21**, 1335–1343 (2013).

[120] A. Pasquazi, M. Peccianti, L. Razzari, D. J. Moss, S. Coen, M. Erkintalo, Y. K. Chembo, T. Hansson, S. Wabnitz, P. Del'Haye, X. Xue, A. M. Weiner, and R. Morandotti, "Microcombs: A novel generation of optical sources," Physics Reports **729**, 1–81 (2018).

[121] E. Obrzud, S. Lecomte, and T. Herr, "Temporal solitons in microresonators driven by optical pulses," Nature Photonics **11**, 600–607 (2017).

[122] M. Malinowski, A. Rao, P. Delfyett, and S. Fathpour, "Optical frequency comb generation by pulsed pumping," APL Photonics **2**, 066101 (2017).

[123] N. Lilienfein, C. Hofer, M. Högner, T. Saule, M. Trubetskov, V. Pervak, E. Fill, C. Riek, A. Leitenstorfer, J. Limpert, F. Krausz, and I. Pupeza, "Temporal solitons in free-space femtosecond enhancement cavities," Nature Photonics, advance online publication, DOI:10.1038/s41566-018-0341-y (2019) .

[124] T. Heupel, M. Weitz, and T. W. Hänsch, "Phase-coherent light pulses for atom optics and interferometry," Optics Letters **22**, 1719 (1997).

[125] Y. Vidne, M. Rosenbluh, and T. W. Hansch, "Pulse picking by phase-coherent additive pulse generation in an external cavity," Optics Letters **28**, 2396 (2003).

[126] R. J. Jones and J. Ye, "High-repetition-rate coherent femtosecond pulse amplification with an external passive optical cavity," Optics Letters **29**, 2812 (2004).

[127] N. Lilienfein, S. Holzberger, and I. Pupeza, "Ultrafast optomechanical pulse picking," Applied Physics B **123**, 1916 (2017).

[128] T. Baumgartner, R. M. Burkart, and J. W. Kolar, "Analysis and design of a 300-w 500000-r/min slotless self-bearing permanent-magnet motor," IEEE Transactions on Industrial Electronics **61**, 4326–4336 (2014).

[129] S. Breitkopf, N. Lilienfein, T. Achtnich, C. Zwyssig, A. Tünnermann, I. Pupeza, and J. Limpert, "Velocity- and pointing-error measurements of a 300 000-r/min self-bearing permanent-magnet motor for optical applications," The Review of scientific instruments **89**, 063110 (2018).

[130] A. Cingoz, D. C. Yost, T. K. Allison, A. Ruehl, M. E. Fermann, I. Hartl, and J. Ye, "Direct frequency comb spectroscopy in the extreme ultraviolet," Nature **482**, 68–71 (2012).

[131] A. Ozawa and Y. Kobayashi, "vuv frequency-comb spectroscopy of atomic xenon," Physical Review A **87** (2013).

[132] A. K. Mills, S. Zhdanovich, A. Sheyerman, G. Levy, A. Damascelli, and D. J. Jones, "An xuv source using a femtosecond enhancement cavity for photoemission spectroscopy," (SPIE, 2015), SPIE Proceedings, p. 95121I.

[133] G. Porat, C. M. Heyl, S. B. Schoun, C. Benko, N. Dörre, K. L. Corwin, and J. Ye, "Phase-matched extreme-ultraviolet frequency-comb generation," Nature Photonics **12**, 387–391 (2018).

[134] Z. Huang and R. Ruth, "Laser-electron storage ring," Physical Review Letters **80**, 976–979 (1998).

[135] W. S. Graves, W. Brown, F. X. Kaertner, and D. E. Moncton, "Mit inverse compton source concept," Nuclear Instruments and Methods in Physics Research Section A: Accelerators, Spectrometers, Detectors and Associated Equipment **608**, S103–S105 (2009).

[136] J. Bonis, R. Chiche, R. Cizeron, M. Cohen, E. Cormier, P. Cornebise, N. Delerue, R. Flaminio, D. Jehanno, F. Labaye, M. Lacroix, R. Marie, B. Mercier, C. Michel, Y. Peinaud, L. Pinard, C. Prevost, V. Soskov, A. Variola, and F. Zomer, "Non-planar four-mirror optical cavity for high intensity gamma ray flux production by pulsed laser beam compton scattering off gev-electrons," Journal of Instrumentation **7**, P01017 (2012).

[137] F. Adler, M. J. Thorpe, K. C. Cossel, and J. Ye, "Cavity-enhanced direct frequency comb spectroscopy: Technology and applications," Annual Review of Analytical Chemistry **3**, 175–205 (2010).

[138] M. A. R. Reber, Y. Chen, and T. K. Allison, "Cavity-enhanced ultrafast spectroscopy: Ultrafast meets ultrasensitive," Optica **3**, 311 (2016).

[139] E. Constant, D. Garzella, P. Breger, E. Mével, C. Dorrer, C. Le Blanc, F. Salin, and P. Agostini, "Optimizing high harmonic generation in absorbing gases: Model and experiment," Physical review letters **82**, 1668–1671 (1999).

[140] T. Saule, S. Heinrich, J. Schötz, N. Lilienfein, M. Högner, O. DeVries, M. Ploetner, J. Weitenberg, D. Esser, J. Schulte, P. Russbueldt, J. Limpert, M. F. Kling, U. Kleineberg, and I. Pupeza, "High-flux, high-photon-energy ultrafast extreme-ultraviolet photoemission spectroscopy at 18.4 mhz pulse repetition rate," (in press, DOI:10.1038/s41467-019-08367-y (2019)).

[141] H. G. Muller, "Reconstruction of attosecond harmonic beating by interference of two-photon transitions," Applied Physics B **74**, s17–s21 (2002).

[142] K. Klünder, J. M. Dahlström, M. Gisselbrecht, T. Fordell, M. Swoboda, D. Guénot, P. Johnsson, J. Caillat, J. Mauritsson, A. Maquet, R. Taïeb, and A. L'Huillier, "Probing single-photon ionization on the attosecond time scale," Physical review letters **106**, 143002 (2011).

[143] R. Locher, L. Castiglioni, M. Lucchini, M. Greif, L. Gallmann, J. Osterwalder, M. Hengsberger, and U. Keller, "Energy-dependent photoemission delays from noble metal surfaces by attosecond interferometry," Optica **2**, 405 (2015).

[144] Z. Tao, C. Chen, T. Szilvási, M. Keller, M. Mavrikakis, H. Kapteyn, and M. Murnane, "Direct time-domain observation of attosecond final-state lifetimes in photoemission from solids," Science (New York, N.Y.) **353**, 62–67 (2016).

[145] F. Labaye, M. Gaponenko, V. J. Wittwer, A. Diebold, C. Paradis, N. Modsching, L. Merceron, F. Emaury, I. J. Graumann, C. R. Phillips, C. J. Saraceno, C. Kränkel, U. Keller, and T. Südmeyer, "Extreme ultraviolet light source at a megahertz repetition rate based on high-harmonic generation inside a mode-locked thin-disk laser oscillator," Optics letters **42**, 5170–5173 (2017).

Part II

Results

Chapter 5

Balancing of thermal lenses in enhancement cavities with transmissive elements

by

Nikolai Lilienfein, Henning Carstens, Simon Holzberger, Christoph Jocher,
Tino Eidam, Jens Limpert, Andreas Tünnermann, Alexander Apolonski,
Ferenc Krausz and Ioachim Pupeza

published in

Optics Letters (2015)
DOI: 10.1364/OL.40.000843

Contributions

I conceived the experiment together with H.C. and I.P., and performed the experiments together with H.C.. I developed the model, analyzed the data and wrote most of the manuscript.

March 1, 2015 / Vol. 40, No. 5 / OPTICS LETTERS 843

Balancing of thermal lenses in enhancement cavities with transmissive elements

N. Lilienfein,[1,2,*] H. Carstens,[1,2] S. Holzberger,[1,2] C. Jocher,[3] T. Eidam,[3] J. Limpert,[3] A. Tünnermann,[3] A. Apolonski,[1,2] F. Krausz,[1,2] and I. Pupeza[1,2]

[1]*Max-Planck-Institut für Quantenoptik, Hans-Kopfermann-Str. 1, 85748 Garching, Germany*
[2]*Ludwig-Maximilians-Universität München, Fakultät für Physik, Am Coulombwall 1, 85748 Garching, Germany*
[3]*Friedrich-Schiller-Universität Jena, Institut für Angewandte Physik, Albert-Einstein-Str. 15, 07745 Jena, Germany*
**Corresponding author: nikolai.lilienfein@mpq.mpg.de*

Received December 5, 2014; accepted January 19, 2015;
posted January 22, 2015 (Doc. ID 229074); published February 27, 2015

Thermal lensing poses a serious challenge for the power scaling of enhancement cavities, in particular when these contain transmissive elements. We demonstrate the compensation of the lensing induced by thermal deformations of the cavity mirrors with the thermal lensing in a thin Brewster plate. Using forced convection to fine-tune the lensing in the plate, we achieve average powers of up to 160 kW for 250-MHz-repetition-rate picosecond pulses with a power-independent mode size. Furthermore, we show that the susceptibility of the cavity mode size to thermal lensing allows highly sensitive absorption measurements. © 2015 Optical Society of America

OCIS codes: (140.4780) Optical resonators; (140.7240) UV, EUV, and X-ray lasers.
http://dx.doi.org/10.1364/OL.40.000843

In high-finesse passive optical resonators, the pulses of a mode-locked laser can be coherently stacked to achieve a power enhancement of several orders of magnitude. Such enhancement cavities (ECs) are powerful tools for driving frequency conversion processes exhibiting low single-pass efficiencies such as high-order harmonic generation (HHG) in gaseous media [1,2] or inverse Compton scattering from relativistic electrons [3,4] at high repetition rates. Another promising application of this generic concept has been the “stack and dump” approach, where a stretched femtosecond pulse circulating in the EC is periodically dumped after having built up to allow for high pulse energies while almost maintaining the high input average power [5,6]. In the resonant state, high-finesse ECs exhibit an enhanced sensitivity towards changes of their longitudinal and transverse field distributions, making them uniquely sensitive measurement tools for application fields ranging from gravitational-wave detection [7] over molecular spectroscopy [8], to the measurement of linear [9] and nonlinear [10] polarization response of materials.

Together with intensity-related damages, thermal effects in the cavity optics ultimately limit the achievable intracavity peak and average power. In a previous work [11], we demonstrated the enhancement of ultrashort pulses to average powers of several hundreds of kilowatts. To avoid intensity-induced damage, large spot sizes on the mirrors are necessary. This can be conveniently achieved at an alignment-insensitive edge of the resonator stability zone [12]. Even though the dielectric mirrors employed in [11] were carefully chosen to minimize susceptibility to thermal lensing, at hundreds of kilowatts of average power, the transverse cavity mode was significantly affected by thermally induced changes. Many high-power applications require transmissive elements in the beam path of the EC, rendering thermal lensing an even more serious challenge. For instance, in cavity-enhanced HHG Brewster plates [13] or anti-reflection-coated plates placed at grazing incidence [14] can be used to couple out the generated radiation. Another example are nonlinear conversion processes in intracavity crystals, such as terahertz generation [15], intrapulse difference-frequency generation [16], or spectral broadening via self-phase modulation [17,18].

In this Letter, we experimentally and theoretically investigate thermally-induced changes in the size of the modes of high-finesse cavities containing transmissive elements. We show that the optics of an EC can be chosen such that the thermally-induced phase-front distortions largely compensate for each other. To precisely balance the contribution of a thin plate with those of the mirrors, we demonstrate a technique to fine-tune its thermal lensing characteristics. With this method, we achieve an intracavity average power of 160 kW in an EC containing a fused silica Brewster plate (BP), while drastically reducing thermally induced changes of the mode size. The susceptibility of the mode size to thermal lenses allows for measurements of total absorptions of thin transmissive plates in the range of 0.1 ppm.

The concept of combining optics with different dependencies of dioptric power on temperature to athermalize imaging systems has been used since the 1940s [19]. Later, this approach was used to mitigate self-induced thermal lensing of the gain medium in laser resonators [20–22], focusing optics for laser machining [23], and other high-power laser optics [24,25]. In ECs, such compensation has to be achieved at average powers of hundreds of kilowatts, which is orders of magnitude higher than in previous applications of the concept.

Thermal lensing of mirrors is caused by absorption of the incident power P in the coatings. The resulting thermal expansion of the substrate deforms the mirror surface, causing it to act as a defocusing optical element upon reflection. The thermally-induced radius of curvature R_{ref1} scales as [26]

$$R_{\mathrm{ref1}}^{-1} \propto -\frac{\alpha A}{\kappa w^2} \cdot P, \qquad (1)$$

with the absorption coefficient of the coating A, the thermal conductivity κ and thermal expansion coefficient α of the substrate, and the $1/e^2$ intensity radius w of the incident beam. By using coatings with an absorption of a few ppm and low-expansion glass substrates, thermal deformations can be alleviated [11]. However, the high bulk absorption of low-expansion glasses prevents their use as substrates for input couplers of ECs [11]. Thus, thermal lensing in state-of-the-art all-reflective ECs is dominated by the surface deformation of the input coupler.

In transmissive elements, thermal lensing effects are caused by absorption in the bulk material as well as in coatings. The resulting temperature distribution also leads to surface deformations, but usually their effect is negligible compared to the phase front distortions caused by the temperature-dependence of the refractive index dn/dT. The lensing effect scales as [27]

$$R_{\text{trans}}^{-1} \propto \frac{al}{\kappa w^2}\frac{dn}{dT}\cdot P, \tag{2}$$

with l being the thickness and a the absorption coefficient of the element. In most materials the temperature coefficient of the refractive index is positive, resulting in focusing thermal lenses. Because of the low temperatures and thermal gradients seen in the experiments, we neglect the dependence of the thermal conductivity on temperature, and stress-induced effects.

To understand how focusing and defocusing thermal phase front distortions affect a resonator, it is useful to distinguish between their parabolic and higher-order content. Purely parabolic phase front distortions act as perfect lenses altering the focusing geometry of the cavity and, thus, its position in the stability zone. This changes the mode size and can lead to configurations where higher order transverse modes are degenerate with the fundamental mode [28]. The dependence of the mode size on the focusing geometry diverges at the edges of the stability zone. To avoid mirror damage, the EC can be operated close to the inner edge of stability, where the illuminated areas on the mirrors are increased [12]. Here, a defocusing thermal lens pushes the cavity further towards the edge. Additionally, all transverse modes with even orders converge at this edge of stability [28]. The higher order content of thermal phase front distortions facilitates coupling of the fundamental transverse mode to higher order modes, causing losses [11]. These effects make a precise compensation of both thermal lensing and aberrations desirable. Conversely, the susceptibility of high-finesse cavities to thermal effects can be exploited to measure small absorptions with a high sensitivity [29,30].

We simulated the deformation of the input coupler caused by the absorption of a Gaussian beam using the finite-element solver COMSOL. Figure 1 shows the phase front distortion produced by a beam of 100 kW on a mirror with a coating of 5 ppm absorption and a fused-silica substrate. Heat exchange with the ambience is assumed to take place only via radiation, with the emissivity of the mirror being 0.95. A parabolic fit to this profile, weighted with the incident intensity profile, yields its dioptric power. The residuals of this fit represent aberrations. We find that a thin fused-silica plate placed in a collimated arm of the cavity is well suited to compensate for the thermal aberrations of the input coupler (Fig. 1). The plate is placed at Brewster's angle to minimize losses and to avoid additional absorption in anti-reflection coatings [Fig. 2(a)]. The projection of a round beam on the plate is then an ellipse, with the ratio of its major to its minor axis being about 1.76. This leads to astigmatism of the thermal lens, with the shorter focal length in the plane of the tilt.

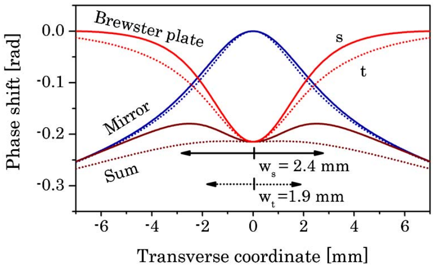

Fig. 1. Simulated thermal phase distortion profiles induced by an elliptical Gaussian beam. Profiles are plotted for a mirror, a Brewster plate, and their sum in both the sagittal (s, solid lines) and tangential planes (t, dotted lines).

Because of the different shapes of the heating patterns on the input coupler and on the BP, their thermal lenses cannot be perfectly matched in the sagittal and tangential planes simultaneously [Fig. 1]. Thus, the ellipticity of the cavity mode will change with intracavity power. For a cavity close to the inner edge of the stability zone with non-zero angles of incidence on the curved mirrors, the mode is elliptical in the cold state. Its major axis lies in the sagittal plane of the mirrors. By placing the BP such that the tilt angle is within this plane, its astigmatic thermal lensing behavior can be exploited to compensate for the initial ellipticity at a given intracavity power.

To model the thermal sensitivity of a specific cavity design, we use the metric introduced in [11], given by the slope of the beam radius on a curved mirror as a function of the intracavity average power. Close to the inner edge of the stability zone the mode change evolves nearly linear with the intracavity power, making this metric a useful tool to estimate the behavior of the cavity even for high powers [11]. First, we calculate the mode size in both planes for the cold, i.e., low-power cavity. Next, we simulate the heating of the input coupler and of the BP by this beam for a small power in 3D using COMSOL

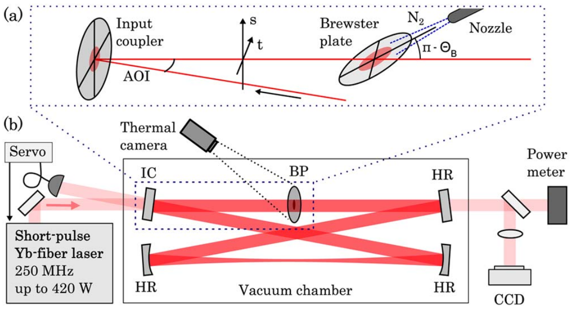

Fig. 2. (a) Sketch of the compensation scheme. The Brewster plate (BP) is tilted in the sagittal plane. The minimal angle of incidence (AOI) depends on the distance between input coupler (IC) and BP, and the mode size. The plate can be cooled with nitrogen gas. (b) Schematic of the experimental setup.

and extract the resulting phase distortion profiles (Fig. 1). From these we obtain the sagittal and tangential focusing powers of the thermal lenses by a parabolic fit, weighted with the incident intensity profile. By plugging the resulting thermal lenses into the cavity model, we calculate the mode size of the warm cavity and its thermal sensitivity. In Fig. 3, a the thermal sensitivity of a symmetric 2.4-m bow-tie cavity is plotted against the initial mode size. The simulations were performed for cavity configurations close to the inner stability edge, with the positions in the stability zone corresponding to the initial mode size [Fig. 3(a)].

In the experiment, we use a four-mirror cavity seeded by the Yb:fiber-based chirped-pulse-amplification laser system published in [31]. It delivers 250-fs pulses centered at 1040 nm with a repetition rate of 250 MHz and up to 420 W of average power. The pulses were stretched to about ten picoseconds for the experiments to exclude nonlinear effects. The laser is locked to the EC using the Pound-Drever-Hall scheme. The cavity comprises three high-reflectance mirrors with ultra-low-expansion glass substrates and an input coupler with a reflectivity of 99.85% on a fused-silica substrate, and is placed in a vacuum chamber [Fig. 2(b)]. It is set up in a symmetric bow-tie geometry [12] with two 600-mm radius-of-curvature mirrors. The distance between the curved mirrors can be varied to adjust the position in the stability zone. We use a round BP made of fused silica (Suprasil 311, Heraeus), with a diameter of 25 mm and a thickness of 100 μm. To avoid clipping the cavity beam while minimizing the angles of incidence on the mirrors, the BP is placed as indicated in Fig. 2. To determine the thermal sensitivity of the cavity, the mode profile on one of the curved mirrors was measured for a range of intra-cavity powers using the same diagnostics as described in [11]. The obtained data was fitted by a linear function. The thermal sensitivity is given by the slope of the fit function, and the initial mode size corresponds to its value at zero power [Fig. 3(b)]. Measurement series were performed with and without the BP for different cavity configurations close to the inner stability edge [Fig. 3(a)].

The model can be fitted to the experimental results by using the absorptions of the input coupler and of the BP as free parameters. For absorption values of 3.2 ppm in the mirror and 0.28 ppm in the plate, theory and experiment show excellent agreement [Fig. 3(a)]. The measurements allow distinguishing absorptions with a resolution of about 0.5 ppm in mirrors and 0.02 ppm in BPs. With the Brewster plate, a clean, round mode is achieved at 62 kW with a power enhancement factor of 1300. The experiments demonstrate that the astigmatism of the thermal lens from the BP can be used to eliminate the initial mode ellipticity. Still, the thermal sensitivity differs significantly from zero, meaning that the balancing of thermal lenses is not perfect [Fig. 3(b)].

In principle, a good compensation is achievable by precisely choosing the thickness of the BP. However, the manufacturing tolerance and availability of plates, as well as small changes in the surface absorption of individual plates in between experiments, make this approach impractical. To overcome this problem, we exploit the high surface-to-volume ratio of the thin BP. It allows for an efficient manipulation of the amount of heat emitted within the illuminated area, and thus of the strength of the thermal lens. This can be achieved by changing the ambient temperature apparent to the plate, or by facilitating heat transport through a gas. Here, we expose a BP of 200 μm thickness to forced convection by directing a steady flow of nitrogen along its surface [Fig. 2(a)]. This method offers a broad range of tunability [Fig. 4(a)]. With this scheme, we achieve an intracavity average power of 160 kW, i.e., with an enhancement factor of 1035, and a nearly constant mode size [Fig. 4(a)]. At this power, losses from thermally induced aberrations prevent further scaling [Fig. 4(b)]. These aberrations seem to stem primarily from the inhomogeneous cooling of the BP [Fig. 4(c)–4(e)], resulting in a significant tilt of

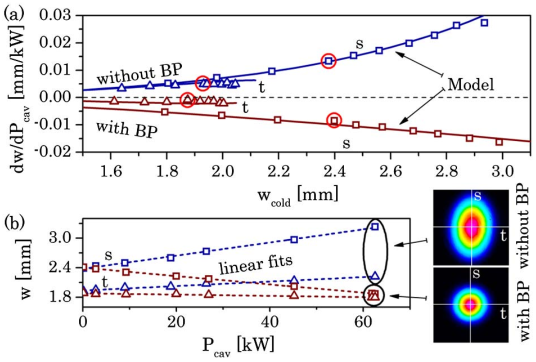

Fig. 3. (a) Thermal sensitivity plotted versus the initial mode size in both the sagittal (*s*, squares) and tangential (*t*, triangles) plane. The model (solid lines) agrees well with the experimental results (symbols). The points marked by red circles are derived from the data shown in (b). (b) Beam radius versus intracavity power with and without a Brewster plate (BP) (symbols) and linear fits (dashed lines). Beam profiles are shown for both cases at an intracavity power of 61 kW.

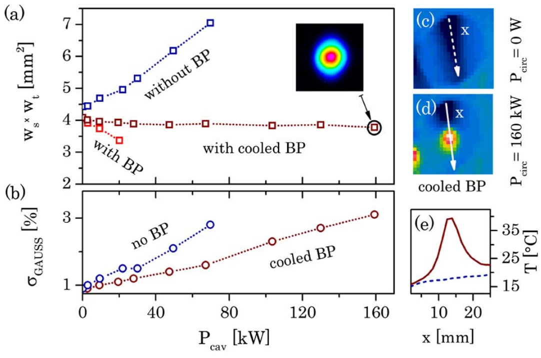

Fig. 4. (a) Mode area versus intracavity power for the same cavity without a Brewster plate, with an uncooled and with a cooled Brewster plate. The inset shows a mode profile achieved with the cooled BP at 160 kW. (b) Standard deviation of the Gaussian fit to the mode profile in the sagittal plane, indicating increasing aberrations. (c),(d) Images of the temperature distribution on the cooled Brewster plate for two powers. The arrow indicates the direction of the cooling gas flow. (e) Temperature profiles on the Brewster plate along the arrows exhibit a significant asymmetry of the thermal lens.

the temperature profile in the sagittal plane, which becomes more severe with increasing power. This technological limitation can in principle be overcome by improving the cooling of the BP. A promising alternative to forced convection could be radiative cooling [32].

In conclusion, we have investigated the enhancement of ultrashort pulses in a high-finesse EC containing a transmissive element. We have demonstrated that the thermal lenses induced in the cavity mirrors and in a thin plate placed at Brewster's angle in the beam path can be balanced with high precision by controlling forced convection of the plate. We have also shown that thermal lensing in BPs can be exploited to compensate for astigmatism in cavities operated close to the edge of stability. With this scheme, we obtained a constant mode size up to 160 kW of average power, which exceeds the performance of state-of-the-art ECs with transmissive elements by more than one order of magnitude. Furthermore, we show that the sensitivity of the cavity mode change with respect to the thermal lens induced in thin plates allows for the detection of absorption values in the range of ~0.1 ppm. The methodology applied in this work will benefit the power scaling of ECs, in particular for applications requiring the inclusion of transmissive elements like nonlinear crystals or output couplers for radiation generated via intracavity conversion processes.

We thank Johannes Weitenberg for helpful discussions. This work was supported by the Deutsche Forschungsgemeinschaft (DFG) Cluster of Excellence, Munich Centre for Advanced Photonics (MAP), by the Bundesministerium für Bildung und Forschung (BMBF) under Photonische Nanomaterialien (PhoNa), contract number 03IS2101B, by the Fraunhofer-Max Planck project MEGAS, and by the European Research Council under the ERC grant agreement no. [617173] ACOPS.

References

1. C. Gohle, T. Udem, M. Herrmann, J. Rauschenberger, R. Holzwarth, H. A. Schuessler, F. Krausz, and T. W. Hänsch, Nature **436**, 234 (2005).
2. I. Pupeza, S. Holzberger, T. Eidam, H. Carstens, D. Esser, J. Weitenberg, P. Rußbüldt, J. Rauschenberger, J. Limpert, T. Udem, A. Tünnermann, T. W. Hänsch, A. Apolonski, F. Krausz, and E. Fill, Nat. Photonics **7**, 608 (2013).
3. Z. Huang and R. Ruth, Phys. Rev. Lett. **80**, 976 (1998).
4. J. Bonis, R. Chiche, R. Cizeron, M. Cohen, E. Cormier, P. Cornebise, N. Delerue, R. Flaminio, D. Jehanno, F. Labaye, M. Lacroix, R. Marie, B. Mercier, C. Michel, Y. Peinaud, L. Pinard, C. Prevost, V. Soskov, A. Variola, and F. Zomer, J. Inst. **7**, P01017 (2012).
5. Y. Vidne, M. Rosenbluh, and T. W. Hansch, Opt. Lett. **28**, 2396 (2003).
6. S. Breitkopf, T. Eidam, A. Klenke, L. von Grafenstein, H. Carstens, S. Holzberger, E. Fill, T. Schreiber, F. Krausz, A. Tünnermann, I. Pupeza, and J. Limpert, Light Sci. Appl. **3**, e211 (2014).
7. G. M. Harry, Class. Quantum Grav. **27**, 84006 (2010).
8. F. Adler, M. J. Thorpe, K. C. Cossel, and J. Ye, Annu. Rev. Anal. Chem. **3**, 175 (2010).
9. I. Pupeza, X. Gu, E. Fill, T. Eidam, J. Limpert, A. Tünnermann, F. Krausz, and T. Udem, Opt. Express **18**, 26184 (2010).
10. S. Holzberger, N. Lilienfein, H. Carstens, T. Saule, F. Lücking, M. Trubetskov, V. Pervak, T. Eidam, J. Limpert, A. Tünnermann, E. Fill, F. Krausz, and I. Pupeza are preparing a manuscript to be called "Femtosecond enhancement cavities in the nonlinear regime."
11. H. Carstens, N. Lilienfein, S. Holzberger, C. Jocher, T. Eidam, J. Limpert, A. Tünnermann, J. Weitenberg, D. C. Yost, A. Alghamdi, Z. Alahmed, A. Azzeer, A. Apolonski, E. Fill, F. Krausz, and I. Pupeza, Opt. Lett. **39**, 2595 (2014).
12. H. Carstens, S. Holzberger, J. Kaster, J. Weitenberg, V. Pervak, A. Apolonski, E. Fill, F. Krausz, and I. Pupeza, Opt. Express **21**, 11606 (2013).
13. C. Benko, T. K. Allison, A. Cingöz, L. Hua, F. Labaye, D. C. Yost, and J. Ye, Nat. Photonics **8**, 530 (2014).
14. O. Pronin, V. Pervak, E. Fill, J. Rauschenberger, F. Krausz, and A. Apolonski, Opt. Express **19**, 10232 (2011).
15. M. Theuer, D. Molter, K. Maki, C. Otani, J. A. L'huillier, and R. Beigang, Appl. Phys. Lett. **93**, 41119 (2008).
16. I. Pupeza, D. Sánchez, J. Zhang, N. Lilienfein, M. Seidel, O. Pronin, N. Karpowicz, T. Paasch-Colberg, I. Znakovskaya, V. Pervak, E. Fill, Z. Wei, F. Krausz, A. Apolonski, and J. Biegert are preparing a manuscript to be called "High-power sub-2-cycle mid-infrared pulses at 100 MHz repetition rate."
17. K. D. Moll, R. J. Jones, and J. Ye, Opt. Express **13**, 1672 (2005).
18. V. L. Kalashnikov, Appl. Phys. B **92**, 19 (2008).
19. J. W. Perry, Proc. Phys. Soc. London **55**, 257 (1943).
20. N. P. Barnes and D. J. Gettemy, J. Opt. Soc. Am. **70**, 1244 (1980).
21. R. Koch, Opt. Commun. **140**, 158 (1997).
22. E. Wyss, M. Roth, T. Graf, and H. P. Weber, IEEE J. Quantum Electron. **38**, 1620 (2002).
23. M. Scaggs and G. Haas, Proc. SPIE **7913**, 79130C (2011).
24. S. Piehler, C. Thiel, A. Voss, M. Abdou Ahmed, T. Graf, E. Beyer, and T. Morris, Proc. SPIE **8239**, 82390Z (2012).
25. M. Stubenvoll, B. Schäfer, and K. Mann, Opt. Express **22**, 25385 (2014).
26. W. Winkler, K. Danzmann, A. Rüdiger, and R. Schilling, Phys. Rev. A **44**, 7022 (1991).
27. J. P. Gordon, R. C. C. Leite, R. S. Moore, S. P. S. Porto, and J. R. Whinnery, J. Appl. Phys. **36**, 3 (1965).
28. J. Weitenberg, P. Rußbüldt, I. Pupeza, T. Udem, H.-D. Hoffmann, and R. Poprawe, "Geometrical on-axis access to high-finesse resonators by quasi-imaging: a theoretical description," J. Opt. (to be published).
29. S. Hild, H. Lück, W. Winkler, K. Strain, H. Grote, J. Smith, M. Malec, M. Hewitson, B. Willke, J. Hough, and K. Danzmann, Appl. Opt. **45**, 7269 (2006).
30. N. Lastzka, J. Steinlechner, S. Steinlechner, and R. Schnabel, Appl. Opt. **49**, 5391 (2010).
31. C. Jocher, T. Eidam, S. Hädrich, J. Limpert, and A. Tünnermann, Opt. Lett. **37**, 4407 (2012).
32. C. Justin Kamp, H. Kawamura, R. Passaquieti, and R. DeSalvo, Nucl. Instrum. Methods Phys. A **607**, 530 (2009).

Chapter 6

Femtosecond enhancement cavities in the nonlinear regime

by

Simon Holzberger, Nikolai Lilienfein, Henning Carstens, Tobias Saule,
Maximilian Högner, Fabian Lücking, Michael Trubetskov, Vladimir Pervak,
Tino Eidam, Jens Limpert, Andreas Tünnermann, Ernst Fill Ferenc Krausz and
Ioachim Pupeza

published in

Physical Review Letters (2015)
DOI: 10.1103/PhysRevLett.115.023902

Reprinted from [115]
with permission from the American Physical Society.

Contributions

The model was developed by S.H.. I performed the experiments together with S.H., discussed simulations and results with S.H. and I.P., and contributed to the manuscript.

PRL **115,** 023902 (2015) PHYSICAL REVIEW LETTERS week ending 10 JULY 2015

Femtosecond Enhancement Cavities in the Nonlinear Regime

S. Holzberger,[1,2,*] N. Lilienfein,[1,2] H. Carstens,[1,2] T. Saule,[1,2] M. Högner,[1,2] F. Lücking,[2] M. Trubetskov,[1] V. Pervak,[2] T. Eidam,[3] J. Limpert,[3] A. Tünnermann,[3] E. Fill,[1,2] F. Krausz,[1,2] and I. Pupeza[1,2]
[1]*Max-Planck-Institut für Quantenoptik, Hans-Kopfermann-Straße 1, 85748 Garching, Germany*
[2]*Ludwig-Maximilians-Universität München, Am Coulombwall 1, 85748 Garching, Germany*
[3]*Friedrich-Schiller-Universität Jena, Institut für Angewandte Physik, Albert-Einstein-Straße 15, 07745 Jena, Germany*

(Received 30 December 2014; published 8 July 2015)

We combine high-finesse optical resonators and spatial-spectral interferometry to a highly phase-sensitive investigation technique for nonlinear light-matter interactions. We experimentally validate an *ab initio* model for the nonlinear response of a resonator housing a gas target, permitting the global optimization of intracavity conversion processes like high-order harmonic generation. We predict the feasibility of driving intracavity high-order harmonic generation far beyond intensity limitations observed in state-of-the-art systems by exploiting the intracavity nonlinearity to compress the pulses in time.

DOI: 10.1103/PhysRevLett.115.023902 PACS numbers: 42.65.Ky, 42.60.Da, 52.38.-r

During light-matter interactions, the properties of the light field are subjected to changes reflecting the physical mechanisms underlying the interaction and revealing fundamental properties of matter. A powerful tool for high-precision studies of light-matter interactions is the passive optical resonator, also known as enhancement cavity (EC). An EC can be resonantly excited by laser light, resulting in an enhancement of the input power and of the single-round-trip phase by up to several orders of magnitude. ECs have been successfully employed for high-sensitivity measurements of absorption [1] and of dispersion [2,3] in the linear regime. Here, we present the first quantitative study of the nonlinear phase associated with the propagation of an ultrashort laser pulse through a nonlinear medium exploiting the sensitivity enhancement of more than 2 orders of magnitude provided by an EC.

In the last decade, the advent of high-power femtosecond lasers and the design of adequate ECs have enabled ultrashort pulses with an otherwise unattainable combination of peak intensities and average powers [4]. The most prominent application has been high-order harmonic generation (HHG) in an intracavity gas target, at repetition rates exceeding 10 MHz [5–9]. Although cavity-enhanced HHG has matured to deliver phase-stable extreme-ultraviolet (XUV) frequency combs enabling first spectroscopic experiments [7,8], all state-of-the-art EC-HHG systems suffer from a saturation behavior of the intracavity intensity with respect to the input peak power, referred to as *intensity clamping* [9–12]. Currently, this severely limits the further scaling of the photon flux and of the XUV photon energies attainable with this technology and questions its applicability to other nonlinear conversion processes. The models developed so far [11,12] capture the main physical mechanisms of this limitation qualitatively but do not allow for accurate quantitative predictions, such that optimizing the cavity design with respect to the nonlinear conversion remains an open challenge.

In this Letter, we use the phase sensitivity of a high-finesse EC—the very effect responsible for the intensity clamping—to precisely study the nonlinear interaction of a laser pulse with a gas target. The full pulse characterization in the spectral domain allows for the formulation of a quantitative, *ab initio* nonlinear propagation model, experimentally validated in a wide range of the critical parameters. Second, we use this model to derive a scaling law quantitatively describing the intensity-clamping behavior in ECs employing mirrors according to the *standard approach* used in all setups reported so far, i.e., a uniform spectral reflectivity, symmetric with respect to the input spectrum. This analytic expression enables the optimization of the nonlinear conversion efficiency in standard-approach ECs. Third, we address the question of whether or not nonlinear ECs can be operated beyond the intensity limitations exhibited by the standard approach. We demonstrate that the ionization-induced spectral broadening in conjunction with cavity mirrors with tailored reflectivity can be used to dramatically compress the intracavity pulse in time, while maintaining a high power enhancement factor. This finding represents the first viable route towards significantly surpassing the intensity limitations of state-of-the-art nonlinear ECs and, therefore, reveals an enormous new potential of the EC technology for building high-power, broadband, coherent sources in spectral ranges where suitable laser materials are absent, such as the XUV, the midinfrared, and the THz ranges.

The experimental setup is depicted in Fig. 1. The chirped-pulse-amplification-based Yb-fiber laser system has been previously described in Refs. [2,13]. It delivers a 77-MHz train of near-Fourier-limited 180-fs pulses carried at a wavelength of 1040 nm. The pulses can be linearly chirped to 640 fs, or spectrally broadened in a

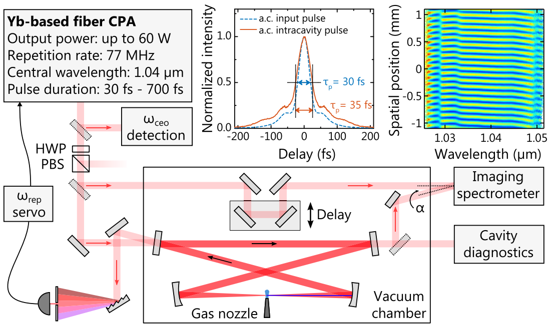

FIG. 1 (color online). Experimental setup: laser system with optional fiber broadening and compression, comb offset frequency (ω_{ceo}) detection unit, enhancement cavity ($1/e^2$ focus radius: 25 μm), active stabilization of the center frequency to the cavity resonance, and imaging spectrometer. The offset frequency of the laser is adjustable and free running. Insets: autocorrelation trace of laser and intracavity pulse for compressed input pulses and interferogram showing distinct phase jumps. HWP: half-wave plate, PBS: polarizing beam splitter.

photonic-crystal fiber and compressed via chirped mirrors to 30 fs. The pulses are coherently enhanced in a standard-approach EC. With 30-fs input pulses, an intracavity pulse duration of 35 fs at a power enhancement factor of 250 was reached, leading to an average power of 3.3 kW without a gas target.

Besides a power enhancement, the resonant cavity provides a means of enhancing the single-round-trip phase. We employ spatial-spectral interferometry to measure the spectral phase difference between the intracavity and the input pulses [2,14]. Replicas of each of these beams intersect noncollinearly at the entrance slit of an imaging spectrometer. The resulting interference pattern in the spatial and spectral plane (y, ω) is given by

$$I(y,\omega) = I_{\mathrm{in}}(y,\omega) + I_{\mathrm{cav}}(y,\omega) + 2\sqrt{I_{\mathrm{in}}(y,\omega) I_{\mathrm{cav}}(y,\omega)} \cos\left(\phi(\omega) + \frac{y\omega}{c}\sin\alpha\right). \tag{1}$$

Here, $\phi(\omega)$ is the relative spectral phase of the two pulses and α is the intersection angle of the two beams. From Eq. (1) the acquired phase $\phi(\omega)$ can be directly retrieved, without the necessity of characterizing the phases of both pulses individually. Only quadratic and higher-order terms in ω are considered, as there are multiple uncontrolled sources of group delays. Thus, a linear function must be added when comparing the retrieved phases to simulations. Both beams have to be matched in the transverse dimension and should exhibit good spatial homogeneity. When using fiber-broadened pulses this is the main source of experimental uncertainty in the retrieved phase, limiting the sensitivity to about 60 mrad. To date, spatial-spectral interferometry together with ECs has been used for measuring the single-round-trip group delay dispersion in the linear regime with a sensitivity of less than 1 fs^2 [2]. Here, we use this technique to investigate the phase modulation induced in a nonlinear interaction driven in the steady-state regime of an EC.

Our model describing the pulse propagation through the ionized medium in the cavity focus is based on the first-order propagation equation derived in Ref. [15] within the approximation of a 1D envelope description as given in Ref. [11]. In short, the nonlinear laser-gas interaction is governed by a differential equation for the pulse envelope $A(z,\tau)$ that reads in the comoving reference frame

$$\frac{dA(z,\tau)}{dz} = -\frac{I_p n}{2\epsilon_0 c}[1-\eta(z,\tau)]\Gamma_{\mathrm{peak}}(\tau)\frac{A(z,\tau)}{|A(z,\tau)|^2} + i r_e \lambda_c n \eta(z,\tau) A(z,\tau). \tag{2}$$

The first term on the right-hand side accounts for the energy loss upon ionization (I_p, ionization potential; n, gas number density; η, ionized fraction; Γ_{peak}, peak ionization rate; r_e, classical electron radius; λ_c, carrier wavelength) and the second term describes a temporal phase shift due to the rapidly changing electron density $n_e = n\eta$. Although the derivation of Eq. (2) was originally intended for pulses consisting of many cycles in the low-intensity regime, we verified that the agreement of Eq. (2) with its original counterpart (see Eq. (7) in Ref. [15]) is still excellent even for 10-fs pulses (comprising only a few cycles) and for peak intensities of 8×10^{13} W/cm^2 in a Xe gas target (see Supplemental Material [16], also for Ar and Ne).

The build-up process of the intracavity pulse is described in the frequency domain:

$$\tilde{A}_{\mathrm{cav,prior}}(\omega) = \sqrt{1-R_{\mathrm{ic}}(\omega)}\tilde{A}_{\mathrm{in}}(\omega) + \sqrt{R_{\mathrm{ic}}(\omega)R_{\mathrm{cav}}(\omega)}e^{i\phi_{\mathrm{rt}}(\omega)}\tilde{A}_{\mathrm{cav,post}}(\omega). \tag{3}$$

Here, R_{ic} is the reflectivity of the input coupler, R_{cav} represents the product of the reflectivities of all other cavity mirrors, and $\tilde{A}$ denotes the Fourier components of the field envelope (with indices for the input field and for the field before and after the plasma interaction). The spectral phase $\phi_{\mathrm{rt}}(\omega)$ is acquired upon one cavity round-trip and includes the contribution from the ionization-induced plasma. A split-step Fourier algorithm is used to solve the coupled equations (2) and (3). The employed 1D model neglects the spatial dependence of the nonlinearity and, therefore, the coupling of energy to higher-order transverse modes. Since the cavity is operated such that only the fundamental mode is resonant, transverse effects of the plasma result in additional losses and the cavity beam profile remains spatially homogeneous. This is confirmed by the imaging 2D spectrometer. For typical gas-density-length products that are below 2×10^{17} cm^{-2} and for the intensity range studied here, the 1D model is a good approximation (see Supplemental Material [16] for comparison to 4D simulation).

All inputs to the model are taken as measured or as calculated by other independent simulations so that fit parameters are not necessary. Since the cross-sectional density of freed electrons determines the phase shift, it is essential to mimic this quantity when approximating the 2D spatial beam profile by a flattop profile with similar peak intensity. Therefore, we scale the ionization rate such that for every peak intensity it generates as many electrons within the flattop intensity profile as would have been released in the Gaussian beam profile with the original ionization rate. In contrast to earlier works [11,12], we find the Perelomov-Popov-Terent'ev model [25] averaged over the magnetic quantum number to be better suited for the intensity range under investigation, i.e., for Keldysh parameters greater than 1. In particular, using Ammosov-Delone-Krainov theory [26] underestimates the nonlinearity and thus leads to a significant overestimation of the reachable intracavity peak intensity (~25%). Whenever the consideration of subcycle ionization dynamics is necessary, we use the extension of the Perelomov-Popov-Terent'ev rate as given in Ref. [27].

From fluid flow simulations, the velocity of the gas atoms is calculated to be about 220 m/s. This is not sufficient to replace the plasma with new atoms in the interaction region (~20 μm) within one cavity round-trip time of 13 ns. Therefore the decay of the plasma is considered and modeled according to the dominant recombination mechanism via three-body collisions (see Supplemental Material [16]). However, the cavity response is mainly affected by the temporal phase shift and not by the dispersive effects of a preexisting plasma. This holds when the induced group-delay dispersion is below 0.2 fs^2 and when the depletion of the neutral gas is small ($\lesssim$15%). At the gas parameters used in the experiments, both criteria are fulfilled, rendering more detailed modeling unnecessary.

In Fig. 2(a), three examples of recorded spectra and spectral phase shifts of the intracavity pulse are presented. For the simulations, the mirror reflectivities and phases are taken from multilayer design calculations and the gas parameters are extracted from fluid flow simulations. The input pulse parameters are set as measured. For the broadband pulses, the deviation of the comb offset frequency from the value required by the cavity for optimum enhancement is particularly critical, because even deviations as small as 2 MHz from the optimum value lead to a drop in intracavity power by 50% and to a spectral filtering. The offset frequency is, however, sufficiently stable on the time scale of data acquisition, that active stabilization is not compelling (beat-note linewidth ~200 kHz, measured with a resolution bandwidth of 100 kHz). A small detuning of the locked central comb line from the empty cavity resonance is introduced avoiding the regime of optical bistability [10,11], and keeping intracavity power fluctuations below 1% rms (band: 2.5 Hz to 5 MHz) and ensuring operation close to the maximum of the nonlinear resonance. The agreement between the simulated spectra and phases to the measured ones is excellent, validating the 1D nonlinear cavity model in a broad parameter range. Simulations yield the ionized population before the pulse and the ionization per pulse to be both on the order of 2×10^{16} cm^{-3}.

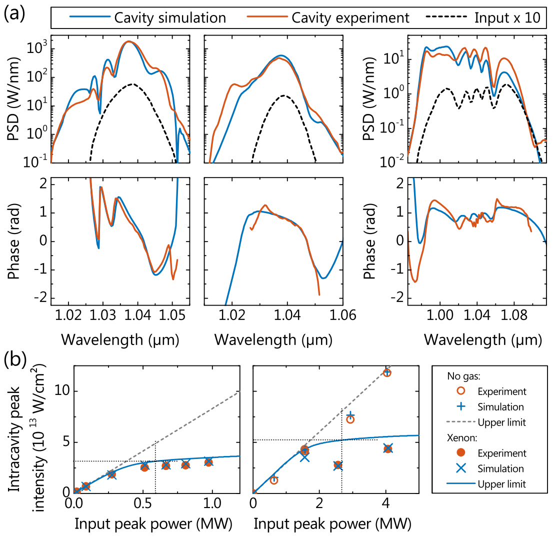

FIG. 2 (color online). Validation of the nonlinear cavity model in a standard-approach cavity. (a) Measured power spectral densities (PSD, upper panel) and acquired phases (lower panel) of the intracavity pulse along with simulation results. Left to right: input pulse duration, 640 fs (upchirped); 180 fs (Fourier limited); 30 fs (fiber broadened). Without ionization, the spectrum is symmetrically enhanced around the central wavelength. (b) Intracavity peak intensity as a function of input peak power for 640-fs (left) and for 30-fs pulses (right). The outlier in the right panel is due to an incorrectly set offset frequency of the comb. Gas density, 9×10^{18} cm^{-3}; interaction length, 180 μm; finesse, 1190 (narrowband case) and 950 (broadband case).

Figure 2(b) depicts the dependence of the intracavity peak intensity on the input peak power for two different pulse durations. Both curves reveal the intensity clamping behavior reported previously [9,10]. Again, the simulated intensities agree well with the experimentally determined ones. From the simulations we deduce an upper limit for the intracavity intensity [solid line in Fig. 2(b)]. This is found by optimizing the input frequency comb (ω_r, ω_{ceo}) while keeping all other parameters fixed. It has been shown that this optimum is located at nonzero detuning of the comb from the linear cavity resonances and coincides with a local bifurcation of the intracavity power at which stable operation of the cavity is impossible [11].

To optimize the nonlinear laser-gas interaction, e.g., for maximizing conversion efficiency to the XUV via HHG

[28], a simple expression relating the achievable intracavity intensity to the given cavity, gas, and input pulse parameters is desirable. To this end, we calculate the clamping behavior for a broad range of hundreds of different combinations of values for the gas parameters (density-length product, $nl = 4\text{–}20 \times 10^{16}\ \mathrm{cm}^{-2}$), the finesse ($\mathcal{F} = 250\text{–}2500$) and the pulse duration ($\tau = 12\text{–}600$ fs). Standard-approach cavities are considered: we assume a uniform mirror reflectivity, symmetric to the central wavelength and zero group delay dispersion over sufficient bandwidth to limit intracavity pulse lengthening to 1% in the absence of gas and at an input coupler transmission of 1%. Although the intracavity intensity seems to be unbound, the distinct saturation behavior motivates the definition of a clamping intensity. We find that for given gas and pulse parameters and for a targeted intensity there is an optimum cavity finesse that minimizes the required input peak power. Conversely, each finesse is optimal for a desired intensity. This intensity is reached when the peak power enhancement has dropped to about 60% to 70% of its value without a gas target. Therefore, we define the clamping intensity I_{CL} as the intracavity intensity, at which the peak power enhancement equals 65% of its linear value [see dotted cross in Fig. 2(b)]. We find that the following empirical law with the parameters α, β, γ, and δ describes the entire range of simulations within 7% of accuracy:

$$I_{\mathrm{CL}}(\tau, \mathcal{F}, nl) = I_0 \times \left(\frac{\tau_0 - \alpha}{\tau - \alpha} \frac{\mathcal{F}_0 - \beta}{\mathcal{F} - \beta} \frac{n_0 l_0 - \gamma}{nl - \gamma} \right)^{\delta}. \quad (4)$$

All coefficients are given in Table I. It is not surprising that the three input parameters pulse duration, finesse, and the gas-density-length product scale with the same exponent δ: in terms of accumulated temporal phase shift, increasing the finesse is very similar to having a longer or denser gas jet or to increasing the pulse duration. The small value of δ is a direct consequence of the high degree of nonlinearity of the ionization process. It reveals that the ionization constitutes a rather severe limit for scaling the intensity in the presence of an intracavity gas target. For instance, in the clamping regime doubling the intensity requires a decrease in any of the other parameters by roughly a factor of 90.

TABLE I. Parameters for the empirical scaling law of Eq. (4) describing the intensity clamping. $\tau_0 = 100$ fs, $\mathcal{F}_0 = 416$, and $n_0 l_0 = 8 \times 10^{16}\ \mathrm{cm}^{-2}$. Simulations were performed with a repetition rate of 100 MHz and with a gas target length of 200 μm. The bandwidth of the ECs corresponded to the input pulse durations at 1.04 μm central wavelength.

	Xenon	Argon	Neon
α (fs)	0.8	3.3	5.3
β	61	69	72
γ ($10^{16}/\mathrm{cm}^2$)	0.96	0.97	1.0
δ	0.159	0.153	0.148
I_0 (10^{14} W/cm^2)	0.461	1.24	3.72

For our intensity range, the phase-modulation term in Eq. (2) is the predominant limitation. For a single pass through the gas target it takes the approximate form $\Theta(t) = r_e \lambda_c \eta(t) nl$. At the clamping limit intensity the single-pass phase shift at the end of the pulse takes the value of about $\Theta_{\max} = 6.3/\mathcal{F}$ with a minor dependence on other parameters. This is about a factor of 2 higher than the previously reported rule of thumb of $\pi/\mathcal{F}$ [12,29]. The expression for Θ and the tolerable single-pass phase shift $\Theta_{\max}$ are a good starting point for transferring our findings to other driving wavelengths, e.g., for extending the XUV cutoff wavelength (see Supplemental Material [16]).

The tradeoff between intracavity intensity and cavity finesse [see Eq. (4)] raises the question of whether parameters leading to record XUV conversion efficiencies in single-pass HHG experiments [30] can ever be reached in ECs at a reasonable power enhancement. With our experimentally validated model this question can be addressed by designing cavity mirrors to optimize the peak power enhancement in the presence of a gas target with parameters for efficient HHG [30]. In the following example, we seek for a steady-state solution of Eq. (3) presupposing the intracavity pulse $\tilde{A}_{\mathrm{cav,prior}}$ with a peak intensity of $8 \times 10^{13}\ \mathrm{W/cm^2}$, from which $\tilde{A}_{\mathrm{cav,post}}$ directly follows. Using this ansatz, the input coupler reflectivity $R_{\mathrm{ic}}(\omega)$ can be calculated such that the required input power [$\propto |\tilde{A}_{\mathrm{in}}(\omega)|^2$] is minimized. In this example, we consider an EC equipped with broadband complementary-phase mirrors [31,32] supporting a bandwidth of 260 nm. The presupposed intracavity spectrum is manually varied to maximize the peak power enhancement. With the spectra shown in Fig. 3(a), a peak power enhancement surpassing 450 is possible at intracavity pulse durations of 10 fs with incident pulses as long as 52 fs. Since the intracavity

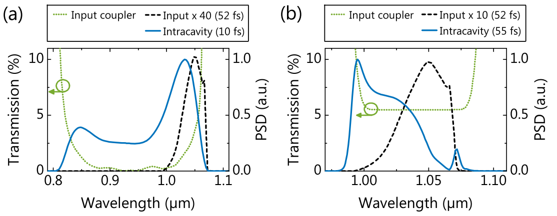

FIG. 3 (color online). (a) Example of a tailored input coupler transmission for best peak power enhancement at $8 \times 10^{13}\ \mathrm{W/cm^2}$ peak intensity and corresponding intracavity and input spectrum (right y axis). Note the reduced width of the input spectrum. (b) The same input spectrum enhanced in a standard cavity requires a 10 times more powerful laser to reach the same peak intensity at 5 times longer intracavity pulses. Xe gas target length, 400 μm; particle density, $2.5 \times 10^{18}\ \mathrm{cm}^{-3}$.

nonlinearity constantly transfers energy from the red part of the spectrum to the blue end, it is sufficient to pump the cavity in the long-wavelength region, in a comparatively narrow bandwidth. We verified that the solution is stable against fluctuations of up to 8% of the input power and of the pulse duration, and against a shift of the carrier wavelength of several nanometers. In contrast, enhancing the same seeding laser spectrum to the same peak intensity in a standard-approach cavity, requires 10 times the incident power and results in considerably longer intracavity pulses [see Fig. 3(b)]. The peak power enhancement and the intracavity pulse compression in the optimized EC will boost the conversion efficiency by more than 3 orders of magnitude compared to a single-pass HHG experiment using the same driving laser and by around 2 orders of magnitude compared to intracavity HHG in a standard-approach EC.

In conclusion, we have studied experimentally and theoretically the nonlinear interaction of laser pulses with a gas target in a high-finesse EC. The improved measurement sensitivity allowed for the quantitative validation of a refined nonlinear interaction model in a large parameter range. The significance of this work is twofold. First, it establishes the combination of ECs with spatial-spectral interferometry as a highly sensitive measurement technique for nonlinear light-matter interactions in general. For instance, the methodology presented here can readily be applied to χ^3 nonlinearities in bulk dielectrics. Second, our experimentally validated *ab initio* model for the nonlinear cavity response can be used in conjunction with models for phase matching in HHG [28] to globally optimize the conversion efficiency to the XUV. We show that tailoring the spectral reflectivities of EC mirrors to exploit the spectral broadening induced by the intracavity nonlinearity is a viable route towards a dramatic increase in the peak power enhancement over standard-approach ECs. In particular, a temporal compression of the intracavity pulse down to the few-cycle regime can be reached for parameters typical for phase-matched HHG. This will enable intracavity HHG experiments at similar laser pulse and gas parameters as state-of-the-art single-pass setups [30] but at significantly higher repetition rates and XUV output powers. In addition, the precise control of intracavity nonlinearities together with the increased degree of ionization tolerated by such an EC offers the prospect of generating ultrabroadband frequency combs ranging from the mid to the far-infrared via THz generation in a photo-induced plasma [33].

The authors thank M. Ciappina, Th. Udem, and A. Apolonski for helpful discussions. This work was supported by the DFG Cluster of Excellence, Munich Centre for Advanced Photonics (MAP), by the BMBF project, Photonische Nanomaterialien (PhoNa), and by the MEGAS Fraunhofer-/Max-Planck-Gesellschaft cooperation.

*simon.holzberger@mpq.mpg.de

[1] A. Foltynowicz, P. Masłowski, A. J. Fleisher, B. J. Bjork, and J. Ye, Appl. Phys. B **110**, 163 (2013).

[2] I. Pupeza, X. Gu, E. Fill, T. Eidam, J. Limpert, A. Tünnermann, F. Krausz, and T. Udem, Opt. Express **18**, 26184 (2010).

[3] T. J. Hammond, A. K. Mills, and D. J. Jones, Opt. Express **17**, 8998 (2009).

[4] H. Carstens, N. Lilienfein, S. Holzberger, C. Jocher, T. Eidam, J. Limpert, A. Tünnermann, J. Weitenberg, D. C. Yost, A. Alghamdi, Z. Alahmed, A. Azzeer, A. Apolonski, E. Fill, F. Krausz, and I. Pupeza, Opt. Lett. **39**, 2595 (2014).

[5] C. Gohle, T. Udem, M. Herrmann, J. Rauschenberger, R. Holzwarth, H. A. Schuessler, F. Krausz, and T. W. Hänsch, Nature (London) **436**, 234 (2005).

[6] R. J. Jones, K. D. Moll, M. J. Thorpe, and J. Ye, Phys. Rev. Lett. **94**, 193201 (2005).

[7] A. Cingöz, D. C. Yost, T. K. Allison, A. Ruehl, M. E. Fermann, I. Hartl, and J. Ye, Nature (London) **482**, 68 (2012).

[8] C. Benko, T. K. Allison, A. Cingöz, L. Hua, F. Labaye, D. C. Yost, and J. Ye, Nat. Photonics **8**, 530 (2014).

[9] I. Pupeza, S. Holzberger, T. Eidam, H. Carstens, D. Esser, J. Weitenberg, P. Rußbüldt, J. Rauschenberger, J. Limpert, T. Udem, A. Tünnermann, T. W. Hänsch, A. Apolonski, F. Krausz, and E. Fill, Nat. Photonics **7**, 608 (2013).

[10] D. C. Yost, A. Cingöz, T. K. Allison, A. Ruehl, M. E. Fermann, I. Hartl, and J. Ye, Opt. Express **19**, 23483 (2011).

[11] T. K. Allison, A. Cingöz, D. C. Yost, and J. Ye, Phys. Rev. Lett. **107**, 183903 (2011).

[12] D. R. Carlson, J. Lee, J. Mongelli, E. M. Wright, and R. J. Jones, Opt. Lett. **36**, 2991 (2011).

[13] T. Eidam, F. Röser, O. Schmidt, J. Limpert, and A. Tünnermann, Appl. Phys. B **92**, 9 (2008).

[14] A. P. Kovács, K. Osvay, Z. Bor, and R. Szipöcs, Opt. Lett. **20**, 788 (1995).

[15] M. Geissler, G. Tempea, A. Scrinzi, M. Schnürer, F. Krausz, and T. Brabec, Phys. Rev. Lett. **83**, 2930 (1999).

[16] See Supplemental Material at http://link.aps.org/supplemental/10.1103/PhysRevLett.115.023902, which includes Refs. [17–24], for the validity of the 1D approach and the envelope approximation and detailed information on the modelling of the plasma decay.

[17] W. H. Press, *Numerical Recipes: The Art of Scientific Computing*, 3rd ed. (Cambridge University Press, Cambridge, 2007).

[18] B. Bernhardt, A. Ozawa, A. Vernaleken, I. Pupeza, J. Kaster, Y. Kobayashi, R. Holzwarth, E. Fill, F. Krausz, T. W. Hänsch, and T. Udem, Opt. Lett. **37**, 503 (2012).

[19] Y. B. Zeldovič, Y. P. Rajzer, and W. D. Hayes, *Physics of Shock Waves and High-Temperature Hydrodynamic Phenomena* (Dover Publication, Mineola and New York, 2002).

[20] E. P. Kanter, R. Santra, C. Höhr, E. R. Peterson, J. Rudati, D. A. Arms, E. M. Dufresne, R. W. Dunford, D. L. Ederer, B. Krässig, E. C. Landahl, S. H. Southworth, and L. Young, J. Appl. Phys. **104**, 073307 (2008).

[21] E. Hinnov and J. Hirschberg, Phys. Rev. **125**, 795 (1962).

[22] M. C. M. van de Sanden, J. M. de Regt, and D. C. Schram, Phys. Rev. E **47**, 2792 (1993).

[23] L. Allen, D. G. C. Jones, and D. G. Schofield, J. Opt. Soc. Am. **59**, 842 (1969).

[24] M. R. Bruce, W. B. Layne, C. A. Whitehead, and J. W. Keto, J. Chem. Phys. **92**, 2917 (1990).

[25] A. M. Perelomov, V. S. Popov, and M. V. Terent'ev, Zh. Eksp. Teor. Fiz. **50**, 1393 (1966) [Sov. Phys. JETP **23**, 924 (1966)].

[26] M. V. Ammosov, N. B. Delone, and V. P. Krainov, Zh. Eksp. Teor. Fiz. **91**, 2008 (1986) [Sov. Phys. JETP **64**, 1191 (1986)].

[27] G. L. Yudin and M. Y. Ivanov, Phys. Rev. A **64**, 013409 (2001).

[28] S. Kazamias, S. Daboussi, O. Guilbaud, K. Cassou, D. Ros, B. Cros, and G. Maynard, Phys. Rev. A **83**, 063405 (2011).

[29] K. D. Moll, R. J. Jones, and J. Ye, Opt. Express **13**, 1672 (2005).

[30] S. Hädrich, A. Klenke, J. Rothhardt, M. Krebs, A. Hoffmann, O. Pronin, V. Pervak, J. Limpert, and A. Tünnermann, Nat. Photonics **8**, 779 (2014).

[31] F. X. Kärtner, U. Morgner, R. Ell, T. Schibli, J. G. Fujimoto, E. P. Ippen, V. Scheuer, G. Angelow, and T. Tschudi, J. Opt. Soc. Am. B **18**, 882 (2001).

[32] V. Pervak, A. V. Tikhonravov, M. K. Trubetskov, S. Naumov, F. Krausz, and A. Apolonski, Appl. Phys. B **87**, 5 (2007).

[33] E. Matsubara, M. Nagai, and M. Ashida, J. Opt. Soc. Am. B **30**, 1627 (2013).

Supplemental Material to ”Femtosecond Enhancement Cavities in the Nonlinear Regime”

S. Holzberger,[1,2] N. Lilienfein,[1,2] H. Carstens,[1,2] T. Saule,[1,2] M. Högner,[1,2] F. Lücking,[2] M. Trubetskov,[1]
V. Pervak,[2] T. Eidam,[3] J. Limpert,[3] A. Tünnermann,[3] E. Fill,[1,2] F. Krausz,[1,2] and I. Pupeza[1,2]

[1]*Max-Planck-Institut für Quantenoptik, Hans-Kopfermann-Str. 1, 85748 Garching, Germany*
[2]*Ludwig-Maximilians-Universität München, Am Coulombwall 1, 85748 Garching, Germany*
[3]*Friedrich-Schiller-Universität Jena, Institut für Angewandte Physik, Albert-Einstein-Str. 15, 07745 Jena, Germany*

(Dated: June 26, 2015)

VALIDITY OF THE ENVELOPE APPROXIMATION

The original derivation of the envelope approximation given in Ref. [1] (see also Eq. (2) of the text) of the first-order propagation equation given in Ref. [2] was intended for highly multi-cycle pulses ($\frac{\omega_c}{2\pi}\tau \gg 1$) at moderate intensities, i.e., at low ionization levels. To justify its use in a broader parameter range, we solve both propagation equations using a fourth-order Runge-Kutta solver with initial parameters that are quite extreme compared to the currently reachable values in enhancement cavities. In particular, we use a 10-fs pulse with a peak intensity of $8 \times 10^{13}\,\mathrm{W/cm^2}$, propagated through a xenon gas target of $4 \times 10^{18}\,\mathrm{cm^{-3}}$ particle density. The propagation length is 1 cm which corresponds to 50 passes through a 200-µm long gas target. In the case of argon and neon the peak intensity is set to $2 \times 10^{14}\,\mathrm{W/cm^2}$ and $5.5 \times 10^{14}\,\mathrm{W/cm^2}$, respectively. Furthermore, Eq. (2) of the text is solved in step sizes of the actual gas target length, i.e., 200 µm as it is used in the cavity simulations. To get the full oscillatory fields in the envelope-based models, we interpolate the obtained complex envelope on a finer time grid and multiply it by the phase from the carrier ($e^{i\omega_c t}$). The results of the three approaches are shown in Fig. 1. The overall agreement is excellent. In the trailing part of the pulse, a small deviation of the envelope-based models can be seen, where the envelope approximation overestimates the losses.

VALIDITY OF THE 1D APPROACH

Due to the strong nonlinear nature of the ionization, the induced phase shifts and losses show a pronounced spatial dependence in the transverse coordinates after a single pass through the gas target. Therefore, it is important to specify the parameter range in which the 1D approximation as used in the text, can be applied. To this end, we simulate one pass through the gas target, once by employing the 1D model and once by solving the first-order propagation equation in 3+1 dimensions, and compare the resulting field distributions. Both simulations use the same peak intensity, pulse energy and time dependence of the incident pulse.

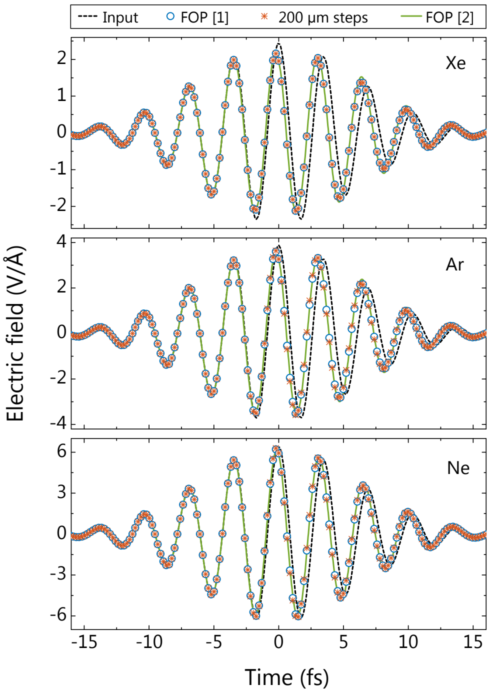

Figure 1. Nonlinear pulse propagation of a 10-fs pulse via the 1D first-order propagation equations (FOP) as given in Ref. [2] and in Ref. [1]. We also show the solution of the latter, when solved in step sizes of 200 µm. From upper to lower panel: input peak intensities of $8 \times 10^{13}\,\mathrm{W/cm^2}$, $2 \times 10^{14}\,\mathrm{W/cm^2}$, and $5.5 \times 10^{14}\,\mathrm{W/cm^2}$ in a xenon, argon, and neon gas target, respectively. The propagation distance was 1 cm and the particle density set to $4 \times 10^{18}\,\mathrm{cm^{-3}}$.

For the 4D simulation, we rely on the first-order propagation equation as derived in Ref. [2] under the assumption of the envelope approximation for the nonlinear polarization response as validated in the previous section. We take a split-step approach that calculates the propagation $z \to z + dz$ in the Fourier space (k_x, k_y, z, ω) and the nonlinear polarization response in real space and time (x, y, z, t). The numerical algorithm is based on a Predictor-Corrector method in combination with a

Crank-Nicolson scheme [3]. This permits to propagate in step sizes of 10 µm through an initially homogeneous gas target of neutral xenon atoms at a particle density of $4 \times 10^{18}\,\mathrm{cm}^{-3}$ and a total length of 200 µm. On a personal computer, the propagation takes about 15 s, which is fast when doing a few calculations. However, for investigating a wide parameter sweep requiring hundreds of complete cavity build-ups, a faster computational model is desirable.

To compare the results of the two models, we use the fact that the cavity acts as a spatial filter. Due to the Gouy phase the resonator can be tuned such that only the fundamental transverse mode $\mathrm{GH}_{0,0}$ is resonant in the cavity. Subsequent to the nonlinear propagation (index "n") through the gas target, we decompose the field distribution $\tilde{A}^{(\mathrm{n})}(x, y, \omega)$ at $z = z_0$ into the normalized transverse modes of the resonator without the gas target ($\mathrm{GH}_{i,j}(x, y, \omega)$). We proceed in the same manner for the case of linear propagation (index "ℓ"), i.e., without a gas target, yielding the field $\tilde{A}^{(\ell)}(x, y, \omega)$ at the same z-position. In the decomposition, we are mainly interested in the coefficient $c_{0,0}$ describing the field content in the fundamental transverse mode, that is calculated as

$$c_{0,0}^{(\mathrm{n},\ell)}(\omega) = \int_{-\infty}^{\infty}\int_{-\infty}^{\infty} \tilde{A}^{(\mathrm{n},\ell)}(x, y, \omega)\mathrm{GH}^{*}_{0,0}(x, y, \omega)dxdy.$$

The fundamental-mode-filtered version $\tilde{A}_{0,0}^{(\mathrm{n},\ell)}$ of the fields $\tilde{A}^{(\mathrm{n},\ell)}$ is then given by

$$\tilde{A}_{0,0}^{(\mathrm{n},\ell)}(x, y, \omega) = c_{0,0}^{(\mathrm{n,l})}(\omega)\mathrm{GH}_{0,0}(x, y, \omega).$$

Next, the corresponding fields in the time domain $A_{0,0}^{(\mathrm{n},\ell)}(x, y, t)$ are retrieved via inverse Fourier transformation. From these fields we can compute the temporal losses and the acquired temporal phase shift according to

$$\mathrm{Loss}(t) = 1 - \frac{\int_{-\infty}^{\infty}\int_{-\infty}^{\infty}\left|A_{0,0}^{(\mathrm{n})}(x, y, t)\right|^2 dxdy}{\int_{-\infty}^{\infty}\int_{-\infty}^{\infty}\left|A_{0,0}^{(\ell)}(x, y, t)\right|^2 dxdy} \tag{1}$$

$$\Theta(t) = \arg \left.\frac{A_{0,0}^{(\mathrm{n})}(x, y, t)}{A_{0,0}^{(\ell)}(x, y, t)}\right|_{x=0,y=0} \tag{2}$$

Note, that the x-y-dependency of the fields $A_{0,0}^{(\mathrm{n},\ell)}$ is an intrinsic attribute of Gaussian beams and is not linked to the plasma effects accounted for by $c_{0,0}^{(\mathrm{n})}(\omega)$. Therefore the relative phase shift has a negligible variation with respect to the transverse coordinates in the parameter range discussed here and we evaluate the phase shift on the optical axis.

In Fig. 2 we compare the overall losses and the total acquired phase shift calculated from Eq. (1) and (2) to the corresponding values of the 1D model of the text. It can be seen that the intensity at which a given phase shift is reached is quite similar. The 1D model, however, slightly overestimates the total phase shift. This is partially counterbalanced by the fact that the 1D model underestimates the losses, as it only accounts for the energy loss due to ionization of the gas target. For intensities up to $7 \times 10^{13}\,\mathrm{W/cm}^2$ the losses are dominated by the energy deposition in the target with a crossover at $8 \times 10^{13}\,\mathrm{W/cm}^2$. Therefore we believe that the 1D model is a valid approximation for intensities up to approximately $8 \times 10^{13}\,\mathrm{W/cm}^2$. The transverse effects of a (pre-existiting) steady-state plasma can in principle be treated similarly. However, this would require detailed calculations about the spatially-resolved plasma dynamics considering also the continuous flow of gas from the nozzle orifice. As an estimate of the order of magnitude of this effect, we calculate the losses for a non-ionizing pulse directly following the ionizing pulse. It turns out that the transfer of energy in higher-order modes of such a non-ionizing pulse is about a factor of two higher than the losses due to this coupling for the ionizing pulse. The actual losses resulting from the partially decayed plasma are on the same order of magnitude as the "direct" losses into higher-order modes.

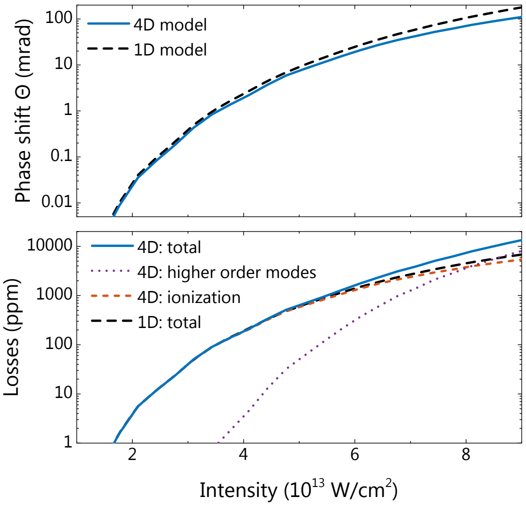

Figure 2. Comparison of a single pass through a xenon gas target in the 1D approach to the model in 3+1 dimensions for a range of intensities. Pulse duration: 30 fs. Upper panel: acquired temporal phase shift Θ at the end of the pulse. Lower panel: Losses due to energy transfer to higher-order modes during the ionization, due to ionization and resulting total losses. In addition, we plot the losses in the 1D model.

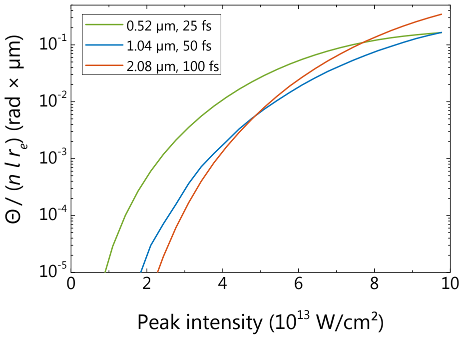

Figure 3. Single-pass phase shift Θ acquired as a function of the intensity for three different carrier wavelengths and pulse durations (but equal number of field oscillations) in a xenon gas target. At identical gas parameters and for most intensities shorter driving wavelengths are disadvantageous for reaching higher intensities.

WAVELENGTH SCALING

In Fig. 3, we plot the total acquired single-pass phase shift $\Theta = r_e \lambda_c \, \eta(t = \infty) nl$ for three different carrier wavelengths λ_c as a function of peak intensity. To keep the number of field oscillations constant, we scale the pulse durations accordingly. While Θ has an explicit linear dependence on λ_c, the ionized fraction η also depends strongly on λ_c. In terms of scaling the cut-off wavelength a 2-µm based system would outperform the 1-µm system up to intensities of about $5 \times 10^{13}\,\mathrm{W/cm^2}$, as it acquires less phase shift and allows for quadratically higher cut-off energies: $E_{\mathrm{cut-off}} = I_p + 3.17 U_p(\lambda)$. Furthermore, in an enhancement cavity seeded with frequency-doubled infrared light, the intensity clamping should be much more pronounced. This is confirmed by the reported peak intensity of about $1.2 \times 10^{13}\,\mathrm{W/cm^2}$ in Ref. [4]. In turn, at the clamping limit, i.e., for a given single-pass phase shift, a short-wavelength-seeded enhancement cavity works at much higher ionization levels, which might be beneficial for some applications.

PLASMA DECAY

Given the strong intensity dependence of the ionization rate, the region of potential ionization is significantly smaller than the $1/e^2$-intensity radius w_0 of the focus (here: $w_0 \approx 25\,\mu\mathrm{m}$ and $r_{\mathrm{ionization}} \sim 0.4 w_0$). With the values stated in the text, a fraction of about 15% of the ionized atoms leaves the region of ionization ($2r_{\mathrm{ionization}}$) within one cavity round-trip time.

For electron densities exceeding $10^{14}\,\mathrm{cm^{-3}}$ and electron temperatures on the order of $k_B T \sim 1\,\mathrm{eV}$, the dominant mechanism of electron-ion recombination is via three-body collisions [5]. When neglecting plasma expansion on the time scale of a cavity round-trip [6], the evolution of the electron density is governed by:

$$\frac{dn_e(t)}{dt} = -b n_e^3 \quad \text{with} \quad b = \hat{b}\,\frac{10^{-27}}{(k_B T)^{9/2}}\,\frac{\mathrm{cm^6\,eV^{9/2}}}{\mathrm{s}}. \tag{3}$$

Literature values for $\hat{b}$ vary from ~ 1 to 9 [5, 7, 8]. We assume an intermediate value of $\hat{b} = 2$. Plasma heating due to the recombination and cooling due to the expansion are neglected. At intensities of up to $\sim 5 \times 10^{13}\,\mathrm{W/cm^2}$ and our repetition rate (78 MHz), the model predicts the steady-state plasma density to be below $1 \times 10^{17}\,\mathrm{cm^{-3}}$. Thus, the higher-order dispersion plays a negligible role ($|\mathrm{GDD}| < 0.04\,\mathrm{fs^2}$ for $200\,\mu\mathrm{m}$, at $n_e = 1 \times 10^{17}\,\mathrm{cm^{-3}}$), which also renders a direct measurement via the higher-order dispersion very challenging. However, complementary measurements of the optimal offset frequency of the cavity corroborate the stated upper boundary in plasma density (not shown). The dominant effect of the steady-state plasma is a global shift of the cavity resonances and a change in the effective cavity length. As the depletion of the neutral gas is only a few percent, the influence on the clamping intensity is negligible. At these densities and for electron temperatures of $\sim 1\,\mathrm{eV}$ calculated with a classical model, we find with Eq. (3) that a fraction of about 30 % of the electrons recombines within the first cavity round-trip time.

Despite the strong temperature dependence of the recombination coefficient b, the emerging steady-state electron density is rather robust against variations in T. Underestimating the electron temperature T in the model leads to a much faster recombination time and thus an even lower steady-state ionized fraction. An overestimation of the electron temperature would mean a much slower recombination rate, however, the n_e^3 dependence of the recombination counteracts the resulting increase in electron density. Furthermore, the error is bound by the timescale set by the replenishment of the plasma in the interaction region with neutral atoms. For the same reasons, uncertainties in $\hat{b}$ have a minor influence on the steady-state ionized fraction and a negligible influence on the clamping intensity (see also next section).

SCALING OF THE REPETITION RATE

A way of increasing the XUV flux not restricted by the intensity clamping is the use of a higher-repetition-rate laser system. This is, however, only viable as long as the steady-state plasma has a tolerable influence on both the phase matching of the conversion process and the robustness of the stabilization system [9]. Furthermore, the exact value of $\hat{b}$ entering the recombination rate (see Eq. (3)) has only a minor influence on the steady-state ioniza-

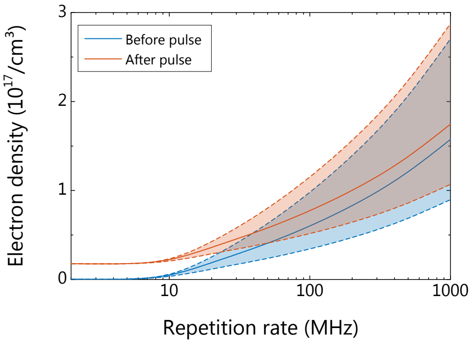

Figure 4. Electronic density before and after the pulse (solid lines) as a function of the repetition rate, keeping other parameters constant (in particular, pulse energy and peak intensity). Xe density: $4 \times 10^{18}\,\mathrm{cm}^{-3}$, target length 200 µm, intensity: $4.3 \times 10^{13}\,\mathrm{W/cm}^2$, focus radius: 30 µm. The dashed lines bounding the shaded areas were calculated assuming a five times higher or lower value of $\hat{b}$ in the recombination rate.

tion: a change in $\hat{b}$ by a factor of five results in a change of the steady-state fraction by only $\sim 50\,\%$ (see dashed lines vs. solid line in Fig. 4). Our model of the recombination process assumes that the electron capture directly populates the ground state of the atoms, a simplification that is only valid for sufficiently long cavity round-trip times, and high electron temperatures [10, 11]. Hence, at very high repetition rates a population of neutral but excited atoms might qualitatively change the cavity performance and the efficiency of the conversion process.

---

[1] T. K. Allison, A. Cingöz, D. C. Yost, and J. Ye, Phys. Rev. Lett. **107**, 183903 (2011).

[2] M. Geissler, G. Tempea, A. Scrinzi, M. Schnürer, F. Krausz, and T. Brabec, Phys. Rev. Lett. **83**, 2930 (1999).

[3] W. H. Press, *Numerical recipes: The art of scientific computing*, 3rd ed. (Cambridge Univ. Press, Cambridge, 2007).

[4] B. Bernhardt, A. Ozawa, A. Vernaleken, I. Pupeza, J. Kaster, Y. Kobayashi, R. Holzwarth, E. Fill, F. Krausz, T. W. Hänsch, and T. Udem, Opt. Lett. **37**, 503 (2012).

[5] Y. B. Zeldovič, Y. P. Rajzer, and W. D. Hayes, *Physics of shock waves and high-temperature hydrodynamic phenomena* (Dover Publ, Mineola and NY, 2002).

[6] E. P. Kanter, R. Santra, C. Höhr, E. R. Peterson, J. Rudati, D. A. Arms, E. M. Dufresne, R. W. Dunford, D. L. Ederer, B. Krässig, E. C. Landahl, S. H. Southworth, and L. Young, J. Appl. Phys. **104**, 073307 (2008).

[7] E. Hinnov and J. Hirschberg, Phys. Rev. **125**, 795 (1962).

[8] M. C. M. van de Sanden, J. M. de Regt, and D. C. Schram, Phys. Rev. E **47**, 2792 (1993).

[9] D. C. Yost, A. Cingöz, T. K. Allison, A. Ruehl, M. E. Fermann, I. Hartl, and J. Ye, Opt. Express **19**, 23483 (2011).

[10] L. Allen, D. G. C. Jones, and D. G. Schofield, J. Opt. Soc. Am. **59**, 842 (1969).

[11] M. R. Bruce, W. B. Layne, C. A. Whitehead, and J. W. Keto, J. Chem. Phys. **92**, 2917 (1990).

Chapter 7

Enhancement cavities for zero-offset-frequency pulse trains

by

Simon Holzberger, Nikolai Lilienfein, Michael Trubetskov, Henning Carstens,
Fabian Lücking, Vladimir Pervak, Ferenc Krausz and Ioachim Pupeza

published in

Optics Letters (2015)
DOI: 10.1364/OL.40.00216

Reprinted from [113]
with permission from the Optical Society of America.

Contributions

I conceived the experiment together with S.H. and I.P., and performed the experiments together with S.H.. I contributed to the data analysis and the manuscript.

May 15, 2015 / Vol. 40, No. 10 / OPTICS LETTERS 2165

Enhancement cavities for zero-offset-frequency pulse trains

S. Holzberger,[1,2,*] N. Lilienfein,[1,2] M. Trubetskov,[1] H. Carstens,[1,2] F. Lücking,[2] V. Pervak,[2] F. Krausz,[1,2] and I. Pupeza[1,2]

[1] *Max-Planck-Institut für Quantenoptik, Hans-Kopfermann-Str. 1, Garching 85748, Germany*

[2] *Ludwig-Maximilians-Universität München, Am Coulombwall 1, Garching 85748, Germany*

**Corresponding author: simon.holzberger@mpq.mpg.de*

Received March 24, 2015; accepted April 14, 2015;
posted April 16, 2015 (Doc. ID 236663); published May 4, 2015

The optimal enhancement of broadband optical pulses in a passive resonator requires a seeding pulse train with a specific carrier-envelope-offset frequency. Here, we control the phase of the cavity mirrors to tune the offset frequency for which a given comb is optimally enhanced. This enables the enhancement of a zero-offset-frequency train of sub-30-fs pulses to multi-kW average powers. The combination of pulse duration, power, and zero phase slip constitutes a crucial step toward the generation of attosecond pulses at multi-10-MHz repetition rates. In addition, this control affords the enhancement of pulses generated by difference-frequency mixing, e.g., for mid-infrared spectroscopy.

OCIS codes: (140.4780) Optical resonators; (140.7240) UV, EUV, and X-ray lasers; (300.6340) Spectroscopy, infrared.
http://dx.doi.org/10.1364/OL.40.002165

In a broadband, passive optical resonator, also referred to as enhancement cavity (EC), the ultrashort pulses emitted by a mode-locked laser can be coherently overlapped. If the losses and the phase distortions upon a round-trip inside the EC are low, the steady-state intracavity power can exceed the input power by several orders of magnitude, offering unique advantages for a multitude of applications. Most prominently, ECs have been used to build multi-MHz-repetition-rate sources of coherent extreme-ultra-violet (XUV) radiation by driving high-order harmonic generation (HHG) with kW-average-power-level femtosecond pulses in an intracavity gas target [1–4]. Recently, broadband ECs became relevant to infrared spectroscopy of diluted gases and aerosols. Here, the sensitivity is dramatically improved via resonant enhancement, increasing the effective absorption path length to several kilometers [5–7].

For a given seeding spectrum, a broadband EC dictates the pulse-to-pulse time delay τ and the pulse-to-pulse carrier-to-envelope phase (CEP) slip $\Delta\phi_{\mathrm{cep}}$. An optimum of the enhancement (e.g., for maximizing the intracavity power) is achieved if the seeding pulse train matches both these parameters. In the frequency domain, the pulse train corresponds to a comb of equidistant spectral lines spaced by the pulse repetition frequency $\omega_{\mathrm{rep}}/2\pi = 1/\tau$ and offset from zero by the carrier-envelope offset frequency $\omega_{\mathrm{ceo}} = -(\Delta\phi_{\mathrm{cep}}/2\pi)\omega_{\mathrm{rep}}$ [8,9]. Thus, for a given EC, input spectrum, and optimization criterion, there is an optimal pair of comb parameters, in particular an *optimal offset frequency* (OOF) [5,9,10].

Typically, the parameter ω_{ceo} of the seeding laser is adjusted to fit the OOF dictated by the EC. Some applications, however, require the intracavity pulse to remain unchanged (up to the sign) from round-trip to round-trip, i.e., the phase slip $\Delta\phi_{\mathrm{cep}}$ must be an integer multiple of 2π (or π), corresponding to a comb with zero-offset-frequency (or $\omega_{\mathrm{rep}}/2$). An example is the generation of trains of XUV attosecond pulses or even of isolated attosecond pulses [11], for which zero-slip ECs that simultaneously support short and powerful pulses are a prerequisite. Another example is the enhancement of frequency combs generated via difference-frequency mixing of spectral components originating from the same comb, a process that intrinsically sets ω_{ceo} to zero [6]. Thus, the ability to tune the OOF of a broadband EC is highly desirable and would greatly benefit high-repetition-rate spectroscopic schemes ranging from XUV photoelectron spectroscopy [12] to mid-infrared vibrational spectroscopy [6,7].

In this Letter, we demonstrate the control of the OOF for the enhancement of broadband pulses by employing mirrors with controlled CEP shift upon reflection. This is achieved without sacrificing any other critical parameter, such as high reflectivity, close-to-zero group-delay dispersion (GDD) over a large bandwidth, or high damage threshold. Seeding the EC with nonlinearly broadened and compressed pulses from an Yb-based laser system allows for the enhancement of a zero-offset-frequency pulse train of sub-30-fs pulses to multi-kW-level average powers, limited only by the seed source. Furthermore, our results establish ECs as a simple yet powerful tool to determine the CEP shift imposed on the pulse upon propagation or reflection.

In the steady state and in the absence of any nonlinear medium in the resonator, the electric field of the circulating pulse E_{cav} at the input coupler can be related to the input field E_{in} by the following equation [13]:

$$E_{\mathrm{cav}}(\omega) = \frac{\sqrt{T(\omega)}}{1 - \sqrt{R(\omega)A(\omega)}e^{i\phi(\omega)}}E_{\mathrm{in}}(\omega). \tag{1}$$

Here, we assumed an input coupler of transmission $T(\omega)$ and reflectivity $R(\omega)$. Losses inside the resonator are accounted for by the round-trip power attenuation $A(\omega)$. The spectral phase $\phi(\omega)$ incorporates all phase shifts accumulated upon a round-trip, including those upon reflections from mirrors, transmission through dispersive materials, and geometric phase shifts due to focusing [13]. Maximal power enhancement is reached at frequencies where the round-trip phase equals a multiple of 2π [see Eq. (1)]. In the presence of GDD, the round-trip phase is not strictly linear in frequency, resulting in varying distances between successive resonances.

In contrast, all spectral lines ω_n of a frequency comb are linear in frequency and given by $\omega_n = n\omega_{\mathrm{rep}} + \omega_{\mathrm{ceo}}$. When coupled to an EC, both comb parameters are adjusted to best fit the equidistant comb to the cavity resonances. For input spectra over which the round-trip phase is sufficiently linear, there is a clear optimum in terms of integrated power enhancement and intracavity pulse duration with respect to ω_{ceo} and ω_{rep}. Although the concept of an OOF is well known [3,5,9,10], control of this parameter has not been reported so far.

In the following, we deduce the round-trip phase slip $\Delta\phi_{\mathrm{cep}}$ experienced by an intracavity pulse given a round-trip phase $\phi(\omega)$ and a laser spectrum $I(\omega)$ [see Fig. 1(a)]. Terms in $\phi(\omega)$ that are proportional to ω merely delay the pulse. Thus, the ϕ-intercept of a linear fit in ω to $\phi(\omega)$ with weights according to the pulse spectrum constitutes the induced phase slip $\Delta\phi_{\mathrm{cep}}$, while the slope represents the group delay τ. Optimal enhancement in this resonator requires a seeding comb with the repetition rate $\omega^*_{\mathrm{rep}} = 2\pi/\tau$ and the offset frequency $\omega^*_{\mathrm{ceo}} = -(\Delta\phi_{\mathrm{cep}}/2\pi)\omega^*_{\mathrm{rep}}$. Hence, we identify the fitted straight line given by $2\pi(\omega - \omega^*_{\mathrm{ceo}})/\omega^*_{\mathrm{rep}}$ with the optimal frequency comb. As the phase is only sampled at the comb lines $\omega_n = n\omega^*_{\mathrm{rep}} + \omega^*_{\mathrm{ceo}}$, the straight line reduces to a series of multiples of 2π. Thus, when evaluating the frequency-resolved power enhancement via Eq. (1), $\phi(\omega_n)$ is equivalent to its deviation from the fit.

One can expand this graphical phase analysis to explain the characteristic shapes of the spectral power enhancement in the case of too high or too low offset frequency of the seeding comb [see Fig. 1(a)]. When sweeping the comb offset frequency while keeping the central region of the input spectrum on resonance—e.g., by deriving the error signal for the locking electronics in that spectral part—the integrated power enhancement traces out a curve with a clear maximum [3,10].

Tuning the phase curve to achieve a desired value of $\Delta\phi_{\mathrm{cep}}$ is possible by manipulating three different contributions to $\phi(\omega)$. First, varying the focusing geometry of the resonator directly changes the Gouy phase $\phi_{n,m} = (m + 1/2)\psi_{\mathrm{tan}} + (n + 1/2)\psi_{\mathrm{sag}}$, which a transverse Gauss–Hermite mode of order n, m acquires per round-trip (in the tangential and sagittal plane, respectively). Here, the Gouy parameters ψ are derived using the *ABCD*-matrix of the resonator according to $\psi = \mathrm{sgn}(B)\arccos[(A + D)/2]$ [13,14]. In spite of the advantage of being continuously adjustable over a large range, in most experiments, the Gouy phase is of limited variability as it is directly linked to the cavity mode size.

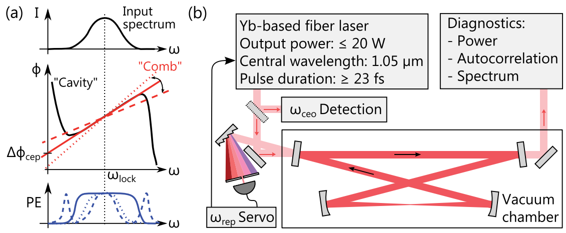

Fig. 1. (a) Upper panel: input power spectrum. Center panel: sketch of the single-round-trip phase $\phi(\omega)$ and of the resulting pulse-to-pulse phase slip $\Delta\phi_{\mathrm{cep}}$. Dashed and dotted lines indicate input comb with too high or too low offset frequency. Lower panel: corresponding spectral power enhancement (PE) in the three cases. (b) Experimental setup.

Second, inserting a transparent material with a refractive index $n(\omega)$ in the resonator, adds $\omega\tau[n(\omega) - 1]$ to the phase curve. In principle, this can even be done without adding higher-order dispersion, e.g., if a material with an index of refraction according to $n(\omega) = c_1 + c_2/\omega$ with two constants c_1, c_2 is employed. In practice, this is difficult to achieve and is likely to be in conflict with other experimental requirements, such as high vacuum, high damage threshold, polarization insensitivity, or low losses and, thus, limits its usability.

Third, as shown here, the phase upon reflection off the cavity mirrors can be tailored without altering higher order dispersion terms. In this study, we employ coating designs based on quarter-wave stacks, which are widely used as highly reflecting mirrors in ECs. They provide low dispersion at a manageable design complexity and exhibit high damage thresholds. To maximize the bandwidth of the coatings, $\mathrm{Nb_2O_5}$ and $\mathrm{SiO_2}$ are chosen as coating materials due to their large contrast in the refractive indices [15]. The topmost layers of the coating deviate from quarter-wave thicknesses and serve as phase correctors. Besides increasing the spectral width of GDD $< 0.5\ \mathrm{fs}^2$ to 96 nm, this opens the possibility to vary the phase slip imprinted on the pulse upon reflection. For the experiment, we implemented two different designs named *A* and *B*, differing in $\Delta\phi_{\mathrm{cep}}$. A systematic study of the design optimization for a target value for $\Delta\phi_{\mathrm{cep}}$ exceeds the scope of this Letter.

The experimental setup is sketched in Fig. 1(b). The pulses are generated by the laser system described in [16], delivering 180-fs pulses at a repetition rate of 77 MHz, centered at a wavelength of 1045 nm. Subsequent spectral broadening in a photonic-crystal fiber and compression using chirped mirrors yields close-to-Fourier-limited pulses of 28 fs at a maximum output power of 20 W. The comb offset frequency of the oscillator is freely running with a typical linewidth of ~50 kHz, monitored using an *f*–2*f* interferometer. Slow drifts in the offset frequency appearing on the time scale of several minutes are manually compensated by a pair of intra-oscillator wedges. The EC is implemented in a bow-tie configuration equipped with an input coupler with 1% transmission dominating the cavity losses. Due to geometric constraints of the vacuum chamber, a minimum of six cavity mirrors is required in the experiment, although less cavity mirrors would increase the supported bandwidth. If not stated otherwise, the cavity is operated close to the inner edge of the stability range, ensuring nearly identical spot sizes on all mirrors.

We determined the OOF of a cavity configuration by recording the steady-state power enhancement while locking the repetition rate of the input laser to the cavity for different comb offset frequencies. Figure 2(a) demonstrates the tunability of the OOF of a broadband EC by controlling the phase of the highly reflecting cavity mirrors. To this end, we measured the OOF of the EC while

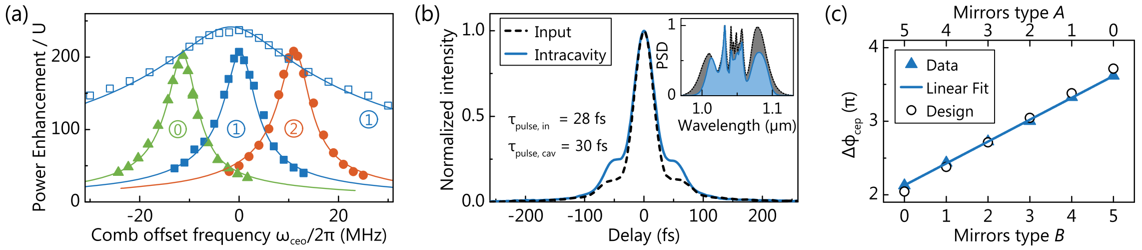

Fig. 2. (a) Power enhancement corrected for the spatial overlap (U) vs. offset frequency of the seeding comb for a cavity employing 0, 1, or 2 mirrors of type *B* (indicated by the numbers). Solid symbols: broadband input pulses. Open symbols: input pulses of reduced bandwidth, illustrating the dependence of the OOF on the spectrum. Solid lines: corresponding model results. (b) Intensity autocorrelation trace of the pulses in case of optimal comb parameters. Inset: corresponding normalized power spectral density (PSD) with 100-nm intracavity bandwidth at −10 dB. (c) Retrieved CEP-shift upon reflection off five cavity mirrors and calculated values from the coating design.

stepwise replacing cavity mirrors of type *A* by mirrors of type *B*. A constant shift of the OOF is observed, in particular reaching zero, when only one mirror of type *B* was employed. For all mirror combinations, a power enhancement of more than 200 was reached with optimal comb parameters. Here, the FWHM of the intensity autocorrelation of the intracavity pulse was measured to be 43 fs, corresponding to a pulse duration of 30 fs assuming a deconvolution factor of 1.41 [see Fig. 2(b)]. Repeating the measurement of the OOF with pulses of a reduced spectral width of ~8 nm confirms that the sensitivity of the cavity to the comb offset frequency strongly depends on the bandwidth of the pulses. The necessary precision in controlling the round-trip phase and the seeding laser phase noise scales with the bandwidth and with the finesse.

To quantify the CEP slip imprinted upon reflection off a single mirror, we inserted two supplementary mirrors and measured the change in OOF for three combinations of the additional mirrors. The retrieved phase slip of a mirror of type *A* was 1.34 rad, and 2.25 rad in case of type *B*. Both differ by less than 80 mrad from their design values. To proove the reproducibility of our approach, i.e., that all mirrors from one coating run (*A* or *B*) are identical, we plot the measured phase differences and the expected ones in Fig. 2(c). The excellent linear fit to the data, which is also in good agreement with the calculated values, clearly validates the reproducibility.

In Fig. 3(a), the phase slip introduced by Gaussian beam propagation through free space is shown. By stepwise increasing the separation between the curved mirrors, we varied the position of the EC in the stability range and, thus, the Gouy parameter. For each cavity geometry we recorded the OOF. The experimental results excellently agree with theory. If the cavity mode size is not a critical parameter, the Gouy phase constitutes an option to fine-tune the OOF.

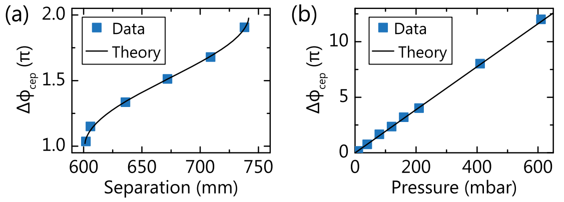

Fig. 3. Dependence of the optimal pulse-to-pulse phase slip $\Delta\phi_{\mathrm{cep}}$ on (a) the resonator geometry by varying the separation between the curved mirrors (radius of curvature: −600 mm) and (b) on the argon pressure in the chamber. In (b), input pulses of ~8 nm bandwidth were used to avoid spectral narrowing. A global offset was added to the data.

In Fig. 3(b), the dependence of the phase slip on the gas dispersion is plotted. By gradually introducing argon gas in the vacuum chamber one can widely tune the OOF. However, the higher order dispersion terms also lead to spectral narrowing of the intracavity spectrum. In the case of broadband, 30-fs pulses and for our finesse, about 0.1 fs^2 of additional GDD is tolerable without sacrificing the intracavity pulse duration. Given the dispersion of argon, this transfers to about 3 mbar of tolerable gas pressure and thus a maximal shift in $\Delta\phi_{\mathrm{cep}}$ of about 0.06π. Similarily, the insertion of, e.g., a pair of thin sapphire wedges (<4 μm), is tolerable and would allow for a phase tunability of 0.15π. A robust implementation of such a thin wedge was demonstrated by optically contacting it to a mirror [17].

Using the full input power of the laser, the intracavity power surpassed 3 kW with 30-fs intracavity pulses. Shorter input pulses resulting from stronger nonlinear broadening in the fiber led to slightly shorter intracavity pulses, however at significantly reduced power enhancement. Employing an input coupler with a transmission of 3%, we obtained sub-25-fs pulses at average powers exceeding 1 kW, limited by the power of the seed source. The damage threshold of the mirror coating was determined to be on the order of $1 \times 10^{11}\ \mathrm{W\,cm^{-2}}$ using a spot size of 200 μm at pulse durations of 30 fs. The RMS stability of the intracavity power was typically better than 0.25% in the range from 2.5 Hz to 5 MHz, limited by the free-running offset frequency of the laser.

In conclusion, we have designed, produced, and characterized low-loss, broadband mirrors that shift the CEP of a pulse upon reflection in a controlled way. To the best of our knowledge, this is the first demonstration of the control over this degree of freedom of the mirror phase. Using these phase-controlled mirrors, we operated a high-finesse, non-polarization-discriminating EC that supports pulses of 30 fs at a power enhancement of 200, with vanishing pulse-to-pulse phase slip. Through careful design, neither the bandwidth nor the damage threshold of the mirrors is compromised by the additional "control knob." We showed that nonlinearly broadened and compressed Yb-based master-oscillator-power-amplifier systems are a viable route for reaching multi-kW level pulses of sub-30-fs duration.

With state-of-the art high-power laser systems and thermally robust cavity geometries with even larger mode radii [18], scaling the intracavity power by at least one order of magnitude at similar pulse durations seems straightforward. A further increase of the cavity bandwidth should be feasible by using mirrors with complementary phase characteristics. When equipped with an XUV output coupler as shown in [4], our setup enables the generation of XUV attosecond pulse trains at multi-MHz repetition rates. In addition, for the first time, these pulse parameters and the polarization insensitivity fulfill the prerequisites for the generation of isolated attosecond pulses in ECs via gating mechanisms restricting the XUV emission process to a single event per driving pulse [19,20].

We thank the fiber laser group at the Institute of Applied Physics at Friedrich-Schiller-University Jena for providing the laser system. We acknowledge financial support by the DFG Cluster of Excellence, Munich Centre for Advanced Photonics (MAP) and by the MEGAS Fraunhofer-/Max-Planck-Gesellschaft cooperation. IP acknowledges funding by the European Research Council under grant agreement no. [617173] ACOPS.

References

1. C. Gohle, T. Udem, M. Herrmann, J. Rauschenberger, R. Holzwarth, H. A. Schuessler, F. Krausz, and T. W. Hänsch, Nature **436**, 234 (2005).
2. A. Cingöz, D. C. Yost, T. K. Allison, A. Ruehl, M. E. Fermann, I. Hartl, and J. Ye, Nature **482**, 68 (2012).
3. A. K. Mills, T. J. Hammond, M. H. C. Lam, and D. J. Jones, J. Phys. B **45**, 142001 (2012).
4. I. Pupeza, S. Holzberger, T. Eidam, H. Carstens, D. Esser, J. Weitenberg, P. Rußbüldt, J. Rauschenberger, J. Limpert, T. Udem, A. Tünnermann, T. W. Hänsch, A. Apolonski, F. Krausz, and E. Fill, Nat. Photonics **7**, 608 (2013).
5. F. Adler, M. J. Thorpe, K. C. Cossel, and J. Ye, Annu. Rev. Anal. Chem. **3**, 175 (2010).
6. A. Schliesser, N. Picqué, and T. W. Hänsch, Nat. Photonics **6**, 440 (2012).
7. A. Foltynowicz, P. Masłowski, A. J. Fleisher, B. J. Bjork, and J. Ye, Appl. Phys. B **110**, 163 (2013).
8. S. T. Cundiff, J. Phys. D **35**, R43 (2002).
9. L. Arissian and J. C. Diels, J. Phys. B **42**, 183001 (2009).
10. A. Schliesser, C. Gohle, T. Udem, and T. W. Hänsch, Opt. Express **14**, 5975 (2006).
11. F. Krausz and M. Ivanov, Rev. Mod. Phys. **81**, 163 (2009).
12. A. Stolow, A. E. Bragg, and D. M. Neumark, Chem. Rev. **104**, 1719 (2004).
13. A. E. Siegman, *Lasers* (University Science Books, 1986).
14. J. Weitenberg, P. Rußbüldt, I. Pupeza, T. Udem, H.-D. Hoffmann, and R. Poprawe, J. Opt. **17**, 025609 (2015).
15. S. A. Furman and A. V. Tichonravov, *Basics of Optics of Multilayer Systems* (Editions Frontières, 1992).
16. T. Eidam, F. Röser, O. Schmidt, J. Limpert, and A. Tünnermann, Appl. Phys. B **92**, 9 (2008).
17. I. Pupeza, E. E. Fill, and F. Krausz, Opt. Express **19**, 12108 (2011).
18. H. Carstens, N. Lilienfein, S. Holzberger, C. Jocher, T. Eidam, J. Limpert, A. Tünnermann, J. Weitenberg, D. C. Yost, A. Alghamdi, Z. Alahmed, A. Azzeer, A. Apolonski, E. Fill, F. Krausz, and I. Pupeza, Opt. Lett. **39**, 2595 (2014).
19. P. Tzallas, E. Skantzakis, C. Kalpouzos, E. P. Benis, G. D. Tsakiris, and D. Charalambidis, Nat. Phys. **3**, 846 (2007).
20. X. Feng, S. Gilbertson, H. Mashiko, H. Wang, S. D. Khan, M. Chini, Y. Wu, K. Zhao, and Z. Chang, Phys. Rev. Lett. **103**, 183901 (2009).

Chapter 8

Enhancement cavities for few-cycle pulses

by

Nikolai Lilienfein, Christina Hofer, Simon Holzberger, Christoph Matzer,
Peter Zimmermann, Michael Trubetskov, Vladimir Pervak and Ioachim Pupeza

published in

Optics Letters (2017)
DOI: 10.1364/OL.42.000271

Reprinted from [116]
with permission from the Optical Society of America.

Contributions

I conceived the experiment together with S.H. and I.P., and performed the experiment together with C.H.. I analyzed the data with C.H., and wrote most of the manuscript.

Letter Vol. 42, No. 2 / January 15 2017 / *Optics Letters* 271

Optics Letters

Enhancement cavities for few-cycle pulses

N. Lilienfein,[1,2,*] C. Hofer,[1,3] S. Holzberger,[1,4] C. Matzer,[5] P. Zimmermann,[5] M. Trubetskov,[1] V. Pervak,[2] and I. Pupeza[1]

[1]*Max-Planck-Institut für Quantenoptik, Hans-Kopfermann-Strasse 1, 85748 Garching, Germany*
[2]*Ludwig-Maximilians-Universität München, Am Coulombwall 1, 85748 Garching, Germany*
[3]*Technische Universität München, James-Franck-Str. 1, 85748 Garching, Germany*
[4]*Present address: Menlo Systems GmbH, Am Klopferspitz 19a, 82152 Martinsried, Germany*
[5]*Layertec GmbH, Ernst-Abbe-Weg 1, 99441 Mellingen, Germany*
**Corresponding author: nikolai.lilienfein@mpq.mpg.de*

Received 28 October 2016; revised 9 December 2016; accepted 9 December 2016; posted 9 December 2016 (Doc. ID 279669); published 11 January 2017

We address the challenge of increasing the bandwidth of high-finesse femtosecond enhancement cavities and demonstrate a broad spectrum spanning 1800 cm^{-1} (195 nm) at −10 dB around a central wavelength of 1050 nm in an EC with an average finesse exceeding 300. This will benefit a host of spectroscopic applications, including transient absorption spectroscopy, direct frequency comb spectroscopy, and Raman spectroscopy. The pulse circulating in the EC is composed of only 5.4 optical cycles, at a kilowatt-level average power. Together with a suitable gating technique, this paves the way to the efficient generation of multi-megahertz-repetition-rate isolated extreme ultraviolet attosecond pulses via intracavity high-order harmonic generation.

OCIS codes: (140.4780) Optical resonators; (320.0320) Ultrafast optics; (310.1620) Interference coatings; (140.7240) UV, EUV, and X-ray lasers; (300.6340) Spectroscopy, infrared.

https://doi.org/10.1364/OL.42.000271

Owing to their unique properties, passive optical resonators, or enhancement cavities (ECs), have leveraged a number of breakthrough achievements in spectroscopy. First, the path length enhancement for the interaction with a weakly absorbing sample provided by ECs has enabled sensing techniques with unparalleled sensitivity [1,2]. Second, in state-of-the-art ECs, broadband optical frequency combs or, equivalently, the ultrashort pulses produced by frequency-stabilized mode-locked lasers, can be enhanced in power by a few orders of magnitude. In addition to boosting the sensitivity of broadband (transient) absorption spectroscopy [3–7], this affords intensities high enough to drive nonlinear processes such as high-harmonic generation (HHG) at multi-megahertz repetition rates [8–14]. Recently, this has enabled the extension of direct frequency comb spectroscopy to the vacuum ultraviolet [10,11] and the demonstration of the feasibility of extreme ultraviolet frequency combs with photon energies exceeding 100 eV [12,14]. Finally, by detuning the input frequency comb with respect to the longitudinal modes of a high-finesse EC, individual comb lines can be resolved via spectral filtering, leading to the highest frequency resolution achievable in broadband spectroscopy so far [15–17].

The sensitivity enhancement underlying the success of ECs in spectroscopy applies not only to absorption, but also to the spectral phase [18]. In combination with the spectral phase the curvature inherent to standard dielectric multilayer mirrors, this sensitivity limits the optical bandwidth of ECs. The broadest bandwidths of ECs reported hitherto in literature amount to 60 nm at a central wavelength of 800 nm [8], and to 100 nm at a central wavelength of 1050 nm [19], both demonstrated in ECs with a finesse of about 300. Significantly extending the spectral coverage and shortening the pulse duration in femtosecond ECs would tremendously benefit existing applications and enable novel ones. For instance, cavity-enhanced Raman spectroscopy, which so far has only been demonstrated in narrowband ECs [20,21] could provide high-sensitivity trace gas detection, covering a significant part of the molecular fingerprint region in a single measurement. Another example is cavity-enhanced HHG. Here, the attainable photon energy and flux have been shown to scale with the decreasing duration of the driving pulse [12,14,19,22]. Together with a suitable gating technique, intracavity pulses approaching the few-cycle regime could enable the efficient generation of bright isolated attosecond pulses at megahertz repetition rates [23,24]. This would dramatically reduce the acquisition time in pump-probe experiments involving the detection of charged particles [25].

In this Letter, we report on an EC with an average finesse exceeding 300, which supports a 10 dB bandwidth of 195 nm (1800 cm^{-1}) centered at 1050 nm. We measure intracavity pulse duration of 19 fs (5.4 cycles) and an average power of 1.04 kW, limited by the seeding laser system. To accomplish this bandwidth increase by a factor of 2 over state-of-the-art femtosecond ECs, we address challenges related to the mirror design, production, and characterization, as well as to the cavity setup and intracavity pulse characterization.

The design and the production of multilayer cavity mirrors that significantly surpass the bandwidth of standard

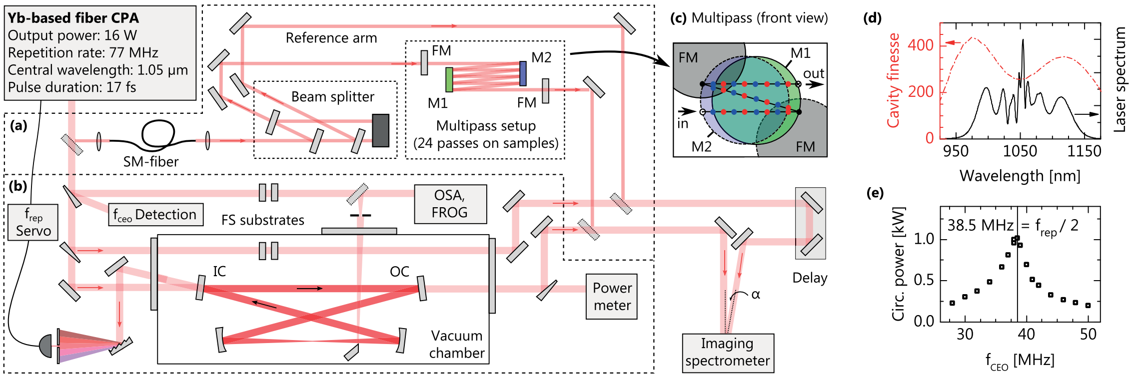

Fig. 1. (a) Setup for multipass SSI measurements. (b) Setup for enhancement cavity (EC) experiments. The cavity includes two partially reflective mirrors (IC, OC). (c) Front view of the multipass setup illustrating the beam path. Two unprotected gold-coated folding mirrors are used to achieve 24 reflections (blue and red dots) on two sample mirrors (M1, M2). (d) Output spectrum of the laser and the finesse of the EC. (e) Intracavity power for the different values of the laser f_{CEO}.

quarter-wave stacks are challenging. Designs of such coatings typically exhibit a very low tolerance with respect to thickness variations in production. This results in deviations of the phase characteristics of the produced coatings from the design and variations among individual coating deposition runs of the same design. Efficient enhancement is only possible if the spectral phase accumulated during one round-trip in the cavity deviates by less than approximately π/F from a linear phase (F = Finesse). Thus, for a four-mirror cavity with $F = 300$, the maximum acceptable phase deviation per mirror is about 2.5 mrad, which is far less than typical errors for broadband coatings. However, an EC with a suitable round-trip phase can be built by combining mirrors from several coating runs. This approach renders a reliable pre-characterization of the mirror phase with a precision of a few milliradians indispensable. To this end, we measure the accumulated spectral phase from multiple reflections on two 1”-diameter sample mirrors using spatial-spectral interferometry (SSI) [26].

Figure 1 shows the overall experimental setup. The Yb-based chirped-pulse fiber amplification system, previously described in [27], delivers 180 fs pulses at 77 MHz. The spectrum is broadened in a photonic-crystal fiber (NKT, LMA-25) and compressed to 17 fs in a double-angle chirped-mirror setup, with an output average power of 16 W. For the mirror-characterization setup [Fig. 1(a)], a small fraction of this power is coupled to a single-mode fiber for spatial filtering. The transmitted light is then collimated and split into a sample and a reference arm in a setup composed of three partially reflective mirrors produced in the same coating deposition run, placed under a small angle of incidence (AOI). This beam splitting setup ensures that the beams in both arms accumulate the same phase from substrates and from the coatings of the transport mirrors. The sample beam is subjected to a total of 24 reflections on two 1” sample mirrors [Fig. 1(c)]. The AOI on the sample mirrors is 1.5°. Thus, the polarization dependence is negligible. The reference and the sample beams intersect at the entrance slit of an imaging spectrometer, producing interferograms from which the accumulated spectral phase difference can be retrieved [26]. Figure 2(a) shows the spectral phase of a reference measurement of two unprotected gold mirrors. The maximum deviation from the expected flat phase is less than 1.5 mrad.

Novel cavity mirrors with a reflectivity $R > 99.995\%$ (highly reflective, HR) and $R = 99 \pm 0.3\%$ (partially reflective, PR) in the wavelength range between 950 and 1150 nm were designed and produced (Layertec GmbH). The design goal was group delay dispersion (GDD) in reflection of 0 fs^2 with deviations within ± 1 fs^2 over this bandwidth. Nb_2O_5 and SiO_2 were chosen as coating materials. The theoretical round-trip spectral

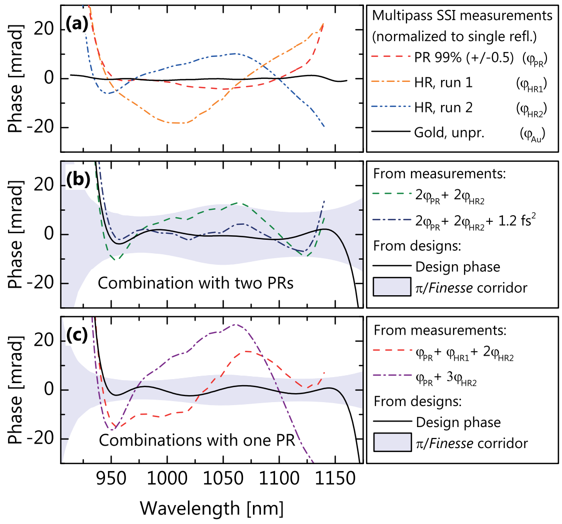

Fig. 2. (a) Spectral phase retrieved from multipass SSI measurements of three different multilayer mirror coatings (PR, partially reflective; HR, highly reflective) and a bare gold coating. (b) Sum of the measured spectral phases (green; blue: with an additional positive GDD of 1.2 fs^2) and of the corresponding coating designs (black) of a mirror combination suitable for a four-mirror impedance-matched EC. (c) Sum of the measured spectral phases (red, purple) and of the corresponding coating designs (black), of the mirror combinations suitable for an input-coupler limited four-mirror EC.

phase of a four-mirror cavity with these mirror designs is shown in Figs. 2(b) and 2(c), for an impedance-matched configuration and an input-coupler limited configuration, respectively. The production process was optimized to achieve an absolute thickness deviation of below 0.5 nm per layer and a maximum spatial inhomogeneity of 0.1% over a diameter of 10 mm on each substrate. Two coating runs (HR1, HR2) were performed with the HR design. For the PR mirror coating, the positioning of the substrates in the machine was chosen to achieve a graded distribution of spectral shifts of the GDD curve.

Figure 2(a) shows phase measurements of the three produced coatings. The measured spectral phases deviate significantly from the designs. The spectral phases of the PR and the HR2 coatings have similar curvatures with opposite signs. In Fig. 2(b), the sum of the measured spectral phases for two of each of these coatings is shown. The resulting curve represents the single-round-trip phase in a four-mirror impedance-matched cavity. It lies mostly within the π/F-corridor calculated from the measured transmission of the PR coatings. The remaining negative curvature of the phase corresponds to a GDD of about $-1.2\ \mathrm{fs}^2$. Figure 2(c) illustrates that an input-coupler limited EC with only one PR is not viable with these mirror coatings: the combination of a higher finesse and a worse shape of the spectral phase does not allow for a broadband enhancement.

Figure 1(b) depicts the setup used for the cavity-based experiments. The impedance-matched cavity is composed of two HR2-coated mirrors with a radius of curvature of 600 mm and two flat PR mirrors used as input- and output-coupling mirrors (IC, OC, respectively). The finesse of the impedance-matched cavity, as calculated from transmission measurements of the PR coating, and the laser spectrum are shown in Fig. 1(d). The reflections off two thin fused silica (FS) wedges are used for the detection of the carrier-envelope offset frequency f_{CEO}, for pulse characterization and for the reference arm of cavity-SSI measurements. In the SSI reference arm, two uncoated FS substrates compensate for the dispersion of the IC and OC substrates in the sample arm. The repetition frequency of the laser is locked to the EC using the Pound–Drever–Hall scheme. For the generation of the error signal, a narrow part of the laser spectrum at a wavelength of about 1000 nm is chosen. A D-shaped silver mirror is used to clip a small part of the intracavity light (<0.1%) to circumvent the spectral filtering and phase of the cavity mirrors in transmission for pulse characterization. The clipped beam is spatially filtered using a pinhole. Since the cavity mode size is not wavelength independent, the measured spectra have to be corrected for the clipping efficiency. The beam transmitted through the OC is used for the SSI sample arm and to measure a portion P_{leak} as a diagnostic for the intracavity power. The intracavity power is calculated accounting for the spectrally varying transmission of the PR coating $T_{\mathrm{PR}}(\lambda)$ and the intracavity spectrum $I(\lambda)$:

$$P_{\mathrm{circ}} = P_{\mathrm{leak}} \frac{\int I(\lambda)\mathrm{d}\lambda}{\int I(\lambda) T_{\mathrm{PR}}(\lambda)\mathrm{d}\lambda}. \tag{1}$$

In a first experiment, the optimal offset frequency [19] of the cavity in vacuum is determined. Figure 1(e) shows P_{circ} for a scan of the laser f_{CEO}. It peaks at 38.5 MHz, corresponding to $f_{\mathrm{rep}}/2$. The intracavity spectrum for this f_{CEO} is plotted in Fig. 3(a). The 10 dB spectral bandwidth is 168 nm. The intracavity average power was 950 W, and the average power enhancement factor was 68. The spectral phase of the intracavity pulses with respect to the incoming light [Fig. 3(c)] is measured via SSI. The negative curvature of the cavity round-trip phase can be compensated for by adding some dispersive material to the cavity. In our setup, this can be conveniently achieved by flooding the vacuum chamber with a small amount of ambient air. At an air pressure of about 24 mbar in the chamber, we obtain the broadest spectral bandwidth in the EC. To exploit this increased bandwidth, we slightly broaden the input spectrum. Figure 3(b) shows the resulting intracavity spectrum exhibiting a 10 dB bandwidth of 195 nm. Here, the average power was 1040 W with an average power enhancement of 75.

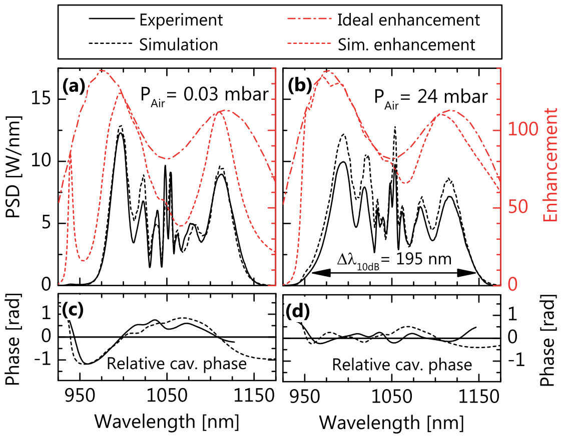

Fig. 3. Measured and calculated intracavity spectra, and calculated spectral enhancement in vacuum (a) and with 24 mbar of air pressure (b). The spectral enhancement is shown for an "ideal" dispersion-free cavity and for the mirror phase shown in Fig. 2. (c,) (d) Measured and calculated cavity phase.

Figure 3 also shows the spectral enhancement and phase calculated with the phase data from the multipass measurements (Fig. 2), without additional dispersion [Figs. 3(a) and 3(c)], and with an additional GDD of $1.2\ \mathrm{fs}^2$ [Figs. 3(b) and 3(d)]. From these and the experimental input laser spectra, intracavity spectra are calculated. The good agreement of both simulated cavity spectra and phase curves with the experiment confirms the accuracy and utility of the multipass SSI measurements.

The laser pulse compression is optimized to achieve minimal pulse duration in the cavity. We characterize the intracavity pulse using two independent methods. First, we retrieve the pulse from second-harmonic-generation frequency-resolved optical gating (FROG) measurements of the clipped intracavity beam. The resulting spectral phase has to be corrected for the spectral phase of the vacuum chamber window. Additionally, we retrieve the intracavity pulses' spectral phase from FROG measurements of the input pulse, together with SSI measurements of the relative cavity phase. Here, two fused silica substrates in front of the FROG device account for the dispersion of the vacuum chamber window and the input coupler (Fig. 1). To calculate the pulse duration, the intracavity spectrum is measured independently. The results of the retrieval in the frequency and in the time domain are shown in Figs. 4(b) and 4(c). The full-width at half-maximum intensity pulse durations determined from the first and second methods are 18.8 and 19 fs, respectively, for the EC in vacuum

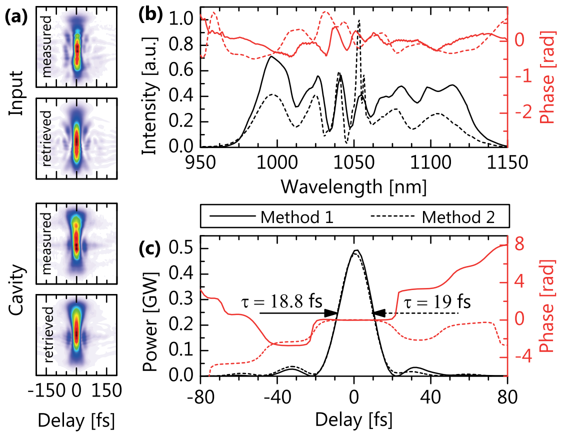

Fig. 4. (a) Measured and retrieved FROG traces of input and cavity pulses. The FROG errors were 0.008 and 0.005, respectively. (b) Intracavity spectra and spectral phases calculated by both methods. (c) Corresponding temporal intensities and phases.

(Fourier limit: 17.5 fs). The peak power of the intracavity pulse is about 0.5 GW.

In conclusion, we have demonstrated methods enabling high-finesse ECs that substantially surpass the state-of-the-art in bandwidth and support pulses approaching the few-cycle range. While a robust coating design and an accurate deposition is of utmost importance, the current error margins in production can only be overcome by combining mirrors from several coating runs. To allow for a quick identification of suitable mirror combinations, we have demonstrated a simple multipass setup capable of measuring the spectral phase of mirrors with, to the best of our knowledge, an unprecedented precision of 1.5 mrad. Further, we have presented methods for the reliable characterization of pulses in such cavities and measured pulses of sub-20 fs duration. We increased the bandwidth of this EC to about 1800 cm^{-1} by fine-tuning the cavity dispersion with the air pressure in the vacuum chamber. For applications that do not allow the presence of a gas, the same effect can be reached by a thin plate placed under Brewster's angle in the EC, e.g., a 56 μm fused silica or a 7 μm $\mathrm{Si_3N_4}$ plate.

The intracavity bandwidth reported here will immediately benefit a host of broadband spectroscopy schemes. For instance, femtosecond stimulated Raman spectroscopy [28] with this cavity would cover half the molecular fingerprint region without the need for tuning. Furthermore, the demonstrated pulse duration, together with a suitable gating technique [24], promises to enable the efficient generation of isolated attosecond pulses via HHG for time-resolved experiments in attosecond physics at multi-megahertz repetition rates.

Funding. Deutsche Forschungsgemeinschaft (DFG) (MAP); Fraunhofer-/Max-Planck-Gesellschaft Cooperation (MEGAS); European Research Council (ERC) (617173).

Acknowledgment. The authors thank the fiber laser group at the Institute of Applied Physics at Friedrich-Schiller-University Jena for providing the laser. They also thank T. Saule and M. Högner for helpful discussions.

REFERENCES

1. J. Hodgkinson and R. P. Tatam, Meas. Sci. Technol. **24**, 012004 (2013).
2. G. Gagliardi and H.-P. Loock, *Cavity-Enhanced Spectroscopy and Sensing* (Springer, 2014).
3. T. Gherman and D. Romanini, Opt. Express **10**, 1033 (2002).
4. B. Bernhardt, A. Ozawa, P. Jacquet, M. Jacquey, Y. Kobayashi, T. Udem, R. Holzwarth, G. Guelachvili, T. W. Hänsch, and N. Picqué, Nat. Photonics **4**, 55 (2009).
5. F. Adler, M. J. Thorpe, K. C. Cossel, and J. Ye, Annu. Rev. Anal. Chem. **3**, 175 (2010).
6. A. Foltynowicz, P. Masłowski, A. J. Fleisher, B. J. Bjork, and J. Ye, Appl. Phys. B **110**, 163 (2013).
7. M. A. R. Reber, Y. Chen, and T. K. Allison, Optica **3**, 311 (2016).
8. C. Gohle, T. Udem, M. Herrmann, J. Rauschenberger, R. Holzwarth, H. A. Schuessler, F. Krausz, and T. W. Hänsch, Nature **436**, 234 (2005).
9. R. Jones, K. Moll, M. Thorpe, and J. Ye, Phys. Rev. Lett. **94**, 193201 (2005).
10. A. Cingöz, D. C. Yost, T. K. Allison, A. Ruehl, M. E. Fermann, I. Hartl, and J. Ye, Nature **482**, 68 (2012).
11. A. Ozawa and Y. Kobayashi, Phys. Rev. A **87**, 022507 (2013).
12. I. Pupeza, S. Holzberger, T. Eidam, H. Carstens, D. Esser, J. Weitenberg, P. Rußbüldt, J. Rauschenberger, J. Limpert, T. Udem, A. Tünnermann, T. W. Hänsch, A. Apolonski, F. Krausz, and E. Fill, Nat. Photonics **7**, 608 (2013).
13. C. Benko, T. K. Allison, A. Cingöz, L. Hua, F. Labaye, D. C. Yost, and J. Ye, Nat. Photonics **8**, 530 (2014).
14. H. Carstens, M. Högner, T. Saule, S. Holzberger, N. Lilienfein, A. Guggenmos, C. Jocher, T. Eidam, D. Esser, V. Tosa, V. Pervak, J. Limpert, A. Tünnermann, U. Kleineberg, F. Krausz, and I. Pupeza, Optica **3**, 366 (2016).
15. C. Gohle, B. Stein, A. Schliesser, T. Udem, and T. W. Hänsch, Phys. Rev. Lett. **99**, 263902 (2007).
16. L. Rutkowski and J. Morville, Opt. Lett. **39**, 6664 (2014).
17. A. Khodabakhsh, V. Ramaiah-Badarla, L. Rutkowski, A. C. Johansson, K. F. Lee, J. Jiang, C. Mohr, M. E. Fermann, and A. Foltynowicz, Opt. Lett. **41**, 2541 (2016).
18. R. J. Jones and J. Ye, Opt. Lett. **27**, 1848 (2002).
19. S. Holzberger, N. Lilienfein, M. Trubetskov, H. Carstens, F. Lucking, V. Pervak, F. Krausz, and I. Pupeza, Opt. Lett. **40**, 2165 (2015).
20. D. J. Taylor, M. Glugla, and R.-D. Penzhorn, Rev. Sci. Instrum. **72**, 1970 (2001).
21. S.-I. Zaitsu, H. Izaki, and T. Imasaka, Phys. Rev. Lett. **100**, 073901 (2008).
22. S. Holzberger, N. Lilienfein, H. Carstens, T. Saule, M. Högner, F. Lücking, M. Trubetskov, V. Pervak, T. Eidam, J. Limpert, A. Tünnermann, E. Fill, F. Krausz, and I. Pupeza, Phys. Rev. Lett. **115**, 023902 (2015).
23. M. Louisy, C. L. Arnold, M. Miranda, E. W. Larsen, S. N. Bengtsson, D. Kroon, M. Kotur, D. Guénot, L. Rading, P. Rudawski, F. Brizuela, F. Campi, B. Kim, A. Jarnac, A. Houard, J. Mauritsson, P. Johnsson, A. L'Huillier, and C. M. Heyl, Optica **2**, 563 (2015).
24. M. Högner, V. Tosa, and I. Pupeza are preparing a manuscript to be titled "Generation of isolated attosecond pulses with enhancement cavities—a theoretical study."
25. M. I. Stockman, M. F. Kling, U. Kleineberg, and F. Krausz, Nat. Photonics **1**, 539 (2007).
26. A. P. Kovács, R. Szipöcs, K. Osvay, and Z. Bor, Opt. Lett. **20**, 788 (1995).
27. T. Eidam, F. Röser, O. Schmidt, J. Limpert, and A. Tünnermann, Appl. Phys. B **92**, 9 (2008).
28. D. R. Dietze and R. A. Mathies, ChemPhysChem **17**, 1224 (2016).

Chapter 9

Temporal solitons in free-space enhancement cavities

by

Nikolai Lilienfein, Christina Hofer, Tobias Saule, Maximilian Högner,
Michael Trubetskov, Vladimir Pervak, Ernst Fill, Claudius Riek,
Alfred Leitenstorfer, Jens Limpert, Ferenc Krausz and Ioachim Pupeza

this manuscript has been submitted for publication
in *Nature Photonics* on June 14th, 2018[1].

---

[1] A revised version of this manuscript has been published in *Nature Photonics* on January 21st, 2019 [123].
DOI: 10.1038/s41566-018-0341-y

Contributions

I conceived the experiments together with C.H. and I.P.. I designed the setup, performed the experiments, analyzed the data and wrote most of the manuscript.

Temporal solitons in free-space femtosecond enhancement cavities

N. Lilienfein[1,2], C. Hofer[1,2], T. Saule[1,2], M. Högner[1,2], M. Trubetskov[1], V. Pervak[2],
E. Fill[2], C. Riek[3], A. Leitenstorfer[3], J. Limpert[4], F. Krausz[1,2], I. Pupeza[1,2]

1 Max-Planck-Institut für Quantenoptik, Hans-Kopfermann-Str. 1, 85748 Garching, Germany
2 Ludwig-Maximilians-Universität München, Am Coulombwall 1, 85748 Garching, Germany
3 Universität Konstanz, Department of Physics and Center for Applied Photonics, 78457 Konstanz, Germany
4 Friedrich-Schiller-Universität Jena, Institut für Angewandte Physik, Albert-Einstein-Straße 15, 07745 Jena, Germany

email: nikolai.lilienfein@mpq.mpg.de

Temporal dissipative solitons (TDS) in nonlinear optical resonators are self-compressed, self-stabilizing and indefinitely circulating wave packets. Owing to these properties, TDS have been harnessed for the generation of ultrashort pulses and frequency combs in active and passive laser architectures, including mode-locked lasers[1-4], passive fibre resonators[5] and microresonators[6-11]. Here, we demonstrate TDS formation in a free-space enhancement cavity with a Kerr nonlinearity and a spectrally tailored finesse. By locking a 100-MHz-repetition-rate train of 350-fs, 1035-nm pulses to this cavity-soliton (CS) state, we generate a 37-fs sech^2-shaped pulse with a peak-power enhancement of 3200, which exhibits low-frequency intensity-noise suppression. The power scalability unique to free-space cavities, the unprecedented combination of peak-power enhancement and temporal compression, and the CS-specific noise filtering attest a vast potential of this novel platform of optical solitons for applications including spatiotemporal filtering and compression of ultrashort pulses, and cavity-enhanced nonlinear frequency conversion.

Optical solitons are localised electromagnetic wave packets propagating through a dispersive, nonlinear medium while maintaining a constant structure. In nonlinear optical resonators they manifest as temporal dissipative solitons[4] (TDS), i.e., asymptotically stable steady states associated with one or more pulses capable of circulating, in principle, ad infinitum. The duration and peak intensity of these pulses are determined by the balance between dispersion and self-phase-modulation on the one hand, and between loss and gain mechanisms on the other. Besides being highly interesting objects from a fundamental nonlinear-optics perspective, their properties, applied in particular for the passive mode-locking of active laser resonators[1-4], have made them a cornerstone of ultrafast-optics and frequency-comb technology. More recently, the generation of temporal cavity solitons (CS) in externally-excited, passive optical resonators has rapidly developed into an active field of research. First demonstrated in 2010 in continuous-wave (CW) laser-driven passive fibre resonators[5], CS formation has since been observed in various types of high-finesse microresonators[6-11], playing a crucial part in the development of a new family of frequency-comb sources[12], and facilitating fundamental research on soliton dynamics[13,14]. Compared to these CS platforms, free-space femtosecond enhancement cavities[15-21] (EC) offer unparalleled flexibility regarding dispersion control, access to the beam and geometric power scalability, in particular permitting peak powers significantly exceeding the catastrophic self-focussing limit in optical materials.

In this Letter, we report the generation of cavity solitons in a macroscopic enhancement cavity. In particular, we observe intracavity temporal self-compression and intensity self-stabilisation of femtosecond pulses. Furthermore, we introduce spectrally-tailored input coupling, which allows for the CS power enhancement to surpass the limits set by the temporal and spectral overlap between intracavity solitons and driving pulses applying to previous CS experiments[11]. This improvement enables a peak-power enhancement exceeding that in conventional, broadband femtosecond ECs by more than one order of magnitude[15,22], while allowing similar

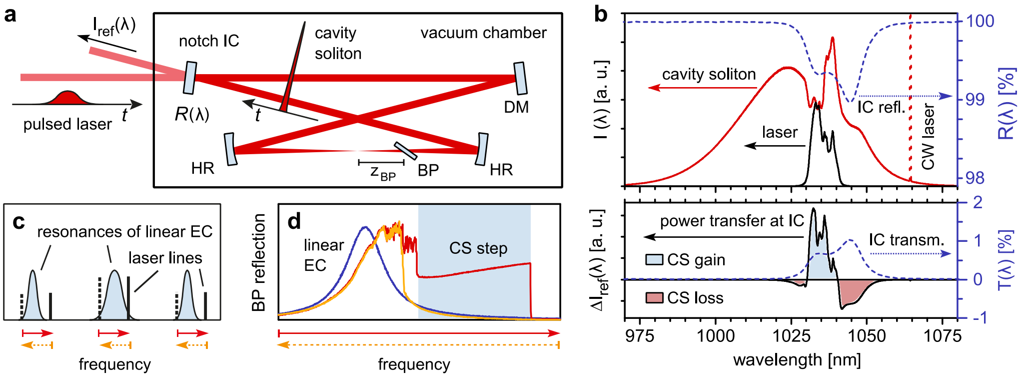

Fig.1. **Concept for efficient cavity soliton generation.** (a) A train of laser pulses is coupled to a free-space EC comprising an input coupling mirror with a spectrally tailored reflectivity *R*(λ) (notch IC), a dispersive mirror (DM) and two curved, highly-reflective mirrors (HR). The EC incorporates a movable sapphire plate arranged under Brewster's angle (Brewster plate, BP). (b, upper panel) Cavity soliton spectrum (red), driving laser spectrum (black), and spectral reflectivity of the notch IC (blue). The sharp peak at 1064 nm is the spectrum of an auxiliary continuous-wave laser necessary for the locking scheme (see Methods). (b, lower panel) Difference of the reflected spectral intensities for the laser being far from resonance and being locked to the CS state, illustrating the high spectral overlap facilitated by the IC transmission. A similar scheme has previously been proposed in the context of intracavity plasma generation[22]. (c) For CS generation, the lines of the input laser frequency comb (black) are adiabatically swept over the cavity resonances. (d) Normalised cavity transmission for frequency sweeps for low (blue) and high input power (sweeps from high to low frequency (red) and back (orange)) exhibiting bistability and the characteristic soliton step.

pulse durations. The intracavity pulse represents – to the best of our knowledge – the shortest and by far most energetic CS reported to date.

The 100-MHz bowtie ring EC consists of four mirrors with dielectric coatings, and an uncoated sapphire plate of 1-mm thickness, placed at Brewster’s angle in the focussed cavity arm (Fig.1.a). An anomalous roundtrip dispersion of about $-15\ \mathrm{fs}^2$ was achieved over a spectral width of 60 nm by combining custom-produced mirrors. The cavity was operated in vacuum. For a high coupling efficiency of the 350-fs (FWHM) driving pulses from our mode-locked laser (MLL) to a CS with a significantly broader spectrum, the reflectivity of the input coupling mirror (IC) was spectrally tailored to match the width of the transmitted CS spectrum to that of the MLL (Fig.1.b). This led to a cavity finesse exceeding 10,000 for the outer parts of the CS spectrum, opposed to 840 in the range of the driving laser spectrum. Sweeping the laser frequency at sufficient driving power over the cavity resonances, the bistable step in the cavity transmission signal characteristic for soliton generation[6] was observed (Fig.1.c,d). The soliton step was reliably produced during every sweep. To stably maintain specific nonlinear cavity states[23,24], the detuning Δf_{cav} of the MLL frequency comb from the cavity resonances was actively stabilised with the aid of an auxiliary low-power continuous-wave (CW) laser, locked to a resonance of the linear EC (Fig.2.a, Methods). Because of the negligible temporal overlap between CW laser and MLL pulses, this lock is insensitive to the MLL-induced nonlinear cavity phase distortions. The carrier-envelope offset frequency (f_0) of the MLL is independently stabilised to an adjustable radio-frequency reference.

Similar to recent observations in microresonators driven by pulsed lasers[11], we found that the soliton step occurs only for a limited range of f_0 (Fig.2.d), corresponding to about 4% of the free spectral range of the EC. It is most pronounced at the upper edge of this range. Figures 3 shows the evolution of the intracavity spectrum during a sweep of the detuning Δf_{cav} at $f_0 = 26\ \mathrm{MHz}$. At a specific detuning, the intracavity spectrum changes from a broad but modulated shape to the smooth, nearly sech^2-shaped spectrum characteristic for solitons. Similar to the observation reported in Ref.[24], we found that the width of the optical CS spectrum increases with increasing detuning.

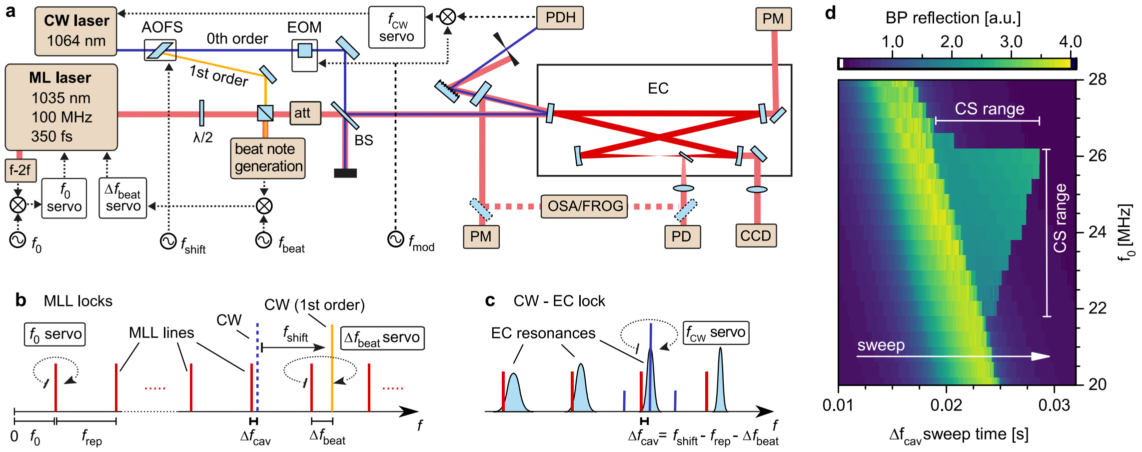

Fig.2. **Setup, locking scheme and f_0-dependence of the soliton regime.** (a) Schematic view of the locking setup and the cavity diagnostics. The frequency f_{cw} of an auxilliary continuous-wave (CW) laser is locked to an enhancement cavity (EC) resonance using the Pound-Drever-Hall scheme (PDH). (EOM: Electro-optic modulator, f_{mod}: modulation frequency, BS: beamsplitter). A beatnote between the carrier-envelope-offset frequency (f_0)- stabilised mode-locked laser system (MLL) and a copy of the CW laser shifted by the frequency f_{shift} is generated and locked to an adjustable frequency (f_{lock}). (AOFS: acousto-optic frequency shifter). The power reflected off the EC is measured with a powermeter (PM). For analysis of the intracavity light, both the transmission through a mirror and the reflection off the Brewster plate can be used. (PD: photodiode, OSA: optical spectrum analyser, FROG: frequency-resolved optical gating). (b) Frequency-domain picture of the CW-laser lock to the linear cavity resonances. The weaker lines around f_{cw} indicate the PDH sidebands. (c) Frequency-domain picture of the MLL lock resulting in an adjustable detuning Δf_{cav} between linear cavity resonances and MLL frequency comb lines at the wavelength of 1064 nm. (d) Cavity transmission for slow blue-to-red sweeps of Δf_{cav} for different values of f_0 showing the strong f_0-dependence of the CS step.

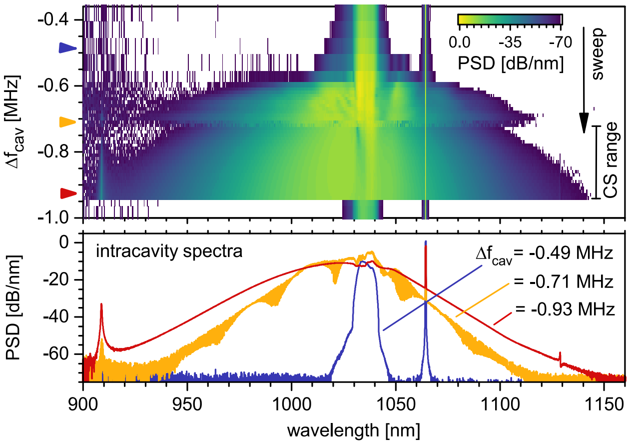

Fig.3. **Soliton evolution.** Contour plot of the intracavity spectra for a sweep of the detuning Δf_{cav} (upper panel), and line cuts at three values of Δf_{cav} (lower panel). The cavity-enhanced CW laser is visible as a narrow peak at 1064 nm. The peak at 910 nm corresponds to the zero-crossing of the cavity roundtrip phase and has a relative spectral intensity of -22 dB with respect to the soliton spectrum.

We characterised the temporal profile and possible chirp of the intracavity pulse using frequency-resolved-optical gating (FROG) measurements for a CS state close to maximum detuning at Δf_{cav}=-0.98MHz. The retrieval yields an intracavity pulse duration of 37 fs (Fourier limit: 36.8 fs), with 98% of the pulse energy carried by the main pulse (Fig.4, Methods). The pulse shape furthermore reveals the existence of a temporal offset between the maxima of the driving pulse and the soliton, as recently predicted from simulations[25], of

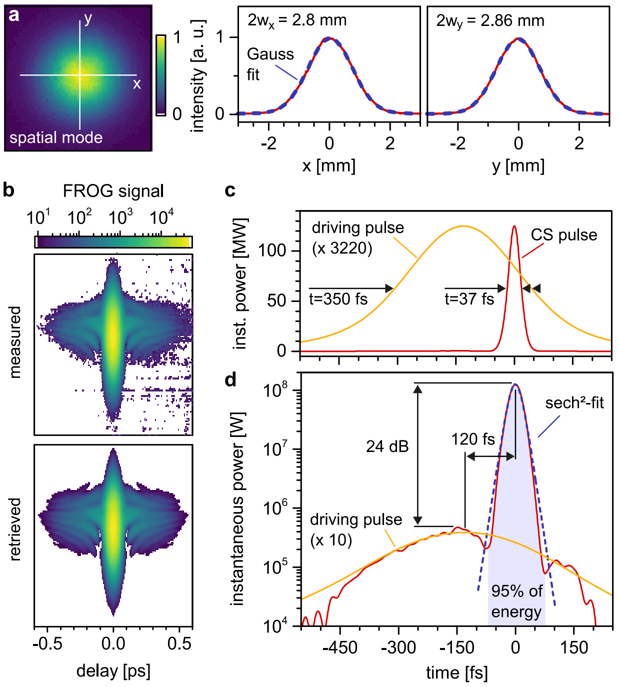

Fig.4. **Soliton characterisation** a) Spatial cavity mode profile of the CS state on the curved mirror. Line cuts (red) in x and y directions are shown together with Gaussian fits (blue). (b) Measured and retrieved frequency-resolved optical gating (FROG) traces of the CS pulse. The FROG error of the retrieval was 0.019. (c,d) The temporal intensities of the intracavity pulse (red) and driving pulses (yellow) calculated from FROG retrieval and power measurements shown on linear and logarithmic scales. The temporal offset was determined by fitting the driving pulse to the CS pedestal (d). The CS main pulse agrees well with a sech²-fit (blue).

about 120 fs. In this CS state, an average-power enhancement of 366 corresponding to a peak-power enhancement of 3220 was measured at an MLL input power of 1.3 W (see Methods). The power enhancement of the MLL in the same EC measured at an input power of 20.3 mW, low enough to maintain a linear response, was 444. Notably, the soliton peak power of 125 MW exceeds the critical power for self-focusing in sapphire by a factor of 40. The distance of the BP to the focal plane z_{BP} was 67 mm, corresponding to an effective mode area of 0.62 mm^2. Similar CS states were achieved at down to two orders of magnitudes lower input and intracavity power levels, limited by the focal width, by decreasing z_{BP}. Further scaling to higher intracavity power at larger z_{BP} was limited by thermal drifts, likely caused by absorption in the IC and/or the BP, preventing stable operation.

To verify the stability of the CS states, we measured the beatnote between the linearly cavity-enhanced CW light, and the light circulating in the MLL-driven nonlinear cavity. The frequency of this beat yields the absolute phase shifts $\Delta\varphi_{\mathrm{NL}}$ associated with the nonlinear intracavity states at the wavelength of 1064 nm. For a sweep of the detuning (Fig.5a), the RF spectrum of this signal changes from a broad and noisy structure with multiple pronounced beatnotes to a single, narrow peak, attesting a stable, fixed nonlinear phase in the soliton regime. Furthermore, we measured the relative intensity noise (RIN) of the CS state at the maximum detuning, and compared it to the RIN of the linear EC (for a low MLL power of 222 mW) and to that of the driving MLL (Fig.5b).

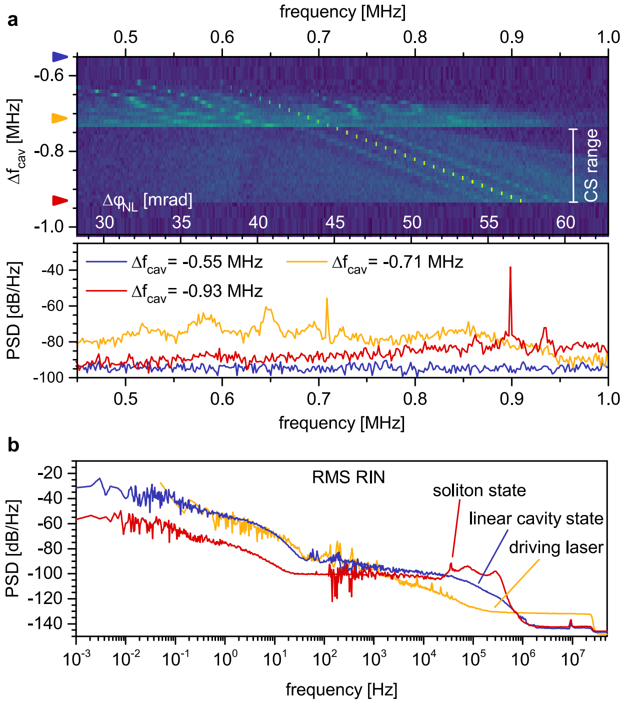

Fig.5. **Nonlinear phase and RIN.** (a) Contour plot of the radio frequency spectrum of the beating signal between the transmission of the linear cavity (CW laser) and nonlinear cavity (pulsed laser) states for a sweep of the detuning Δf_{cav} (upper panel). Line cuts at three values of Δf_{cav} are shown in the lower panel. Taking the free spectral range of the cavity into account, the frequency of the beat note can be converted to the roundtrip nonlinear phase shift $\Delta\varphi_{\mathrm{NL}}$ at the wavelength of 1064 nm. (b) Power spectrum of the root-mean squared (RMS) relative-intensity noise (RIN) for the pulsed driving laser, for a (low-power) linear cavity state and the soliton cavity state close to maximum detuning.

The results show that the low-pass characteristics of the linear cavity, setting in at 500 kHz, are conserved by the CS state. More strikingly, the CS state acts as a high-pass filter, suppressing the RIN for frequencies below 1 kHz by up to two orders of magnitude with respect to the driving laser, while the linear cavity closely follows the laser RIN in this range. This feature stems from the self-stabilising nature of dissipative solitons in general, together with a mechanism unique to CSs: the pulse energy and duration of a soliton are constrained by the balance between dispersion and the nonlinear phase shift, which is fixed to the driving laser detuning. Therefore, the energy of the CS state is largely independent of the input power, pulse duration, or spatial overlap. Between 30 and 500 kHz, the CS RIN is significantly higher than that of both the laser and the linear cavity state. This is most likely due to CS self-stabilisation dynamics excited by the phase noise of the locking loop at about 40 kHz. While the total root-mean-square RIN of 0.98% of the CS is comparable to the value of 1.05% measured for the linear cavity, the CS RIN is confined to a well-defined frequency range.

In conclusion, we have demonstrated the stable generation of cavity solitons in a free-space enhancement cavity with Kerr nonlinearity and a spectrally-tailored input coupler transmission. We have observed intracavity pulse compression by nearly an order of magnitude, to a 37-fs, nearly Fourier-limited sech^2-shaped pulse and a low-frequency RIN-suppression mechanism of cavity-soliton states. The peak-power enhancement surpasses by more than an order of magnitude the highest enhancement previously demonstrated in femtosecond enhancement cavities with comparable pulse durations[22], where the enhancement is severely limited by the cavity-mirror dispersion[15,26]. Further improvements of pulse duration, pulse energy and coupling efficiency can be expected from mirror optimisation and thermal management[27]. Spectrally-tailored input coupling could also benefit the coupling efficiency and bandwidth in microresonator geometries using multilayer mirrors[11].

Free-space enhancement cavities represent a uniquely flexible architecture for the study of cavity solitons, in which the effective nonlinearity, roundtrip dispersion and spectral finesse can be efficiently tailored. In this novel implementation, cavity solitons promise new opportunities for established applications of femtosecond enhancement cavities, such as high-repetition-rate high-order harmonic generation[16] for (extreme-) ultraviolet frequency-comb[19,20] and photoemission[28–30] spectroscopies, or path-length enhancement for vibrational spectroscopy[17,18,21], and are likely to enable new applications. In particular, the temporal, spectral and spatial filtering, and the low-frequency RIN suppression afforded by cavity solitons are highly attractive properties for the compression of ultrashort laser pulses at the full repetition rate of their primary source.

Methods

Enhancement cavity

The spectral power reflectivity of the IC coating was designed to exceed 99.9% in the band between 900 and 1200 nm, except for a notch centred at 1040 nm, with a minimum reflectivity of 99% and a half-depth width of 10 nm (Fig.1.a). The GDD of the mirror coatings was designed to approach 0 fs^2 for the IC and for two of the highly-reflective (HR) coatings, and -45 fs^2 for the fourth, dispersive HR mirror, over the same spectral range. Spectral phase measurements of the individual coatings were performed using multipass spatial-spectral interferometry[26]. Together with the calculated dispersion of the BP, we estimated a roundtrip GDD of about -15 fs^2 in the central spectral region. A ring-down measurement of the EC at a wavelength of 1064 nm yielded a finesse of 12,040. The corresponding roundtrip loss of 522 ppm is dominated by the BP reflections and scattering at the mirror coatings. The cavity finesse at 1035 nm is 842, implying an ideal linear enhancement of 491. A comparison to the experimental linear enhancement yields the spatial overlap of 0.9. The EC was set up as a symmetric bow-tie cavity with 600 mm radius of curvature of the concave mirrors and operated close to the inner edge of stability with a stability parameter of about -0.96. The 1/e^2 intensity diameters of the mode on the curved mirrors was 2.8 and 2.86 mm in tangential and sagittal axes, respectively (Fig.4.a).

Driving laser, locking scheme and soliton generation

The driving pulses with a duration of 350 fs (Fourier limit: 340 fs) and a central wavelength of 1035 nm were delivered at a repetition rate of 100 MHz by an Yb-fibre chirped-pulse amplifier. The Yb-system was seeded by an Er:fibre MLL (*C-Comb*, Menlo Systems) operating at a wavelength of 1.55 µm. The frequency shift to 1035 nm is performed using the electronic Kerr nonlinearity in a highly nonlinear germanosilicate fiber assembly. This step conserves the coherence of the Er:fiber front end[31], resulting in a high level of operational stability[32]. The average power impinging on the EC was adjustable between 10 mW and 10 W. The carrier-envelope-offset frequency f_0 of the MLL, measured with an integrated f-2f interferometer, was locked to the output of an RF waveform generator (Fig.2.a,b). For the cavity lock, a Nd:YAG nonplanar ring oscillator CW laser (*Mephisto*, Coherent) was transmitted through an acousto-optic frequency shifter (AOFS). The 0th-order transmission of the AOFS was phase-modulated in a resonant electro-optic modulator (EOM) and spatially combined with the MLL using an 80:20 beamsplitter, with 50 mW of the CW light impinging on the input coupler. In reflection from the EC, the CW beam at 1064 nm was spatially isolated with a grating and used to generate a Pound-Drever-Hall error signal, allowing the stabilisation of the CW-laser frequency to an EC resonance (Fig.2.a,c). The 1st-order diffraction of the CW laser in the AOFS, being frequency-shifted by $f_{\mathrm{shift}} =$

110 ± 2 MHz, was combined with a part of the MLL light. A beatnote was generated by broadening the MLL spectrum in a nonlinear fibre, subsequently cleaning the polarisation, and filtering the wavelength to a narrow spectrum at 1064 nm, which was sent to a photodiode. The signal was mixed down with a frequency $f_{\mathrm{lock}} = 10.58\,\mathrm{MHz}$, and can be locked by actuating on the repetition rate of the MLL. The detuning of the MLL frequency-comb lines from the cavity resonances Δf_{cav} at a wavelength of 1064 nm is given by $\Delta f_{\mathrm{cav}} = f_{\mathrm{shift}} - f_{\mathrm{rep}} - f_{\mathrm{lock}}$ (Fig.2.a,c). Soliton states were generated by sweeping f_{shift} either continuously using the analog frequency-modulation input of the waveform generator driving the AOFS, or in steps of <20 kHz using its digital control (Suppl. video).

Diagnostics

The spectral transmission of the broadband cavity mirrors is not uniform over the wavelength range of interest. To gain direct access to the intracavity light we therefore used the reflections off the BP, which was slightly detuned from Brewster’s angle for measurements of the intracavity spectrum, detuning curves, FROG trace and RIN data. Due to the position of the BP in the focused cavity arm, both reflections from the close to parallel BP surfaces were well separated spatially after collimation. A wire grid polarizer was used to filter out residual s-polarized light that is reflected off the BP after entering the cavity. The intracavity temporal intensity was calculated from the FROG retrieval (Fig.4.b), accounting for the material dispersion of the vacuum window, lens and wire-grid polarizer (16 mm of fused silica). The high intensity contrast of the measurement was facilitated by the spatial homogeneity of the beam, characteristic for ECs. Because of the high sensitivity of the BP reflectivity with respect to the angle between BP and the cavity beam axis, a calibration of the reflectivity with sufficient accuracy for precise intracavity power measurements would have been challenging. Instead, the intracavity power was calculated from a power measurement in transmission of a cavity mirror by accounting for its spectral transmission and for the intracavity spectrum[26]. To generate the beat signal shown in Fig.5, the transmission through a cavity mirror was spectrally filtered to a narrow range around 1064 nm using a grating. The resulting signal was sent to an amplified photodiode and measured using an electronic spectrum analyser. The RIN data was generated by acquiring oscilloscope traces of the signal of a fast photodiode with lengths of 1000 s and 200 ms, and stitching the resulting power spectra. For the RIN measurements of the linear cavity and CS, the driving laser power was 222 mW and 1.42W, respectively and the laser was locked at Δf_{cav}=-0.642 MHz and Δf_{cav}=-0.93 MHz, respectively.

Funding

European Research Council (ERC) (617173), Deutsche Forschungsgemeinschaft (DFG) Excellence cluster “Munich Centre of Advanced Photonics” (MAP).

Acknowledgements

The authors gratefully acknowledge helpful suggestions from T. Herr and A. Apolonskiy. The authors thank S. Breitkopf and T. Buberl for assistance with the laser system, J. Gessner for phase measurements of cavity mirrors and M. Fischer for support concerning the offset-frequency stabilization. The autors acknowledge funding from the European Research Council (ERC) (617173), Deutsche Forschungsgemeinschaft (DFG) Excellence cluster “Munich Centre of Advanced Photonics” (MAP).

Author contributions

N.L., C.H., and I.P. planned and coordinated the experiments. N.L. designed and performed the experiments, and analysed the data. C.H., T.S., M.H. and I.P. assisted with experiments and data analysis. V.P. and M.T.

designed and produced the cavity optics. E.F. contributed to the experimental concept. C.R. and A.L. conceived and implemented the spectral shift of the erbium oscillator for seeding the ytterbium amplifier system. J.L. designed and provided the amplifier system. N.L. and I.P. wrote the manuscript with input from all other authors. I.P. und F.K. supervised the project.

References

1. Mollenauer, L.F. & Stolen, R.H. The soliton laser. *Opt. Lett.* **9,** 13 (1984).
2. Brabec, T., Spielmann, C. & Krausz, F. Mode locking in solitary lasers. *Opt. Lett.* **16,** 1961 (1991).
3. Haus, H.A. Mode-locking of lasers. *IEEE J. Select. Topics Quantum Electron.* **6,** 1173-1185 (2000).
4. Grelu, P. & Akhmediev, N. Dissipative solitons for mode-locked lasers. *Nat. Photon.* **6,** 84-92 (2012).
5. Leo, F. *et al.* Temporal cavity solitons in one-dimensional Kerr media as bits in an all-optical buffer. *Nat. Photon.* **4,** 471-476 (2010).
6. Herr, T. *et al.* Temporal solitons in optical microresonators. *Nat. Photon.* **8,** 145-152 (2014).
7. Saha, K. *et al.* Modelocking and femtosecond pulse generation in chip-based frequency combs. *Opt. Express* **21,** 1335-1343 (2013).
8. Liang, W. *et al.* High spectral purity Kerr frequency comb radio frequency photonic oscillator. *Nat. Commun.* **6,** 7957 (2015).
9. Yi, X., Yang, Q.-F., Yang, K.Y., Suh, M.-G. & Vahala, K. Soliton frequency comb at microwave rates in a high-Q silica microresonator. *Optica* **2,** 1078 (2015).
10. Brasch, V. *et al.* Photonic chip-based optical frequency comb using soliton Cherenkov radiation. *Science* **351,** 357-360 (2016).
11. Obrzud, E., Lecomte, S. & Herr, T. Temporal solitons in microresonators driven by optical pulses. *Nature Photon.* **11,** 600-607 (2017).
12. Pasquazi, A. *et al.* Micro-combs. A novel generation of optical sources. *Phys. Rep.* **729,** 1-81 (2018).
13. Jang, J.K., Erkintalo, M., Murdoch, S.G. & Coen, S. Ultraweak long-range interactions of solitons observed over astronomical distances. *Nat. Photon.* **7,** 657-663 (2013).
14. Xue, X. *et al.* Mode-locked dark pulse Kerr combs in normal-dispersion microresonators. *Nat. Photon.* **9,** 594-600 (2015).
15. Jones, R.J. & Ye, J. Femtosecond pulse amplification by coherent addition in a passive optical cavity. *Opt. Lett.* **27,** 1848 (2002).
16. Gohle, C. *et al.* A frequency comb in the extreme ultraviolet. *Nature* **436,** 234-237 (2005).
17. Adler, F., Thorpe, M.J., Cossel, K.C. & Ye, J. Cavity-Enhanced Direct Frequency Comb Spectroscopy: Technology and Applications. *Ann. Rev. of Anal. Chem.* **3,** 175-205 (2010).
18. Foltynowicz, A., Ban, T., Masłowski, P., Adler, F. & Ye, J. Quantum-noise-limited optical frequency comb spectroscopy. *Phys. Rev. Lett.* **107,** 233002 (2011).
19. Cingoz, A. *et al.* Direct frequency comb spectroscopy in the extreme ultraviolet. *Nature* **482,** 68-71 (2012).
20. Benko, C. *et al.* Extreme ultraviolet radiation with coherence time greater than 1 s. *Nat. Photon.* **8,** 530-536 (2014).
21. Reber, M.A.R., Chen, Y. & Allison, T.K. Cavity-enhanced ultrafast spectroscopy. Ultrafast meets ultrasensitive. *Optica* **3,** 311 (2016).
22. Holzberger, S. *et al.* Femtosecond Enhancement Cavities in the Nonlinear Regime. *Phys. Rev. Lett.* **115,** 23902 (2015).
23. Coen, S. & Haelterman, M. Modulational Instability Induced by Cavity Boundary Conditions in a Normally Dispersive Optical Fiber. *Phys. Rev. Lett.* **79,** 4139-4142 (1997).
24. Lucas, E., Guo, H., Jost, J.D., Karpov, M. & Kippenberg, T.J. Detuning-dependent properties and dispersion-induced instabilities of temporal dissipative Kerr solitons in optical microresonators. *Phys. Rev. A* **95** (2017).

25. Hendry, I. *et al.* Spontaneous symmetry breaking and trapping of temporal Kerr cavity solitons by pulsed or amplitude modulated driving fields. Preprint at https://arxiv.org/pdf/1803.10203.pdf (2018).
26. Lilienfein, N. *et al.* Enhancement cavities for few-cycle pulses. *Opt. Lett.* **42,** 271-274 (2017).
27. Lilienfein, N. *et al.* Balancing of thermal lenses in enhancement cavities with transmissive elements. *Opt. Lett.* **40,** 843-846 (2015).
28. Mills, A.K. *et al. in SPIE Optics + Optoelectronics,* edited by S.G. Biedron (SPIE2015), pp. 95121I.
29. Corder, C., *et al.* Ultrafast extreme ultraviolet photoemission without space charge. Preprint at https://arxiv.org/pdf/1801.08124.pdf (2018).
30. Saule, T., Heinrich, S., Schötz, J., Lilienfein, N., Högner, M., deVries, O., Plötner, M., Weitenberg, J., Esser, D., Schulte, J., Rüßbueldt, P., Limpert, J., Kling, M. F., Kleinberg, U. & Pupeza, I. High-Flux high-photon energy ultrafast extreme-ultraviolet photoemission spectroscopy at 18.4 MHz pulse repetition rate. *Manuscript submitted March 29, 2018, reference number* NPHOT-2018-03-00421A-Z.
31. Kumkar, S. *et al.* Femtosecond coherent seeding of a broadband Tm:fiber amplifier by an Er:fiber system. Opt. Lett. **37,** 554-557 (2012).
32. Wunram, M. *et al.* Ultrastable fiber amplifier delivering 145-fs pulses with 6-μJ energy at 10-MHz repetition rate. Opt. Lett. **40**, 823-826 (2015).

Chapter 10

Ultrafast optomechanical pulse picking

by

Nikolai Lilienfein, Simon Holzberger and Ioachim Pupeza

published in

Applied Physics B (2017)
DOI: 10.1007/s00340-016-6608-4

Contributions

I conceived the concept together with S.H. and I.P., performed the simulations and wrote most of the manuscript.

Appl. Phys. B (2017) 123:47
DOI 10.1007/s00340-016-6608-4

Applied Physics B
Lasers and Optics

Ultrafast optomechanical pulse picking

Nikolai Lilienfein[1] · Simon Holzberger[1,2] · Ioachim Pupeza[1]

Received: 2 September 2016 / Accepted: 1 December 2016 / Published online: 16 January 2017

Abstract State-of-the-art optical switches for coupling pulses into and/or out of resonators are based on either the electro-optic or the acousto-optic effect in transmissive elements. In high-power applications, the damage threshold and other nonlinear and thermal effects in these elements impede further improvements in pulse energy, duration, and average power. We propose a new optomechanical switching concept which is based solely on reflective elements and is suitable for switching times down to the ten-nanosecond range. To this end, an isolated section of a beam path is moved in a system comprising mirrors rotating at a high angular velocity and stationary imaging mirrors, without affecting the propagation of the beam thereafter. We discuss three variants of the concept and exemplify practical parameters for its application in regenerative amplifiers and stack-and-dump enhancement cavities. We find that optomechanical pulse picking has the potential to achieve switching rates of up to a few tens of kilohertz while supporting pulse energies of up to several joules.

1 Introduction

Picking individual pulses from the MHz-repetition-rate pulse trains produced by (amplified) laser oscillators is particularly important in the context of high-pulse-energy lasers. Here, pulse pickers are necessary to reduce the repetition rate of the seed oscillator pulse train before amplification in average-power-limited laser systems. Other prominent applications are the direct extraction of pulses from laser resonators (cavity dumping) [1], and the coupling of pulses into and out of the cavities of regenerative amplifiers [2–4]. Cavity dumping has also been demonstrated in passive external resonators known as enhancement cavities (ECs) [5, 6]. While this concept has not yet found widespread application, it has recently encountered renewed interest in the context of high-pulse-energy Yb-based amplifiers [7, 8]. The relevant properties of pulse pickers are the switching time and switching rate, efficiency, contrast, and optical bandwidth. Equally important for intracavity applications are properties which affect the transmitted pulses, i.e., losses, chromatic dispersion, and, for high-power applications, self-induced nonlinear and thermal effects.

Cavity dumping from oscillators and regenerative amplifier cavities typically relies on Pockels cells. These devices use the electro-optic Pockels effect in nonlinear crystals to rapidly rotate the polarization of the intracavity pulse upon application of a high voltage. Depending on its polarization, the pulse can be subsequently coupled out by means of a polarizer. The length of the crystals necessary to reach a polarization rotation sufficient for efficient switching is typically tens of millimeters. Pockels cells include several antireflection-coated surfaces which create losses. Since the electro-optic effect scales linearly with the electric field, the half-wave voltage increases with the aperture

---

This article is part of the topical collection “Enlightening the World with the Laser” - Honoring T. W. Hänsch guest edited by Tilman Esslinger, Nathalie Picqué, and Thomas Udem.

✉ Nikolai Lilienfein
nikolai.lilienfein@mpq.mpg.de

[1] Max-Planck-Institut fuer Quantenoptik,
Hans-Kopfermann-Strasse 1, 85748 Garching, Germany

[2] Present Address: Menlo Systems GmbH, Am Klopferspitz
19a, 82152 Martinsried, Germany

width. This, together with the availability of large crystals of sufficient quality, makes increasing the aperture of the cell technologically challenging [3]. The damage threshold of crystals and antireflective coatings, as well as nonlinear and thermal effects, are the limiting factors for the extractable peak and average power from regenerative amplifiers [3, 9]. State-of-the-art systems achieve pulse energies of 30 mJ at 10 kHz repetition rate and 200 mJ at 1 kHz [10]. For amplification, the pulses are typically stretched to durations in the nanosecond range [4, 11].

In contrast to the cavities of laser oscillators and of regenerative amplifiers, which include gain media, the increase in pulse energy in ECs depends on the correct temporal and spatial overlap of circulating and seeding pulses, and the growth per round-trip is typically small. Thus, losses, dispersion, and other distortions of the intracavity pulse are critical, and rule out the use of Pockels cells for efficient dumping. For proof-of-principle demonstrations of the stack-and-dump concept, acousto-optic modulators (AOMs) have been employed [5, 12, 13]. Here, the beam is coupled out by a transient grating, induced by an acoustic wave propagating in a solid, e.g., a fused silica plate. The switching time of these devices is determined by the beam size and by the speed of sound in the material. A sufficiently short switching time to pick pulses from a megahertz pulse train requires the beam to be tightly focused in the AOM. Recently, the extraction of 0.16 mJ pulses from an EC has been demonstrated [14]. The pulses were chirped to a duration of 2.5 ns, and the output repetition rate was 30 kHz. In particular, the high nonlinearity caused by the small beam size in the AOM represents a bottleneck for the further scaling of such systems [14].

Recently, a mechanical pulse picker based on a concept similar to a chopper wheel has been proposed as a possible way to circumvent these limitations [7]. Here, a moving mirror that periodically intercepts the circulating pulse would act as the switching element, avoiding the losses, dispersion, nonlinearities, and thermal lensing associated with intracavity transmissive elements. However, the centrifugal force that would occur in a chopper wheel spinning fast enough to couple out single pulses even from a tightly focused MHz-repetition-rate pulse train would be close to the limits given by the tensile strength of potential rotor materials. This poses a major technological challenge and would severely limit the capabilities of the such devices. Even if feasible, this output coupler would represent a high-precision element of considerable size, complexity, and cost.

In this article, we present a novel concept for an optomechanical pulse picker consisting of exclusively reflective optics. It uses rotating mirrors and stationary imaging mirrors in order to move an entire section of a beam path without affecting the beam path outside of this section. While sharing the advantages of the chopper wheel, the concept drastically reduces the mechanical demands on the rotor by using the beam path as a lever. We present three particular geometries and discuss their advantages and drawbacks. We find that devices based on this concept could be suitable to pick joule-level pulses from optical cavities with repetition rates of several tens of megahertz, at rates of several kilohertz.

2 Circular single-mirror geometry

Figure 1a shows the most basic variant of the concept. It is based on a mirror that rotates at a high angular velocity. The normal of its flat surface is tilted by a small angle from its rotation axis, such that the rotating mirror reflects a stationary input beam into a time-dependent deflection beam path. The rotating mirror surface is positioned in the center of curvature of a large spherical mirror. The deflection beam path impinges orthogonally on the stationary mirror surface for all rotation angles, and is reflected back along its incident path. Irrespective of the deflection angle, the second pass on the rotating mirror deflects the output beam along a path coinciding with the input path. Since the stationary spherical mirror images the surface of the rotating mirror onto itself, we refer to it as the imaging mirror. To achieve collimated input and output beams, a curved folding mirror can be used to focus the beam on the imaging mirror. Figure 1b illustrates the points where individual pulses from a pulse train impinge on the imaging mirror. If the deflection paths of subsequent pulses are separated by a distance Δs that is larger than the beam diameter, mirrors in the deflection beam path or openings in the imaging mirror can be used to pick pulses from the pulse train.

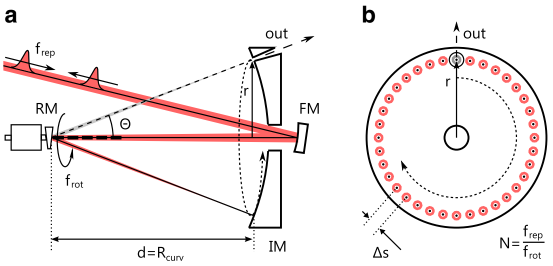

Fig. 1 **a** Side view of the circular single-mirror geometry comprising one rotating mirror (RM), a spherical imaging mirror (IM, radius of curvature R_{curv}) with an opening, and a curved folding mirror (FM). The beam path is shown for two rotation angles (*dashed line* beam path for output coupling). For a full rotation, the deflected beam path describes a cone. **b** Front view of the imaging mirror with N points of incidence of individual pulses from the incoming pulse train being distributed along a circle of radius r

The switching time τ of the pulse picker is given by the velocity with which the beam moves along the circle of radius r, and the $1/e^2$ beam radius w in that plane. If we require that $\Delta s = 2w$, we find that

$$\tau = \frac{w}{\pi r f_{\mathrm{rot}}}, \tag{1}$$

with f_{rot} being the revolution rate of the rotating mirror. This equation also holds for a chopper-wheel-based pulse picker. In this case, the value of r, is given by the size of the chopper wheel. For our optomechanical pulse picker, on the other hand, it depends on the deflection angle from the rotating mirror Θ and on the distance to the imaging mirror d, according to $r = d\sin(\Theta)$. The beam path is used as a lever, and the diameter of the rotor needs to be just large enough to provide a sufficient aperture for the transverse beam size. The switching rate is equal to the revolution rate. A magnetic bearing of the rotor is desirable to achieve a high rotation speed as well as a high stability of the rotor and of its revolution rate, a long lifetime, and to allow for operation in vacuum. In [15], a suitable self-bearing motor reaching a speed of 8.4 kHz intended for laser scanning applications has been demonstrated. With a length of 55 mm and a diameter of about 30 mm, the motor is quite compact. With this motor, and, e.g., an imaging mirror of 15 cm diameter and a beam radius of 50 µm in the focal plane, the switching time is 25.3 ns, corresponding to a maximum pulse repetition rate of close to 40 MHz. Precise holes with diameters in the range of several tens of µm can be manufactured, e.g., via laser drilling [16]. To allow for reliable pulse picking, the points of incidence of the pulses on the imaging mirror have to be fixed. To this end, the repetition rate of the pulse train has to be locked to an integer multiple of the rotation frequency. In addition, the pulse train has to be stabilized to a specific fixed phase with respect to the rotation phase. Both of these requirements are achievable with standard technologies.

A pulse picker of this kind could be used in a linear resonator cavity, with the imaging mirror being one of the end mirrors. The number of round-trips during one rotation period is $N = f_{\mathrm{rep}}/f_{\mathrm{rot}}$, with f_{rep} being the repetition rate of the resonator. The transverse separation of the paths of successive pulses is given by

$$\Delta s_1 = 2\pi d \sin(\Theta)\frac{f_{\mathrm{rot}}}{f_{\mathrm{rep}}}. \tag{2}$$

When the input beam path coincides with the rotation axis of the rotating mirror, the angle of incidence on its surface is constant, and equals half the deflection angle Θ. The polarization of the beam with respect to the imaging mirror surface turns with the rotating mirror. The spectral phase and reflectivity of dielectric mirror coatings typically show increasing polarization dependence with a larger angle of incidence and with an increasing spectral bandwidth. Even though the imaging setup does not affect the polarization geometrically, this effect will cause a birefringent spectral phase modulation increasing with the angle of incidence and the required bandwidth. Any rotation-angle-dependent modulation is periodic with f_{rot}, leading to a constant output of the system at f_{rot}. For some applications , however, small angles of incidence and, thus, a long distance d may be necessary.

For large values of d, the propagation time $\Delta t = 2d/c$ between the first and the second pass of the pulse on the rotating mirrors becomes relevant. During this time, the mirror rotates by $\Delta\phi = 2\pi f_{\mathrm{rot}}\Delta t$. This rotation results in an effective tilt β between the vectors normal to the mirror surface for the first and second passes given by

$$\sin\left(\frac{\beta}{2}\right) = \sin\left(\frac{\Theta}{2}\right)\sin\left(\frac{\Delta\phi}{2}\right). \tag{3}$$

For the example mentioned above, a distance $d = 0.5$m corresponding to $\Theta = 8.6°$, results in an effective tilt of 13.5 µrad.

A limitation of this type of geometry for high-power applications is presented by the high intensity on the imaging mirror. The beam radius w on the imaging mirror depends on the focusing power of the curved folding mirror and on the caustic of the surrounding resonator. A small beam waist reduces the necessary separation of adjacent spots, but increases the peak and average intensity on the imaging mirror. While no transmissive elements prone to thermal and nonlinear effects are used, mirror damage will occur for high peak intensities or fluences. Additionally, thermal lensing in mirrors can affect the operation of cavities at high average powers [17, 18]. While the overall size of the pulse picker can be scaled up with the required peak and average power, the necessity of focussing the beam on a cavity mirror is generally disadvantageous for high-power applications.

3 Circular double-mirror geometry

Figure 2 shows a second variant of the concept which mitigates the above problem. Here, two rotating mirrors and two imaging mirrors are used in a setup which is symmetric with respect to a central plane. The rotating mirrors are fixed on a single shaft which is driven by the motor. The curved imaging mirrors are arranged such that their focal points coincide with the center of the rotating mirror surfaces, analogously to a 4-f imaging configuration. The first rotating mirror reflects the input beam into a deflection beam path that depends on its rotation angle. The two imaging mirrors guide the deflected beam to the second rotating mirror, which produces a stationary output beam.

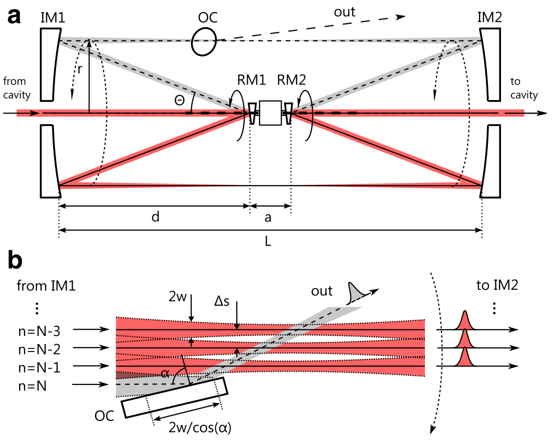

Fig. 2 **a** Side view of the circular two-mirror geometry with two rotating mirrors (RM1, RM2), two imaging mirrors (IM1, IM2) and an output coupling mirror (OC). The beam path is shown for two rotation angles (*dashed line* beam path just before output coupling). For a full rotation, the deflected beam path describes a cylinder between the imaging mirrors. **b** Schematic view of the grazing-incidence output coupling mirror. The beam path is shown for the three final round-trips of the pulse before the output coupling event (*dashed line*)

Between the rotating mirrors, some space is needed for the bearing and power unit of the rotor, separating their surfaces by a distance a. When the distance between the imaging mirrors L is large with respect to a and the deflection angle Θ is small, the imaging mirror configuration is close to a true 4-f imaging. In this case, the deflection beam is focused in the symmetry plane of the setup when the input and output beams are nearly collimated. For larger values of a, the beam has to be slightly divergent at the entrance of the pulse-picker setup and slightly convergent at the exit. A mirror placed at some point along the deflected beam path between the imaging mirrors can be used for input or output coupling of the pulse (Fig. 2b). For some applications, the resonator cavity may remain blocked for a small fraction of the rotation period after output coupling and/or before input coupling. Then, the picking mirrors can be larger than the beam size at the position of input/output coupling. The space just before or behind the coupling mirrors can also be used for the mechanical support of the rotor unit. The surface of the stationary mirrors can be either spherical or parabolic. Spherical mirrors are simpler to align and manufacture, but exhibit astigmatism when hit at nonzero angles of incidence. Note that the sagittal and tangential planes with respect to the rotating and imaging mirrors, and thus the astigmatism, are rotating together with the beam path. Particularly in resonators operated close to an edge of the stability range [19], this astigmatism will result in a rotating ellipticity of the cavity mode. Similar to the birefringent effects in dielectric mirror coatings mentioned before, this can be mitigated by decreasing the angle of incidence at the cost of increased size.

An optomechanical pulse picker of the second variant could be used in both linear and ring resonator cavities. For small angles of incidence on the mirrors, the following equation gives the pulse path separation for the second variant:

$$\Delta s_2 = \pi (L - a) \tan(\Theta) \frac{f_{\text{rot}}}{f_{\text{rep}}}. \tag{4}$$

It is similar to the one for the single-mirror geometry, but the total length, given here by the distance of the imaging mirrors L, doubles for otherwise identical parameters. In this geometry, the rotation of the mirrors during the propagation time along the deflection beam path can be compensated by adjusting the orientation of the rotating mirrors with respect to each other. In contrast to the single-mirror geometry, the spot size of the beam is large on both the rotating and the imaging mirrors. On the pulse-picking mirrors (output or input couplers), the beam size can be chosen corresponding to the required switching time by changing the position along the deflection beam path (Fig. 2b).

While the average power impinging on the picking mirrors is far lower than on the other optics, the small spot size necessary to achieve switching times below 100 ns causes a considerably higher peak intensity. The intensity on the output coupler can be reduced by placing it under grazing incidence. For instance, at an extreme angle of incidence α of 89°, the irradiated area would be increased by a factor of about 57. Generally, the peak fluence F of a beam with a Gaussian profile on the output coupler is

$$F = \frac{2\cos(\alpha)}{\pi w^2} E_{\text{p}}, \tag{5}$$

where E_{p} denotes the pulse energy. At $\alpha = 89°$, and a wavelength of 1 μm, the reflectivity of an uncoated quartz surface for s-polarized light is 94%. By avoiding a mirror with a coating, which contain high-refractive-index material and typically come with small deposition errors and contaminants, the highest possible damage threshold can be achieved. The output coupler, being a quartz (or sapphire, diamond, etc.) plate, can be readily and cost-effectively replaced. For a given switching time and rate, a larger spot size can be accommodated by increasing the overall size of the system. Thus, the maximum peak power scales with the square of the system size (Eqs. 4, 5).

4 Planar double-mirror geometry

In principle, the pulse-picker geometries discussed so far allow for an unobstructed deflection beam path for all rotation angles (apart from input or output couplers). Thus, they can provide a resonator with an open beam path for most of the rotation period, which corresponds to the input and/or output switching rate. However, in regenerative amplifiers for instance, the time between input coupling to and output coupling from the cavity is often only a fraction of the repetition period. Thus, the cavity needs to be closed for just a small range of rotation angles of the rotating mirrors. In the case of the two pulse-picker variants discussed so far, smaller imaging mirrors covering only the necessary rotation angles could be used. In addition, applications of this kind would allow for the use of a particularly advantageous third geometry, as shown in Fig. 3a. In contrast to the previous implementation, the axis of rotation of the rotating mirrors is perpendicular to the incoming beam path. The deflection beam paths for different rotation angles form a plane. The mirror surfaces of the rotor are parallel to the rotation axis and to each other. The imaging mirror setup is similar to the second variant, with the focal planes coinciding with the rotating mirror surfaces. However, the central axis along which the imaging mirrors are aligned is offset from the incoming beam and the rotating mirrors by a distance Δx. Figure 3b illustrates the beam path in the system. The 4-f configuration of the imaging mirrors creates an inverted image in the central plane, after the beam has passed each of the imaging mirrors once. In this plane, the beam is offset by $-\Delta x$ from the central axis. If Δx is larger than the maximum radius of the rotor, the beam passes the rotor without being clipped and enters the imaging setup for a second time. Two passes through the 4-f imaging setup create an upright image of the first rotating mirror surface on the parallel second surface. The reflection from this surface produces a stationary output beam from the rotation-angle-dependent deflection beams for a continuous range of rotation angles. As in the second variant, the (close to) collimated input beam is focused in the Fourier planes in the symmetry plane, and input or output coupling elements can be placed at some position of the deflection beam having a suitable beam size. A major advantage of this geometry is its inherent insensitivity to vibrations and other deviations from a perfect rotation of the rotor: Any kind of angular or positional error of the first surface is reproduced by the second surface and, due to the imaging system, its effects on the output beam cancel out.

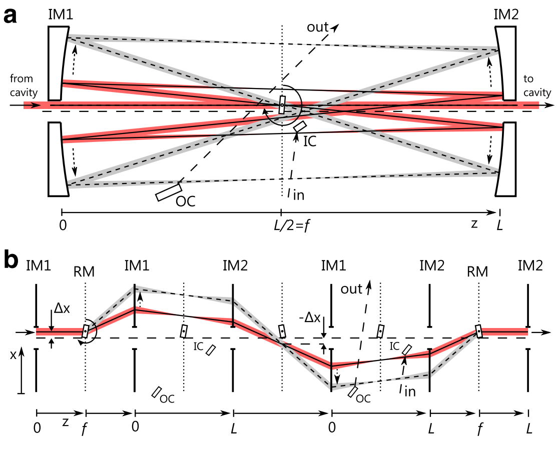

Fig. 3 **a** Top view of the planar two-mirror geometry with a two-faceted rotor (RM), two imaging mirrors (IM1, IM2), an input coupling mirror (IC), and an output coupling mirror (OC). The beam path is shown for two rotation angles (*solid line* just after input coupling, *dashed line* just before output coupling). **b** Schematic view of the beam path. The beam passes each of the imaging mirrors twice

The rotor can be a two-faced substrate, or have a geometry with a larger number of parallel surface pairs, i.e., square, hexagonal, and so forth. A simple two-faced rotor would allow for a switching rate corresponding to twice the rotation frequency. Rotors with a higher number of facets would further increase the maximum switching rate. For small deflection angles, the transverse separation of the paths of subsequent pulses is

$$\Delta s_3 = 2\pi L \frac{f_{\mathrm{rot}}}{f_{\mathrm{rep}}}. \tag{6}$$

In contrast to the first two variants, this separation does not depend on the deflection angle. Consequently, a much larger separation or, alternatively, a much shorter switching time can be achieved in a system with the same footprint. The deflection angle Θ equals twice the rotation angle, i.e., the angle of incidence on the rotating mirrors. The maximum range of deflection angles $\Delta\Theta$ for which the cavity is open is given by the minimum angle Θ_{min} for which the beam is not clipped by the rotating mirror in the first Fourier plane (Fig. 3b), and a maximum angle Θ_{max} given by the dimensions of the imaging mirrors. The maximum number of round-trips N which a pulse can undergo in a cavity containing this pulse picker is

$$N_{\mathrm{plan}} = \frac{\Theta_{\mathrm{max}} - \Theta_{\mathrm{min}}}{4\pi} \frac{f_{\mathrm{rep}}}{f_{\mathrm{rot}}}. \tag{7}$$

Since the angle of incidence on the rotating mirrors is not constant, rotation-angle-dependent astigmatism will occur when spherical imaging mirrors are used. These changes in the effective focal length of the imaging mirrors with the rotation angle will cause a varying ellipticity of the cavity mode. If large deflection angles are required, the use of parabolic imaging mirrors might be necessary (also depending on the sensitivity of the surrounding cavity). In this geometry, the rotation of the mirrors during the propagation time in the device causes a small tilt of the output beam that is constant for a given rotation frequency.

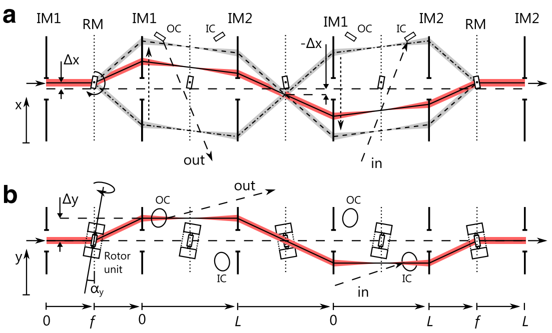

Fig. 4 **a** Schematic top view of the beam path in the nonplanar two-mirror geometry for three rotation angles (*dash-dotted line* path of a pulse just after input coupling, *dashed line* just before output coupling, *solid line* in between). **b** Schematic side view of the beam path. The inclined rotation axis allows the beam path to circumvent the rotor unit and the opening in the imaging mirrors

5 Nonplanar double-mirror geometry

Figure 4 shows a simple modification of the planar double-mirror geometry with which the maximum deflection angle to achieve a specific number of round-trips can be reduced by more than a factor of two. Here, the rotating mirror and its rotation axis are inclined by an angle α_y in the $z{-}y$ plane with respect to the symmetry plane of the imaging setup, offsetting the beam by Δy in the first Fourier plane, and $-\Delta y$ in the second Fourier plane (Fig. 4b). With this modification, the deflection beam circumvents the rotor and its bearing and the holes in the imaging mirrors, even for zero deflection angle in the $x - z$ plane. Thus, there is an unobstructed path for the deflection beam for all deflection angles between $-\Theta_{\max}$ and $\Theta_{\max}$, and $\Delta\Theta$ is equal to $2\Theta_{\max}$. The maximum number of round-trips is now

$$N_{\mathrm{nonplan}} = \frac{\Theta_{\max}}{2\pi}\frac{f_{\mathrm{rep}}}{f_{\mathrm{rot}}}. \tag{8}$$

The minimum width X of the imaging mirrors is

$$X_{\mathrm{nonplan}} = N\Delta s_3. \tag{9}$$

6 Application example 1: regenerative amplifier

The nonplanar double-mirror geometry would be particularly suited for regenerative amplifiers. With rotation frequencies of several kHz and multifaceted rotors, switching rates of up to a few 10 kHz should be achievable. We exemplify practical pulse-picker parameters based on an amplifier build by Nubbemeyer et al. [20], who have recently achieved an average power of about 1 kW at an output repetition rate of either 5 or 10 kHz, with 40 round-trips and a cavity repetition rate of 20 MHz. A nonplanar double-mirror optomechanical switch with a two-surface rotor at a rotation frequency of 5 kHz would allow an output repetition rate of both 5 or 10 kHz. A magnetically beared motor which could be suitable for this application is commercially available [21]. Its length along the rotation axis is 85 mm. To achieve 40 round-trips, $\Delta\Theta$ has to be 7.2° (Eq. 8), resulting in a maximum angle of incidence of 1.8° in the $z{-}x$ plane. With a distance of 1 m between the imaging mirrors, a pulse path separation of 1.57 mm would be achieved (Eq. 6). The dimensions of the motor would imply a Δy of about 45 mm, and thus an angle of incidence of 3° in the $z{-}y$ plane. The input/output coupling plate could be placed at a position where the beam radius is 0.7 mm. With an angle of incidence of 88°, the spot on the plate would be elongated to a w of 20 mm. For a Gaussian profile with this spot size and a pulse energy of 200 mJ, the peak fluence is about 0.9 J cm^{-2} (Eq. 5). At a central wavelength of 1053 nm and a pulse duration of 1 ns, the damage fluence of fused silica is about 40 J cm^{-2}; for a pulse duration of 1 ps, it is 2 J cm^{-2} [22]. Shorter amplifier cavities would allow for a larger number of round-trips, but increase the fluence on the output coupler in a system with identical dimensions. Higher output rates can be achieved by using multifaceted rotors. In conclusion, the outlined optomechanical pulse picker could tolerate higher pulse energies, and/or far shorter pulses than state-of-the-art Pockels cells. Apart from the higher damage threshold, the losses, nonlinearity, thermal lensing, and dispersion associated with the transmission through the Pockels cell would be avoided. An optomechanical pulse picker would likely require vacuum for stable operation.

7 Application example 2: Stack-and-dump cavity

In Ref. [7], a stack-and-dump cavity with a repetition rate of 10 MHz is proposed as a part of a future fiber-laser-based particle accelerator. From this cavity, an output pulse energy of 1.2 J with pulses stretched to 4 ns is envisaged. The pulse train seeding the cavity is continuous, making a pulse picker that provides an unobstructed beam path for most of the output repetition period necessary. We outline practical parameters for an optomechanical pulse picker of a circular double-mirror geometry as discussed in Sect. 4, and a rotation frequency of 8.3 kHz [15]. With this output switching rate, the maximum number of stacked pulses is 1200. With a length of 1.5 m, a distance between the rotating mirrors of 70 mm and an angle of incidence of 2°, the diameter of the deflection beam circle on the imaging mirrors is about 100 mm. At an angle of incidence of 2°, birefringent effects in typical broadband highly reflective mirrors are negligible even for the largest bandwidths yet demonstrated in high-finesse ECs [23]. The separation of

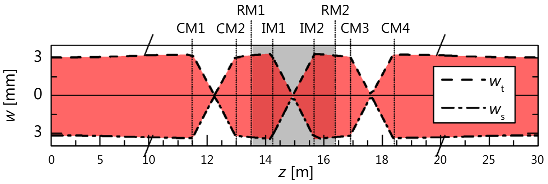

Fig. 5 Calculated sagittal and tangential $1/e^2$-intensity radius (w_s, w_t) for the 10-MHz EC outlined in Sect. 8 containing a pulse picker of the circular two-mirror geometry (RM1, IM1, IM2, RM2), and four additional curved mirrors (CM1-4)

the optical axes of successive pulses is 0.26 mm (Eq. 4). For a pulse energy of 1.2 J and a beam radius of 130 µm at an output coupler with 89° angle of incidence, the peak fluence would be 79 J cm^{-2}. Using the $\tau^{0.5}$-law for the pulse width dependence of the damage threshold, a damage threshold of fused silica of about 80 J cm^{-2} for a pulse duration of 4 ns can be extrapolated from the measurements in [22], putting the highly ambitious pulse energy targeted in [7] within reach.

8 Misalignment sensitivity

The feasibility of the concept critically depends on the perturbations of the beam caused by the rotation of the mirrors, and on the sensitivity of the application to these. While the imaging configuration ideally results in a stationary output beam, misalignments, manufacturing tolerances, and astigmatism in spherical imaging mirrors can cause a rotation-angle-dependent translation and ellipticity of the mode. An important question for intra-resonator applications is whether the resulting periodic change in the beam path and shape causes any significant effects that would not be present for a static misalignment or astigmatism. If so, such effects would be particularly severe for enhancement cavities, where the circulating pulse train needs to overlap spatially, temporally, and in terms of its polarization with an incoming pulse train. To address this question, we simulate the enhancement in a 10-MHz EC including an optomechanical pulse picker as outlined in the previous section, giving a maximum number of 1200 round-trips between two switching events. To be able to tune the position in the cavity's stability range, the cavity should include additional concave mirrors. In a cavity with a round-trip Gouy phase close to an odd multiple of π, large spots on the mirrors can be achieved while avoiding a high misalignment sensitivity [19]. In our cavity example, two pairs of concave mirrors with a radius of curvature of 1500 mm are used. With a distance of 1470 mm between each of the two curved mirror pairs and a wavelength of 1040 nm, the beam radius is about 3 mm on all cavity mirrors (Fig. 5). Assuming the same footprint as in [14], 20 flat folding mirrors producing overall losses of about 400 ppm are needed. To achieve a good stacking efficiency with 1150 round-trips, an input coupler of 99.75% reflectivity is chosen.

Because of the rotating deflection beam path, the cavity cannot be described using "global" sagittal and tangential planes. Here, we simulate the buildup in the cavity numerically in 3D using a modified Fox-Li algorithm [24]. The beam size and divergence of a round input beam is optimized for the cavity with an inactive pulse picker (rotating mirrors are at rest). In this case, the simulation yields an enhancement of about 780 after 1150 round-trips, corresponding to a stacking efficiency of 0.65. The angle of incidence of 2° on the imaging mirrors causes an eccentricity of the beam of 0.27 at the curved cavity mirrors. The simulation for an active pulse picker shows a periodic rotation of the major axis of the elliptic intracavity mode profile with the deflection beam path, but no change in the enhancement level. When a tilt of one of the rotating mirrors is introduced, the central axis of the cavity beam is misaligned. For the active pulse picker, the misaligned beam axis periodically rotates around the axis of the unperturbed beam. The enhancement level drops by the same amount for both the active and inactive pulse picker. The loss of enhancement stems exclusively from the decrease in the spatial overlap of the intracavity beam with the seeding beam. Thus, we can follow the approach taken in [19], which uses far less computation time, to investigate the misalignment sensitivity of the system in detail.

We find that in the cavity example used above, positioning errors or tilts of the imaging mirrors also lead to a rotating cavity beam axis. For instance, a quite large positioning error of one of the imaging mirrors of 5 mm along the z-axis results in a loss of overlap with a fixed input beam of about 10%. A tilt of one of the imaging mirrors by 10 µrad results in an overlap reduction of 4%. A tilt of the rotation axis and the rotor with respect to the imaging mirrors causes a stationary misalignment, but no rotation of the cavity beam axis. For pulse pickers of the circular two-mirror geometry, the rotating mirror surfaces should have identical inclination angles and orientations with respect to the axis of rotation. Errors in the inclination angle can be compensated by adjusting the distances of the rotating to the stationary mirrors to change the magnification of the imaging system. For example, for an error of the inclination angle of 100 µrad, a nearly static cavity beam can be achieved by repositioning both imaging mirrors by about 20 mm along the z-axis. However, the imaging setup cannot compensate for different orientations of the mirrors, i.e., when the planes of the inclination angles of the mirrors are not identical. The effective mirror tilt resulting from this effect is described by Eq. 3, with $\Delta\phi$ now representing the orientation mismatch. In the cavity simulation, an orientation mismatch of 500 µrad results in a rotating offset of the intracavity mode axis of about 0.2 mm at the curved cavity mirrors and the overlap decreases by 10%. Since the rotor has to meet high mechanical demands, and its mirrors will most probably not be adjustable, achieving the necessary accuracy in the orientation of the surfaces will be critical. Importantly, the sensitivity of the EC with respect to misalignments of the mirrors comprising the pulse picker is not higher than for the other cavity mirrors. Furthermore, all perturbations are periodic and synchronized to the output repetition rate, resulting in a stable output. While a detailed analysis of all possible perturbations exceeds the scope of the paper, we conclude that we see no fundamental limitations related to the alignment sensitivity of the optomechanical pulse picker.

9 Sensitivity to rotor motion irregularities

Another important aspect of the technical implementation of this concept will be deviations of the actual rotor motion from a perfect rotation caused by, e.g., unbalance. These can be classified in three categories: parallel deviations (shifts) and angular deviations (tilts) of the rotation axis, and axial displacements of the rotor along the rotation axis. The planar and nonplanar double-mirror geometries are inherently insensitive to these effects. Here, the upright imaging of the front surface of the compact rotor onto its back surface results in a self-compensation of positional and angular errors of the rotor position. Axial displacements are parallel to the rotor surfaces. For the circular one-mirror geometry, in contrast, axial movements would directly translate to changes in the cavity length and, therefore, render its use for applications requiring interferometric stability challenging. Parallel rotation errors would, to a much lesser extent, also affect the cavity length. The imaging configuration results in self-compensation of angular rotation errors. The circular two-mirror geometry is insensitive to length changes due to axial rotor positioning errors, since the displacement of the first rotating mirror surface is compensated by an identical displacement of the second surface. However, due to the inverted imaging configuration in this geometry, angular errors of the rotor position result in a displacement of the cavity beam path. For the stack-and-dump-cavity example described in the previous section, an angular error of 10 µrad corresponding to a rotor tip displacement of 0.35 µm would result in a 14% decrease in overlap. In [15], a maximum displacement of the rotor tip of 17 µm is measured at a rotation frequency of 8.7 kHz. These measurements were taken with an unbalanced rotor, and it is not stated how much of the displacement is due to angular deviations. Still, the results suggest that the balancing of the rotor and the optimization of its active stabilization may be the main technological challenges for an application of the concept in enhancement cavities. For the regenerative amplifier application discussed in Sect. 6, the effects of the rotor displacements reported in [15] would be negligible.

10 Conclusion

In this article, we have outlined a concept for a family of ultrafast all-reflective pulse pickers. Discussing three specific geometries, we have shown that such optomechanical pulse pickers could particularly benefit high-power and high-pulse energy applications. Designs suitable for regenerative amplifiers could support pulse energies of several joules and repetition rates of up to a few tens of kHz, while circumventing the losses, dispersion, and the nonlinear and thermal effects in state-of-the-art Pockels cells. Optomechanical pulse picking could additionally render the temporal stretching of pulses in such systems unnecessary. The concept also holds promise for cavity dumping in passive enhancement cavities. Here, output repetition rates of up to several kHz could potentially be reached for joule-level output pulse energies. Other applications may emerge in wavelength ranges where conventional pulse pickers are not available, in particular in the terahertz [25] and X-ray [26] ranges.

Acknowledgements Open access funding provided by Max Planck Society. We thank Henning Carstens for help with the simulations. We thank Sven Breitkopf, Jens Limpert, Thomas Nubbemeyer, and Moritz Ueffing for fruitful discussions. This work was funded by the European Research Council under Grant Agreement No. [617173] ACOPS.

References

1. A. Killi, J. Dörring, U. Morgner, M.J. Lederer, J. Frei, D. Kopf, Opt. Expr. **13**(6), 1916 (2005). doi:10.1364/OPEX.13.001916
2. C. Hönninger, I. Johannsen, M. Moser, G. Zhang, A. Giesen, U. Keller, Appl. Phys. B **65**(3), 423 (1997). doi:10.1007/s003400050291
3. A. Beyertt, D. Nickel, A. Giesen, Appl. Phys. B **80**(6), 655 (2005). doi:10.1007/s00340-005-1796-3
4. T. Metzger, A. Schwarz, C.Y. Teisset, D. Sutter, A. Killi, R. Kienberger, F. Krausz, Opt. Lett. **34**(14), 2123 (2009). doi:10.1364/OL.34.002123
5. T. Heupel, M. Weitz, T.W. Hänsch, Opt. Lett. **22**(22), 1719 (1997). doi:10.1364/OL.22.001719

6. R.J. Jones, J. Ye, Opt. Lett. **27**(20), 1848 (2002). doi:10.1364/OL.27.001848
7. S. Breitkopf, T. Eidam, A. Klenke, Lv Grafenstein, H. Carstens, S. Holzberger, E. Fill, T. Schreiber, F. Kraus, A. Tünnermann, I. Pupeza, J. Limpert, Light Sci. Appl. **3**(10), e211 (2014). doi:10.1038/lsa.2014.92
8. G. Mourou, B. Brocklesby, T. Tajima, J. Limpert, Nat. Photon. **7**(4), 258 (2013). doi:10.1038/nphoton.2013.75
9. J.P. Negel, A. Voss, M.A. Ahmed, D. Bauer, D. Sutter, A. Killi, T. Graf, Opt. Lett. **38**(24), 5442 (2013). doi:10.1364/OL.38.005442
10. K. Michel, S. Klingebiel, M. Schultze, C.Y. Tesseit, R. Bessing, M. Häfner, S. Prinz, D. Sutter, T. Metzger: *SPIE LASE*, ed. by W.A. Clarkson, R.K. Shori (SPIE 2016), SPIE Proc. doi:10.1117/12.2208127
11. H. Fattahi, A. Alismail, H. Wang, J. Brons, O. Pronin, T. Buberl, L. Vamos, G. Arisholm, A.M. Azzeer, F. Krausz, Opt. Lett. **41**(6), 1126 (2016). doi:10.1364/OL.41.001126
12. Y. Vidne, M. Rosenbluh, T.W. Hansch, Opt. Lett. **28**(23), 2396 (2003). doi:10.1364/OL.28.002396
13. R.J. Jones, J. Ye, Opt. Lett. **29**(23), 2812 (2004). doi:10.1364/OL.29.002812
14. S. Breitkopf, S. Wunderlich, T. Eidam, E. Shestaev, S. Holzberger, T. Gottschall, H. Carstens, A. Tünnermann, I. Pupeza, J. Limpert, Appl. Phys. B. **122**(12), 297 (2016). doi: 10.1007/s00340-016-6574-x
15. T. Baumgartner, R.M. Burkart, J.W. Kolar, IEEE Trans. Ind. Electron. **61**(8), 4326 (2014). doi:10.1109/TIE.2013.2284159
16. D. Esser, J. Weitenberg, W. Broring, I. Pupeza, S. Holzberger, H.D. Hoffmann, Opt. Expr. **21**(22), 26797 (2013). doi:10.1364/OE.21.026797
17. H. Carstens, N. Lilienfein, S. Holzberger, C. Jocher, T. Eidam, J. Limpert, A. Tünnermann, J. Weitenberg, D.C. Yost, A. Alghamdi, Z. Alahmed, A. Azzeer, A. Apolonski, E. Fill, F. Krausz, I. Pupeza, Opt. Lett. **39**(9), 2595 (2014)
18. N. Lilienfein, H. Carstens, S. Holzberger, C. Jocher, T. Eidam, J. Limpert, A. Tünnermann, A. Apolonski, F. Krausz, I. Pupeza, Opt. Lett. **40**(5), 843 (2015). doi:10.1364/OL.40.000843
19. H. Carstens, S. Holzberger, J. Kaster, J. Weitenberg, V. Pervak, A. Apolonski, E. Fill, F. Krausz, I. Pupeza, Opt. Expr. **21**(9), 11606 (2013)
20. T. Nubbemeyer, et al.: Manuscript under preparation
21. http://www.celeroton.com/fileadmin/user_upload/produkte/motoren/datasheets/Datasheet CM-AMB-400
22. B.C. Stuart, M.D. Feit, A.M. Rubenchik, B.W. Shore, M.D. Perry, Phys. Rev. Lett. **74**(12), 2248 (1995)
23. S. Holzberger, N. Lilienfein, M. Trubetskov, H. Carstens, F. Lucking, V. Pervak, F. Krausz, I. Pupeza, Opt. Lett. **40**(10), 2165 (2015). doi:10.1364/OL.40.002165
24. A.G. Fox, T. Li, Bell Syst. Techn. J. **40**(2), 453 (1961). doi:10.1002/j.1538-7305.1961.tb01625.x
25. S. Takahashi, G. Ramian, M. Sherwin, Appl. Phys. Lett. **95**(23), 234102 (2009). doi:10.1063/1.3270041
26. M. Cammarata, L. Eybert, F. Ewald, W. Reichenbach, M. Wulff, P. Anfinrud, F. Schotte, Rev. Sci. Instr. **80**(1), 015101 (2009). doi:10.1063/1.3036983

Data archiving

The original figure files, raw data, scripts and additional information needed to reproduce each figure enclosed in this thesis can be found on the Data Archive Server of the Laboratory for Attosecond Physics at the Max Planck Institute of Quantum Optics.

The data relating to the figures contained in Part I of this thesis are archived in the directory:
`/afs/ipp/mpq/lap/publication_archive/Theses/2018/`
`Lilienfein Nikolai (PhD)/`
The subfolders of the '`/Figures`' directory, named corresponding to the figure number as appearing in this thesis, contain the data related to the respective figure.

Data relating to the individual publications enclosed in Part II of this thesis are archived in the following directories:

Chapter 5:
`/afs/ipp/mpq/lap/publication_archive/Papers/2015/`
`Lilienfein_OptLett_thermal_lenses/`

Chapter 6:
`/afs/ipp/mpq/lap/publication_archive/Papers/2015/`
`Holzberger_Enhancement cavities in the nonlinear regime/`

Chapter 7:
`/afs/ipp/mpq/lap/publication_archive/Papers/2015/`
`Holzberger_Enhancement cavities for zero-offset-frequency pulse trains/`

Chapter 8:
`/afs/ipp/mpq/lap/publication_archive/Papers/2017/`
`Lilienfein_OptLett_few-cycle/`

Chapter 9:
`/afs/ipp/mpq/lap/publication_archive/Papers/2019/`
`Lilienfein_Temporal solitons in free-space femtosecond enhancement`
`cavities/`

Chapter 10:
`/afs/ipp/mpq/lap/publication_archive/Papers/2017/`
`Lilienfein_Springer_ultrafast_pulse_picking/`

List of publications

Manuscripts included in this thesis

1. N. Lilienfein, H. Carstens, S. Holzberger, C. Jocher, T. Eidam, J. Limpert, A. Tünnermann, A. Apolonski, F. Krausz, and I. Pupeza, “Balancing of thermal lenses in enhancement cavities with transmissive elements,” *Optics Letters* 40, 843–846 (2015), DOI: 10.1364/OL.40.000843.

2. S. Holzberger, N. Lilienfein, M. Trubetskov, H. Carstens, F. Lücking, V. Pervak, F. Krausz, and I. Pupeza, “Enhancement cavities for zero-offset-frequency pulse trains,” *Optics Letters* 40, 2165–2168 (2015), DOI: 10.1364/OL.40.002165.

3. S. Holzberger, N. Lilienfein, H. Carstens, T. Saule, M. Hogner, F. Lücking, M. Trubetskov, V. Pervak, T. Eidam, J. Limpert, A. Tünnermann, E. Fill, F. Krausz, and I. Pupeza, “Femtosecond enhancement cavities in the nonlinear regime,” *Physical Review Letters* 115, 023902 (2015), DOI: 10.1103/PhysRevLett.115.0239025.

4. N. Lilienfein, C. Hofer, S. Holzberger, C. Matzer, P. Zimmermann, M. Trubetskov, V. Pervak, and I. Pupeza, “Enhancement cavities for few-cycle pulses”, *Optics Letters* 42, 271–274 (2017), DOI: 10.1364/OL.42.000271.

5. N. Lilienfein, S. Holzberger, and I. Pupeza, “Ultrafast optomechanical pulse picking,” *Applied Physics B* 123, 1916 (2017), DOI: 10.1007/s00340-016-6608-4

6. N. Lilienfein, C. Hofer, T. Saule, M. Högner, M. Trubetskov, V. Pervak, E. Fill, C. Riek, A. Leitenstorfer, J. Limpert, F. Krausz, and I. Pupeza, “Temporal solitons in free-space femtosecond enhancement cavities,” Manuscript in review as a *Letter* to *Nature Photonics*, submitted on June 14th, 2018.[1]

Other journal articles

1. H. Carstens, N. Lilienfein, S. Holzberger, C. Jocher, T. Eidam, J. Limpert, A. Tünnermann, J. Weitenberg, D. C. Yost, A. Alghamdi, Z. Alahmed, A. Azzeer, A. Apolonski, E. Fill, F. Krausz, and I. Pupeza, “Megawatt-scale average-power ultrashort pulses in an enhancement cavity”, *Optics Letters* 39, 2595-2598 (2014), DOI: 10.1364/OL.39.002595.

---

[1] A revised version of this manuscript has been published in *Nature Photonics* on January 21st, 2019. DOI: 10.1038/s41566-018-0341-y

2. I. Pupeza, D. Sánchez, J. Zhang, N. Lilienfein, M. Seidel, N. Karpowicz, T. Paasch-Colberg, I. Znakovskaya, M. Pescher, W. Schweinberger, V. Pervak, E. Fill, O. Pronin, Z. Wei, F. Krausz, A. Apolonski, J. Biegert, and I. Pupeza, "High-power sub-two-cycle mid-infrared pulses at 100 MHz repetition rate", *Nature Photonics* 11, 721 (2015), DOI: 10.1038/NPHOTON.2015.1795.

3. J. Zhang, J. Brons, N. Lilienfein, E. Fedulova, V. Pervak, D. Bauer, D. Sutter, Z. Wei, A. Apolonski, O. Pronin, and F. Krausz, "260-megahertz, megawatt-level thin-disk oscillator", *Optics Letters* (2015), DOI: 10.1364/OL.40.001627.

4. H. Carstens, M. Högner, T. Saule, S. Holzberger, N. Lilienfein, A. Guggenmos, C. Jocher, T. Eidam, D. Esser, V. Tosa, V. Pervak, J. Limpert, A. Tünnermann, U. Kleineberg, F. Krausz, and I. Pupeza, "High-harmonic generation at 250 MHz with photon energies exceeding 100 eV", *Optica* 3, 366-369, (2016), DOI: 10.1364/OPTICA.3.000366.

5. M. Högner, T. Saule, N. Lilienfein, V. Pervak, and I. Pupeza, "Tailoring the transverse mode of a high-finesse optical resonator with stepped mirrors", *Journal of Optics* 20 (2017), DOI: 10.1088/2040-8986/aa9ece.

6. S. Breitkopf, N. Lilienfein, T. Achtnich, C. Zwyssig, A. Tünnermann, I. Pupeza, and J. Limpert, "Velocity-and pointing-error measurements of a 300 000-r/min self-bearing permanent-magnet motor for optical applications", *Review of Scientific Instruments* 89 (2018), DOI: 10.1063/1.5012834.

7. J. Xu, B. Globisch, C. Hofer, N. Lilienfein, T. Butler, N. Karpowicz, and I. Pupeza, "Three-octave terahertz pulses from optical rectification of 20-fs, 1-µm, 78-MHz pulses in GaP", *Journal of Physics B: Atomic, Molecular and Optical Physics* 51 (2018), DOI: 10.1088/1361-6455/aacfe7.

8. T. Saule, M. Högner, N. Lilienfein, O. DeVries, M. Ploetner, V. S. Yakovlev, N. Karpowicz, J. Limpert, and I. Pupeza, "Cumulative plasma effects in cavity-enhanced high-order harmonic generation in gases", *APL Photonics* 3 (2018), DOI: 10.1063/1.5037196.

Other manuscripts in review

1. T. Saule, S. Heinrich, J. Schoetz, N. Lilienfein, M. Högner, O. DeVries, M. Ploetner, J. Weitenberg, D. Esser, J. Schulte, P. Russbueldt, J. Limpert, A. Tünnermann, M. F. Kling, U. Kleineberg, and I. Pupeza, "High-Flux, High-Photon-Energy Ultrafast Extreme-Ultraviolet

Photoemission Spectroscopy at 18.4 MHz Pulse Repetition Rate", Manuscript in review at *Nature Photonics*, submitted on April 19th, 2018. [2]

2. C. Gaida, T. Heuermann, M. Gebhardt, E. Shestaev, T.P. Butler, D. Gerz, N. Lilienfein, P. Sulzer, M. Fischer, R. Holzwarth, A. Leitenstorfer, I. Pupeza, J. Limpert, "High-power frequency comb at 2 µm wavelength emitted by a Tm-doped fiber laser system," Manuscript in review at *Optics Letters*, submitted on August 22nd, 2018.[3]

Patent applications

1. Lilienfein, N., Holzberger, S., and Pupeza, I., "Optical beam switch apparatus, beam switching method, and applications thereof", International Patent Application WO/2017/211375, filed June 10, 2016.

Conference contributions (Talks)

1. N. Lilienfein, H. Carstens, S. Holzberger, C. Jocher, T. Eidam, J. Limpert, A. Tünnermann, A. Apolonski, F. Krausz, and I. Pupeza, "Balancing thermal lensing in enhancement cavities," in *European Conference on Lasers and Electro-Optics*, CF_9_2 (Optical Society of America, 2015).

2. N. Lilienfein, S. Holzberger, M. Trubetskov, H. Carstens, F. Lücking, V. Pervak, F. Krausz, and I. Pupeza, "Enhancement cavities for pulse trains with fixed offset frequency," in *10th International Conference on Ultrafast Optics*, UFO0095, (Beijing, China 2015).

3. N. Lilienfein, C. Hofer, S. Holzberger, C. Matzer, P. Zimmermann, M. Trubetskov, V. Pervak, and I. Pupeza, "Bandwidth scaling of near-infrared enhancement cavities," in *European Conference on Lasers and Electro-Optics*, CF_1_6 (Optical Society of America, 2017).

---

[2] This manuscript has been accepted for publication in *Nature Communications* on January 4th, 2019. DOI: 10.1038/s41467-019-08367-y

[3] This manuscript has been accepted for publication in *Optics Letters* on October 12th, 2018. DOI: 10.1364/OL.43.005178y

Danksagung

Zu guter Letzt möchte ich mich bei den vielen Menschen bedanken, die diese Arbeit ermöglicht haben.

An erster Stelle ist hier mein Doktorvater Ferenc zu nennen, zum Einen für deine Betreuung meiner Promotion und deinen Rat und zum Anderen für die herausragenden Bedingungen die du für unsere Gruppe geschaffen hast. Diese betreffen nicht allein den finanziellen Rückhalt den das Projekt stets genossen hat, sondern auch das von dir gestaltete wissenschaftliche Umfeld von dem ich immens profitiert habe.

Besonderer Dank gebührt meinem Teamleiter Ioachim für die direkte Betreuung dieser Arbeit. Mit deiner Zielstrebigkeit und Begeisterung hast du ein wunderbares Team geschaffen. Ohne deine Kreativität und Offenheit gegenüber allen möglichen Ideen, aber auch deine Hartnäckigkeit in der Verfolgung unserer Ziele und deine Überzeugungskraft in Wort und Text hätte diese Arbeit nicht zustande kommen können.

Sehr dankbar bin ich auch den anderen Kollegen in unserem kleinen Team. Zuerst sind hier meine Seniordoktoranden Henning und Simon zu nennen. Ihr habt meine Begeisterung für die Laserei geweckt, und ich bin froh dieses edle Handwerk von euch gelernt zu haben. Herzlich danken für die gemeinsame Arbeit und Zeit möchte ich auch Tobi, mit seiner unvergleichbaren Hilfsbereitschaft, begeisternden Athletik an Justageschrauben und Klettergriffen und beeindruckenden Virtuosität im immerwährenden Ausbau seines Setups, Maxi, dem Magier an der Tastatur, dem großen Schlangenbeschwörer und HHG Guru, und Stefan, dem Herrn der letzten Kammer, der mit großer Ausdauer unsere Arbeit endlich ihrer Anwendung zuführt. Besonderer Dank gilt Christina, für die Beiträge zu unseren gemeinsamen Experimenten die du während der Masterarbeit mit schnellem Auffassungsvermögen und großem Geschick geleistet hast, und für deine Hilfsbereitschaft, von der ich seitdem oft profitiert habe. Die mit euch allen durchlebten Abenteuer in Labor und freier Wildbahn und die lebhaften Diskussionen über Optik, Gott und die Welt haben dieser Zeit die Würze gegeben.

Weiterhin möchte ich mich bei der Jenenser Faserlasergruppe um Jens für unsere hervorragenden Lasersysteme, sowie für eure großartige Unterstützung und die immer produktive Zusammenarbeit bedanken. Eine kompetentere und hilfsbereitere Truppe kann man sich nicht vorstellen. Jens möchte ich außerdem für die Übernahme des Koreferats dieser Arbeit danken. Besonders möchte ich auch Sven für deine Begeisterungsfähigkeit, die tolle Zusammenarbeit bei der Rotorvermessung und deine Hilfsbereitschaft bei der Laserbetreuung danken.

Special thanks go to Vladimir and Michael for your great endurance in supplying us with designs and coatings for ever more ambitious cavity mirrors. Without you, most of the results of this thesis would have been impossible.

Danken möchte ich auch der Cavity Gruppe um Thomas. Von euch habe ich insbesondere in der Anfangsphase meiner Arbeit sehr viel gelernt habe und eure vielen Leihgaben haben uns das Leben sehr erleichtert. Besondere Erwähnung verdient Johannes für seine akribischen und hilfreichen Rückmeldungen zu unseren Manuskripten und unsere lebhaften und lehrreichen Diskussionen.

I also want to acknowledge Oleg for his brief supervision, and Jinwei for our productive and entertaining teamwork on the setup of our mode-locked thin-disk laser.

Danken möchte ich auch Herrn Öhm und der LMU Werkstatt für die immer zügige und präzise Herstellung vieler Komponenten, und Martin, für dein riesiges Engagement und deine Kreativität, die uns den Umzug ans MPQ sehr erleichtert haben.

Furthermore I would like to thank the past and present members of our Coulombwall lunch group (bing, bing!), and other colleagues at LMU and MPQ for your occasional help, but more importantly for the great times we had during the past years.

For the timely but thorough comments on this thesis i would like to thank Ioachim, Maxi, Tobi, Thomas, Jakob and Johanna.

Zuletzt möchte ich meiner Familie für eure moralische Unterstützung während dieser Zeit, und, viel wichtiger, dafür danken, dass ihr die generellen Bedingungen für das Gelingen dieser Arbeit (Existenz und guter Zustand des Autors, usw.) geschaffen habt.

Mein größter Dank gilt Johanna, für deine beständige Unterstützung trotz der Volatilität von Abend-, Wochenend- und Urlaubsplanungen, und den ein oder anderen Tritt in den Hintern.